# Axon Tracing With Functionalized Paramagnetic Nanoparticles

By

**Harrison John Westwick, BSc.**

A thesis submitted as a partial fulfilment of the degree requirements of the MSc Neuroscience Program

Department of Cellular and Molecular Medicine
Faculty of Medicine
University of Ottawa
Ottawa, Ontario, Canada

# Abstract

It was hypothesized that superparamagnetic nanoparticles encapsulated in a silica shell with a fluorescent dye could be functionalized with axonal tracers and could be used for serial, non-invasive imaging with magnetic resonance imaging (MRI) for axon tract tracing. Nanoparticles functionalized with amine, octadecyl, silica, and biotinylated dextran amine were manufactured and characterized with MRI, scanning electron microscopy, and UV-visible, infrared, and fluorescence spectroscopy. Nanoparticle concentrations of 10 mM were not toxic to adult rat neural progenitor cells (NPCs) and labeled approximately 90% of cells. Nanoparticles were assessed for anterograde and retrograde tract tracing in adult rat models. With MRI and microscopy, the nanoparticles did not appear to trace axons but did provide an MRI signal for up to 3 weeks post implantation. While functionalized nanoparticles did not appear to trace axons, they are not toxic to NPCs and may be used as a MRI contrast agent in the neural axis.

# Acknowledgements

Thanks especially to Dr. Eve Tsai for the supervision of this project and many opportunities she has offered.

Dr. Leo Renaud, Dr. John Woulfe, and Dr. Xudong Cao offered tremendous guidance in this project.

I owe huge thanks to many people who made completing this thesis possible. Foremost thanks to Dr. Arturo Cárdenas-Blanco, Matt Coyle, Ushananthani Shanmugalingam, A-J Hutchings, Dr. Xuefen Yang, and Elaine Coderre. Without all of these people, none of the work would have been possible. Thanks also to Karan Mathur, Bernard Mendis, Madeline Kukko, Jasmine Hasselback, Dr. Farid Bendjelloul among other members of the research group for help with animal experiments and histology. Alain Berthiaume and Natasha La Russa made the MRI experiments possible.

I would like to thank others who were able to support me in this project including Catherine Verreault, Brien Benoit, and my family Barbara, Vince, Valerie, and Will.

# Table of Contents

# List of Tables

# List of Figures

# Nomenclature

AU – Arbitrary Units (Dimensionless)

BDA – Biotin Dextran Amine

C18 – Octadecyl (18 Unsaturated Carbon Chain)

CT – Computed Tomography

CTB – Cholera Toxin Subunit B

DAB - 3,3'-Diaminobenzidine

DEG – Diethylene glycol

DETA - 3-[2-(2-Aminoethylamino)ethylamino]propyl-trimethoxysilane

DiI - 1,1',dioctadecyl-3,3,3'3'-tetramethylindocarbocyanine perchlorate

DMEM/F12 – Dulbecco's modified eagle media F12

ECM – Extracellular Matrix

Fe - Iron

$Gd_2O_3$ – Gadolinium (III) Oxide Nanoparticle

HIV-tat - Human acquired immunodeficiency virus trans-activator of transcription

ICP-AES - inductively coupled plasma atomic absorbance spectrometry

IR – Infrared

α-MEM – α –Minimal essential media

MRI – Magnetic Resonance Imaging

NIR – Near Infrared

NH2 – Primary Amine

NH4OH – Ammonium Hydroxide (aqueous)

NPC – Neural Progenitor Cell

PBS – Phosphate Buffered Saline

ROS – Reactive Oxide Species

RuBpy – Tris-(2,2’-bipyridine) ruthenium (II)

SEM – Scanning Electron Microscopy

SiO2 - Silica

SPIO – Superparamagnetic Iron Oxide

TEOS - Tetrethoxysilane

WGA- Wheat Germ Agglutinin

# Chapter 1: Introduction

## 1.1 Introduction

The study of neuronal circuitry in the brain and spinal cord has been an area of extensive study in neurophysiology. It is well understood that the nervous system functions through interactions of networking neurons where impulses are transmitted down axons which link with a downstream cell[1]. Axon tracing has been pivotal in mapping neuronal connections[2]. Many different approaches have been developed for the study of neuronal networking. Early mapping of the nervous system was accomplished based on examinations of functional gains and losses when a particular structure was ablated or probed. Optical microscopic techniques examining pathways at the histological level were later developed using conventional histology and silver stains to identify neurons [3]. This staining elucidated role and location of neurons in the nervous system, but could not identify specific pathways. Later mapping techniques included tracer molecules which can be injected into a specific cell or nucleus in the nervous system and transported through the axon and identified through histology to map pathways. Early radionuclide tracers identified active axon transport as an important process in the nervous system [4, 5], but this technique could not identify pathways at the histological level. Pathway specific neuronal tracers were developed for optical microscopy; these are molecules injected into the nervous system and are taken up and transported by neurons. Staining for these tracer molecules reveals neuronal pathways [2]. To this day,

axon tracing with histology remains the gold standard in the mapping of neuronal connections. Electron microscopy is a technique which has been used to probe neuronal structures and connections at the sub-cellular level [6-8], and can provide greater resolving power than optical techniques. Electron microscopy suffers the same disadvantages of other histological techniques with optical microscopy in that the tissue cannot be examined *in vivo*. Radiographic techniques were later developed to image the nervous tissue in humans such as computed tomography (CT); however, resolution is highly limited to imaging at the tissue level, and cannot provide information at the cellular level. Magnetic resonance imaging (MRI) provides great resolution improvements for the imaging of anatomy, and can differentiate between grey and white matter along with other finer, smaller structures. MRI is highly advantageous because of its application in living tissue, but is limited in resolution [9, 10], although higher field strength systems can be applied to improve resolution in small animals [11, 12] and for *ex vivo* imaging. Magnetic resonance spectroscopy can provide chemical details from cellular processes and elucidate biochemical information *in vivo* [9]. More advanced diffusion weighted MRI techniques have been able to be used to reconstruct three dimensional depictions of axonal tracts based on the diffusion of water along the length of axons[13-15]. Corroboration of the MRI reconstructed tracts is not easily confirmed with histology. MRI has been applied in the visualization of axon tracts in the spinal cord with the application of a manganese contrast agent [16]; however, corroboration with histology was not possible. Live microscopy has been developed to image axons and neurons in the superficial structures of the brain and spinal cord[17], but only superficial tracts can be visualized.

Bioluminescence, or the use of near infrared (NIR) dyes for the study of cell tracking and diffusion of a dye *in vivo*[18, 19], as well as towards the study of axons [20], have been applied. However, the disadvantage of NIR dyes is that the normal (unstained) host tissue is not clearly identified as it is with MRI. All these techniques have been applied in different ways to the study of neural circuitry, but each technique individually cannot create a full picture.

The imaging techniques used for the study of neuronal circuitry can be divided into two major streams: low resolution methods for serial, non-invasive imaging, and high resolution techniques for fixed tissue imaging. There is a trade off between high resolution imaging and the ability for *in vivo* assessments over time. There are clear advantages to imaging these pathways *in vivo* especially in the study of regeneration after injury; for instance, in spinal cord injury, to quantify the extent of regeneration and which specific tracts are regenerating with a specific treatment. *In vivo* imaging of axon tracing could be applied in a clinical setting for localizing a lesion or quantifying the success of a treatment [21]. Therefore, the development of a hybrid technique which can be applied for both serial, non-invasive imaging and high resolution techniques would be highly beneficial. A breakdown of the levels of resolution of the techniques for the study of neural networks is shown schematically in Figure 1-1. Generally, the techniques capable of serial *in vivo* imaging have less resolution than imaging of tissue post-mortem. It is also clear that imaging post-mortem multiple times in the same subject is not possible. The ideal imaging platform would allow serial, *in vivo* imaging while also being able to provide sub-cellular resolution with conventional optical microscopic techniques.

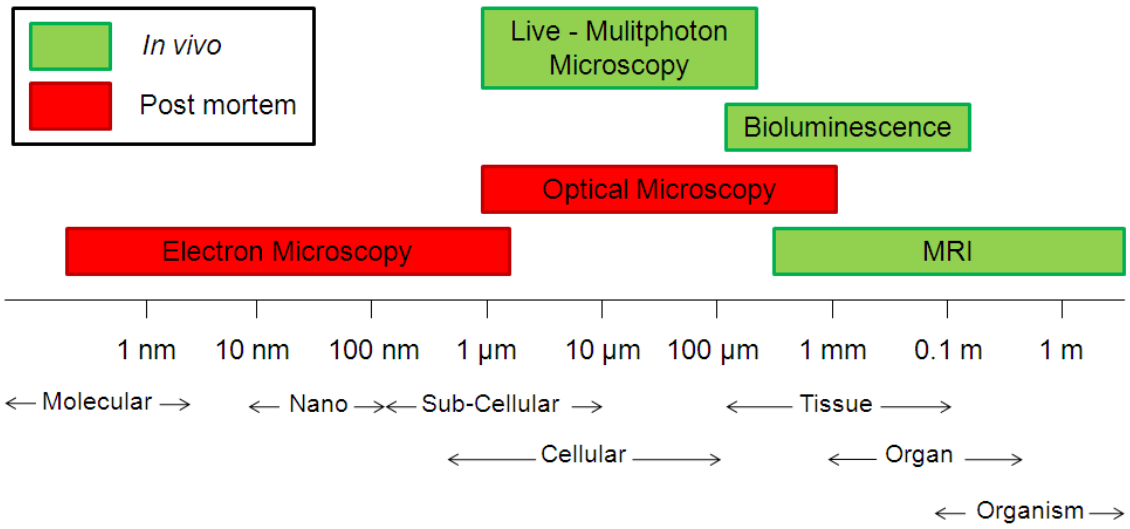


**Figure 1-1: Scale of resolving power of different imaging modalities.**
**The range of applicability of each technique is highlighted, and the applicability for in vivo or only post-mortem tissue is shown. Figure adapted from Schroeder 2008[22].**

The purpose of this study was to attempt to bridge the limitations of the techniques for the imaging of axon tracing in neuronal circuits by combining both optical microscopy and MRI. This approach could facilitate serial, *in vivo* imaging, while allowing later histological studies on the same subject.

Our objective was to design a prototype nanoparticle construct which could be used as a contrast agent for *in vivo* imaging, while at the same time be applicable as a tracer for microscopic studies, along with allowing for the correlation of the MRI axonal fiber tracing results at the microscopic level. A nanoparticle construct was chosen because of its ability to concurrently hold multiple functionalities. The particles used in this experiment were trifunctional including a: 1) magnetic core for MRI contrast, 2) fluorescent shell for optical detection, and 3) surface functionalized shell for cell interaction and internalization. The magnetic core was made of superparamagnetic iron

oxide (SPIO). SPIO nanoparticles have high signal contrast with T2 which is quantifiable and proportional to the concentration of the nanoparticle[23, 24]. Contrast agents are useful in detection and labelling with MRI [25, 26]. The shell was made from the polymerized silica, and the fluorescent dye Tris-(2,2'-bipyridine) ruthenium (II) (RuBpy) was used. The functionalization of the nanoparticle surface was to be done with the axon tracer molecules described below.

It was hypothesized that magnetic nanoparticles could be conjugated with different functional groups allowing for cellular uptake, and cell labelling *in vivo* and that the labelled cells could be visualized both with MRI and histologically without a high level of toxicity. To test uptake and toxicity at a cellular level, an *in vitro* model of adult rat neural progenitor cells (NPC) isolated from the ependymal zone spinal cord was used. *In vivo* experimentation was done examining Sprague Dawley rats with nanoparticles injected in the brain (anterograde) or spinal cord (retrograde), imaging them with MRI and subsequently histological methods.

Using both *in vitro* neural progenitor cell (NPC) culture techniques and *in vivo* Sprague Dawley rats as models, this hypothesis was addressed in five distinct stages:

1) Development, synthesis, and characterization of functionalized nanoparticles
2) Assessment of toxicity *in vitro*
3) Assessment of cell uptake *in vivo*
4) Assessment of axon tracing *in vivo*
5) Assessment of axon tracing *ex vivo*

## 1.2 Design, Synthesis, and Characterization of Functionalized Nanoparticles

Nanotechnology is generally defined as the study of materials ranging on the size order of 10-100 nm in one, two, or three dimensions; in the case of a thin film, nano rod, or particle respectively[27]. The synthesis of nanomaterials has been described for many years, and nanomaterials offer advantages specifically in that they exist as a hybrid state between a solution state of a material and a bulk state. This hybrid of bulk and molecular states is no clearer than with magnetic iron oxide nanoparticles: when the particles are suspended in solution, the solution is a liquid sol where particles flow freely; however, when in the presence of an applied magnetic field, the nanoparticles aggregate along the magnetic field and behave more like a solid than a liquid. Furthermore, nanoparticles act almost as building blocks allowing for other functionalities to be stuck together on the same functional complex; for instance, fluorescence and magnetism can be assembled together in the same particle. The most notable applications of nanomaterials in the bioscience field are particles with strong luminescent properties for optical imaging (quantum dots)[28, 29], magnetic nanoparticles for imaging or cell separation[26], and loaded nanoparticles for targeted therapeutic drug delivery[30, 31]. Nanomaterials have also been experimented with in the design field of tissue scaffold engineering [32, 33]. Specific applications of nanoparticles to the nervous system have been studied as well. Nanotubes have been used as templates for neurite outgrowth [34], and antioxidant nanoparticles have been studied for their neuroprotective properties against oxidative stress[35]. Studies of the use of magnetic nanoparticles for imaging purposes in neurons are few [36, 37]; however,

there has been a large wealth of research done on labelling neural progenitor cells with nanoparticles for tracking purposes [38, 39] or for MRI detection of neoplasms [40].

### 1.2.1 Nanoparticle Design and Synthesis

The schematic representation of the synthesis of the superparamagnetic iron oxide nanoparticles (SPIO) which are coated with a dye doped silica shell is shown in Figure 1-2. This method for the preparation of multifunctional nanoparticles with silica was chosen because of the strongly magnetic properties of the SPIO particles, the strong luminescence of the RuBpy dye, and the biocompatible, functionalizable silica shell.

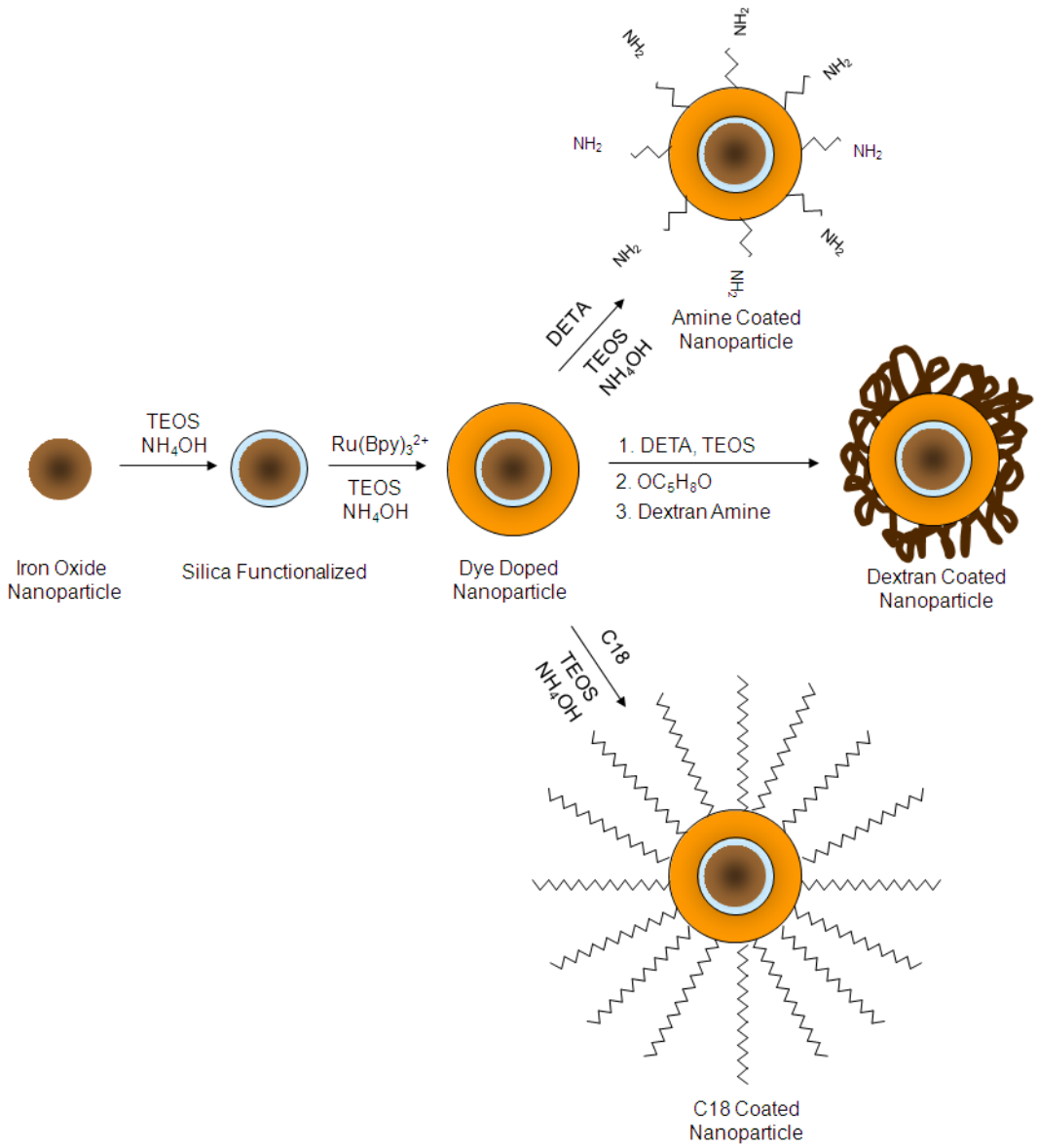


**Figure 1-2: Schematic representation of synthesis route for the preparation of multifunctional nanoparticles as axon tracers.**

### 1.2.2 SPIO nanoparticles

The preparation of SPIO is accomplished through the co-precipitation of ferric iron (III) and ferrous iron (II) in a 2:1 molar ratio in water, and was based on methods

previously described with minor modifications [41, 42]. This method for the preparation of SPIO nanoparticles typically yields particles of a size less than 10 nm, which is small enough to contain only a single magnetic domain. These nanoparticles are magnetic because of the nature of the crystal structure of the iron oxide. The net magnetization stems from the alignment of the spins of the Fe (II) and Fe (III) electrons in the structure [43]. Only in the presence of an applied magnetic field will all of the individual particles align and form a solid mass.

### 1.2.3 Silica encapsulation of SPIO nanoparticles

A silica shell was used in the preparation of the multifunctional nanoparticles for axon tracing because a fluorescent dye can be incorporated directly into the silica shell, silica offers a wide range of chemical functionalizations, silica can chemically stabilize the SPIO nanoparticles in solution, and silica can potentially reduce the toxicity of a SPIO nanoparticle. The Stöber method was used for silica encapsulation of the SPIO nanoparticle. This method has the benefit that no surfactant is needed to stabilize the prepared nanoparticles and is based on the direct hydrolysis and polymerization of the silica precursor tetrethoxysilane (TEOS) [44]. SPIO particles aggregate in solution; therefore, it is necessary to functionalize them appropriately to maintain their small size. The thickness of the silica shell deposited on the nanoparticle can be controlled in the Stöber process by controlling the concentration of TEOS; thinner shells are made with lower TEOS concentrations [45]. Ammonium hydroxide is used to catalyze the hydrolysis of TEOS to $SiO_2$ by first producing the reaction intermediate, silicon hydroxide, with the removal of ethanol [44, 46]. TEOS and silicon hydroxide of opposite charge is highly

attracted to the SPIO particles in solution because of their cationic ammonium stabilization. This acts as a seed for the polymerization of silica [45].

### 1.2.4 Fluorescent shell synthesis on $SiO_2$ coated SPIO nanoparticles

The inorganic complex, tris(2,2′-bipyridyl)dichlororuthenium(II) (RuBpy), is a luminescent inorganic dye with the capability of being incorporated directly into a polymerized silica nanoparticle. The luminescent properties of the RuBpy stem from metal to ligand charge transfer to the bipyridine ligand [42]. Although other dyes such as rhodamine were experimented with [47], RuBpy has a net positive charge allowing for easy initial attraction to the negative silicon hydroxide precursor formed by TEOS. This charge attraction continues to stabilize the structure even after silica has polymerized when the ruthenium center binds electrostatically to the oxygen atoms in the silica polymer, and this prevents leaching of the dye [46]. Preventing leaching is a distinct advantage of this choice of dye. However, RuBpy is limited in this setup because of the fluorescence quenching experienced by surrounding oxygen atoms. To reduce these effects, a spacer layer of silica on top of the SPIO has been incorporated before adding the dye [42] to decrease the effect of the SPIO on fluorescence quenching of the dye.

### 1.2.5 Surface functionalization of magnetic nanoparticles

Modification of the silica nanoparticles can be accomplished by a number of functional groups, including amine, thiol, dextran, octadecyl (c18), and polyethylene glycol. All of these means have their advantages; however, primary amine can allow for particle reactivity and potential for covalent linkages to proteins, sugars and nucleic

acids. The primary amine modified TEOS precursor, 3-[2-(2-Aminoethylamino)ethylamino]propyl-trimethoxysilane (DETA) has been used previously to link silica nanoparticles to DNA. Thus, we proposed to utilize DETA to modify the surface of the nanoparticles, as shown in Figure 1-2 to facilitate covalent linkages to proteins and sugars to enable functionalization.

DETA functionalization of the nanoparticles offers a primary amine functionalization. This primary amine functionalization can be used alone due to the positive charge it brings to the nanoparticle, or it can be used as an intermediate step in the further functionalization of the nanoparticle. In the case of the axonal tracer biotin dextran amine (BDA), the BDA is linked to the nanoparticle through an imine bond which is formed with the DETA functionalization. Glutaraldehyde is used for this purpose as it leaves a free aldehyde group on the surface of the particles which allows for BDA attachment. This is shown schematically in Figure 1-3. The free aldehyde group is able to attach to the axonal tracer biotin dextran amine (BDA) through the attached lysine group.

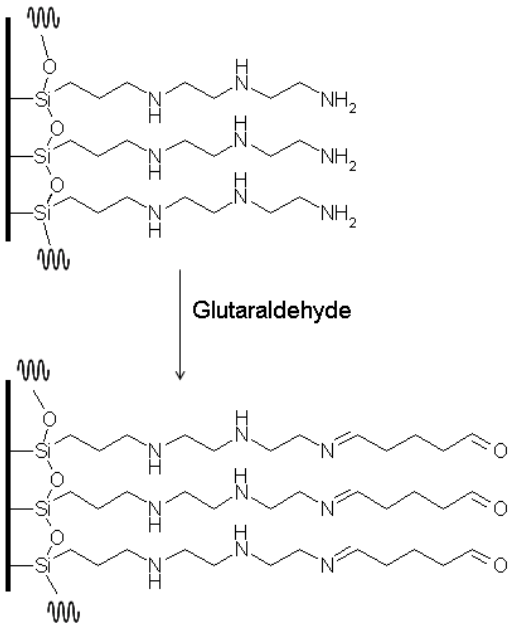


**Figure 1-3: Imine bond formation with glutaraldehyde on the surface of silica nanoparticles for BDA functionalization.**

Dextran amines are long stranded, branched polysaccharides (sugars) which have the known functionality of labelling axons in the nervous system [48]. These dextrans can be functionalized with a primary amine group through the addition of the amino acid lysine. The primary amine on lysine can be subsequently attached to the free aldehyde groups from the glutaraldehyde functionalized silica nanoparticles, using a modified method for imine production [49]. Dextrans have been demonstrated previously to enhance biocompatibility of nanoparticles [50], and to offer protection from destruction by enzymes in the body [51]. For that reason, they offer distinct advantages in their covalent attachment to nanoparticles.

The octadecyl (c18) functionalization of the nanoparticle can create a highly hydrophobic surface on the nanoparticle. This hydrophobic surface can potentially facilitate intermolecular interactions with the hydrophobic core of a cell's phospholipid

bilayer. This functionalization can potentially be accomplished through the reaction of a silica coated SPIO nanoparticle with trimethoxy(octadecyl)silane which binds covalently to a silica surface [52].

### 1.2.6 Characterization of nanoparticles

Studies of the surface functionalization of the nanoparticles have been shown in the literature with various different techniques including infrared (IR) spectroscopy[41] and inductively coupled plasma atomic absorbance spectrometry (ICP-AES)[53]. Studies of amine functionalization of the surface of lanthanide oxide nanoparticles was done through an examination of infrared spectroscopic characterization of distinct stretching bands in the region of 2900 – 3000 $cm^{-1}$ [54]. IR has been shown as an effective means of evaluating the functionalization of the magnetic nanoparticle.

Characterization of size is accomplished through examination with electron microscopy. Scanning electron microscopy (SEM) is a means of evaluating the size of nanoparticles[52].

## 1.3 *In vitro* Assessment of Nanoparticle Uptake

The mechanisms of the internalization of nanoparticles are varied. Previous studies have been done on the cellular uptake of nanoparticles, and it was determined that the efficiency of the nanoparticle uptake was based largely on two parameters: 1) the size of the nanoparticles, and 2) the functionalization of the surface of the particles. It was found that smaller particles were taken into cells with higher efficiency than larger ones [55]. Secondly, the functionalization of the particle was determinative in the particle uptake:

it was found that particles which bore a positive charge (such as a primary amine or amidine) were taken up into cells with higher efficiency than similarly sized nanoparticles with oppositely charged functional groups (such as carboxyl groups) [36, 38, 55]. Other functional groups can be used to enhance the uptake of nanoparticles [20, 56, 57]. Enhanced uptake with positively charged nanoparticles is likely due to an electrostatic interaction between the particle and the negatively charged phospholipid head group of the plasma membrane, as is the case in other cellular protein-membrane interactions [58]. It is likely that the positive charge of a nanoparticle attracts it to the cell membrane where it binds non-specifically to the cell membrane [59]. When an endocytosis event occurs in this proposed mechanism, the membrane is invaginated, the nanoparticles bound to the membrane can therefore be internalized within the endosome, and the particles cannot escape from the endosome due to their membrane binding. Different studies have shown that nanoparticles taken up into cells are sequestered into membrane bound structures characteristic of endosomes [53, 59]. In a neuron, endosomes are then trafficked through an active retrograde transport process to the soma where the endosomes fuse in the formation of lysosomes. This is the mechanism which has been described in the transport of the axonal tracer Fluoro-gold [60]. It is possible therefore, that nanoparticles encapsulated in endosomes undergo retrograde transport. In a study done on iron oxide nanoparticles with a highly positive surface charge, it was found that retrograde transport of the nanoparticles to the soma did occur [36]. Transport of nanoparticles conjugated to a wheat germ protein was also observed in neurons [37]. In quantum dots conjugated to nerve growth factor (NGF) it was found that particles could be transported in an *in vitro* co-

culture apparatus individually [20]. In a study done on bare silica nanoparticles in the ear where the particles were exposed to the facial nerve, posterior semicircular canal, and bulla, it was found that retrograde transport did occur in neurons with some nanoparticle fluorescence present in the brainstem of the experimental animals [61]. These previous results suggest that axonal transport of nanoparticles is possible.

Previous studies of silica-coated nanoparticles indicate that particles are internalized into membrane bound structures with a clatherin mediated process, and that the particles are found within lysosomal structures [62]. Conjugation of other functional molecules to nanoparticles have facilitated their uptake into cells, but the nanoparticles remained sequestered in vesicles, and this was the case with Cholera toxin subunit B functionalized nanoparticles [56]. Other biomolecules such as protamine sulphate conjugated to the nanoparticle facilitate highly efficient uptake; however, sequestering of the particles is still evident [23]. The sequestering of iron oxide nanoparticles functionalized with silica and amine groups, determined with Prussian blue light microscopic staining for iron, was corroborated with transmission electron microscopic (TEM) images in *in vitro* studies to be in lysosomal structures [53]. Tuning of the uptake of nanoparticles could be accomplished with the addition of an adenovirus capsule as a surface coating, allowing for pH dependent uptake [63]. In summary, the uptake of nanoparticles is dependent on charge, particle size and functionalization. Size determines the relative ease for entering the cell; if a particle is small enough, there is the possibility it can penetrate the plasma membrane directly[59]. Larger particles, however, require the process of bulk endocytosis to occur in order to trigger uptake. Particles with intermediate sizes are endocytosed by

various means. Charge determines the extent of interaction of the nanoparticle with the cell membrane enabling electrostatic interactions to drive the uptake of particles. Surface functionalization with certain receptor interacting biomolecules drives membrane receptor based processes, triggering the uptake of a nanoparticle in a process of endocytosis. Membrane bound structures such as endosomes play a significant role in the uptake and cellular interactions with nanoparticles, and are one of the most significant means of internalization.

## 1.4 *In vitro* Assessment of Nanoparticle Toxicity

The toxicity of nanoparticles is believed to originate through the production of reactive oxide species (ROS) [59]. The toxicity of the nanoparticle corresponds with the route of entry, with different mechanisms existing between inhalation into the lungs and inoculation. The formation of ROS leads to oxidative damage and necrosis and damage to lipids, proteins and DNA[64]. This is triggered when the particles come in contact with the cells causing a signalling cascade of ROS generation. Although the presence of nanoparticles in cells strongly triggers ROS generation, the chemical composition of the nanoparticle may enhance the production of ROS. Metal oxide nanoparticles such as iron oxide nanoparticles can further catalyze the production of ROS, thereby enhancing the toxic effects of a nanoparticle [65]. This occurs through a REDOX process with hydrogen peroxide when ferric iron is oxidized to ferrous iron, producing high superoxide levels [59]. This process is known as the Fenton reaction for the production of ROS [64]. Although the cell has mechanisms to enzymatically reduce ROS levels, high ROS levels ultimately lead to cellular necrosis. The oxidation state of the iron nanoparticle is of particular

importance with respect to toxicity. Ferric iron (3+) is more chemically inert than ferrous iron (2+) in REDOX reactions with an electrochemical drive for the oxidation of ferrous iron. Coupled with this reaction is the production of reactive oxide species *in vivo* in the Fenton process [59]. In a study done in *Escherichia coli*, $Fe_3O_4$ nanoparticles, which are a mixed valence state between ferrous and ferric iron, had higher toxicity than $Fe_2O_3$ nanoparticles which are composed of ferric iron alone. This study also correlated the oxidation of iron oxide nanoparticles with the production of ROS to cellular toxicity [66]. Passivating the surface with a more chemically inert molecule like silica of the iron oxide nanoparticles may be beneficial in reducing the overall particle toxicity; however, ROS production will occur by virtue of the nanoparticle's presence. This will produce hybrid iron oxide – silica nanoparticles.

Silica nanoparticles have been studied for their toxicity properties [67], and silica particles are of particular interest because of the chemical functionality diversity needed in this study. Silica is on its own capable of generating ROS by virtue of its chemical composition. Many signalling cascades may be involved *in vivo* for the production of ROS from inflammatory responses, but it is believed that a cellular response is to generate a burst of ROS to destroy foreign matter [68]. Although silica has been known for its pathological effects *in vivo* [64], when coupled with iron oxide nanoparticles, silica has been proposed to have the ability to reduce the exposed iron on the nanoparticle, reducing the ROS levels compared to iron oxide alone [65]. Silica may act as an effective means of encapsulation of the iron nanoparticle with a biocompatible advantage. Other nanoparticle surface functionalizations have been evaluated to reduce toxicity of

nanoparticles. These include polyethylene glycol, gold, and other biomolecules [69]. Silica was found to have some benefits for the reduction of toxicity with metal oxide nanoparticles; however, it is advantageous as a shell due to the wide range of chemical functionalizations which are possible.

## 1.5 *In vivo* Assessment of Nanoparticles

### 1.5.1 Axonal transport

It has been long known that the processes of axon transport are critical components of neuronal physiology and pathophysiology [70]. Axonal transport is critical in embryonic development, pathfinding, and apoptotic signalling [71]. Many diseases and abnormalities of the nervous systems are also caused by abnormalities in axonal transport. It has been suggested that diseases such as Alzheimer's, retinitis pigmentosa, and Huntington's disease are related to defects in normal axonal transport [70].

The mechanism of action of axonal tracers, and axonal transport is believed to exist through a multitude of cellular processes and machines; however, the process is composed of simple discrete steps which are interdependent and rate limiting [1]. At its most basic level, the processes of axonal transport are composed of: 1) cellular recognition, 2) cellular internalization, 3) cellular sorting, 4) cellular processing, 5) axon transport, and 6) potentially a sixth step of externalization of the tracer. Although these steps are described as being discrete, it must be understood that the processes are interdependent and act in sequence.

As tracer molecules are introduced into the nervous system, before any tracing can occur, the molecules must be internalized into the cells. This can occur through a process which is active, completely passive, or lie somewhere on this continuum. A schematic breakdown of the uptake processes is shown in Figure 1-4. Active processes can be driven by receptor medicated processes, such as receptor-ligand interactions. A tracer in this case would be a ligand with a high specificity for the receptors on the surface of neurons, triggering a process of receptor medicated endocytosis. Examples of tracers with this recognition process include neurotrophins such as nerve growth factor (NGF) and neurotrophin-3 (NT-3), or toxins such as cholera toxin and tetanus toxin. Specific recognition of this type guides the process of internalization and further processing. In contrast, however, recognition and later uptake can be non-specific and completely passive in nature. It is possible that tracer molecules interact with neurons though non-specific ligand-receptor interactions, driving the internalization of the tracer molecules, and this would include tracers acting as ligands driving receptor medicated internalization into any cell type. This would include molecules labelled with Human acquired immunodeficiency virus trans-activator of transcription (HIV-tat), for example [72, 73]. If cells recognize tracers as nutrients, internalization can also be driven, for instance in the case of dextran amines [1]. On the far end of the interaction spectrum are molecules which simply interact completely non-specifically with cells, and can interact with the cell plasma membrane through simple electrochemical or chemical interactions. When endocytosis does occur, these tracers become associated with endosomal structures. This is the case with the retrograde tracer Fluoro-Gold. Furthermore, chemical interactions are

possible between tracers and the cell membrane can drive the process of tracing. Hydrophobic interactions of the tracers with cell membranes can drive direct association with the hydrophobic core of the plasma membrane, and internalization never actually occurs, rather the molecule resides within the neuron plasma membrane. Examples of this mechanism include the tracer class with octadecyl functionality, including DiI and DiO. Other lipophilic dyes have been prepared with similar diffusion properties to DiI through the linking of fluorophores to non-polar lipophilic functional groups [74]. This type of tracer can be used for the labelling of tissue ex-vivo, and post-mortem[75, 76], thereby eliminating any possible mechanism of active transport. The specific mechanism of the initial recognition of the tracer molecule with neurons in large part dictates the uptake mechanism for the tracer, and therefore its action. Because cellular recognition and internalization is critically important in the mechanism of action in axon tracing, the conceptualization and design of tracers must account for maximal internalization through optimizing molecular recognition events or non-specific interactions with the plasma membrane.

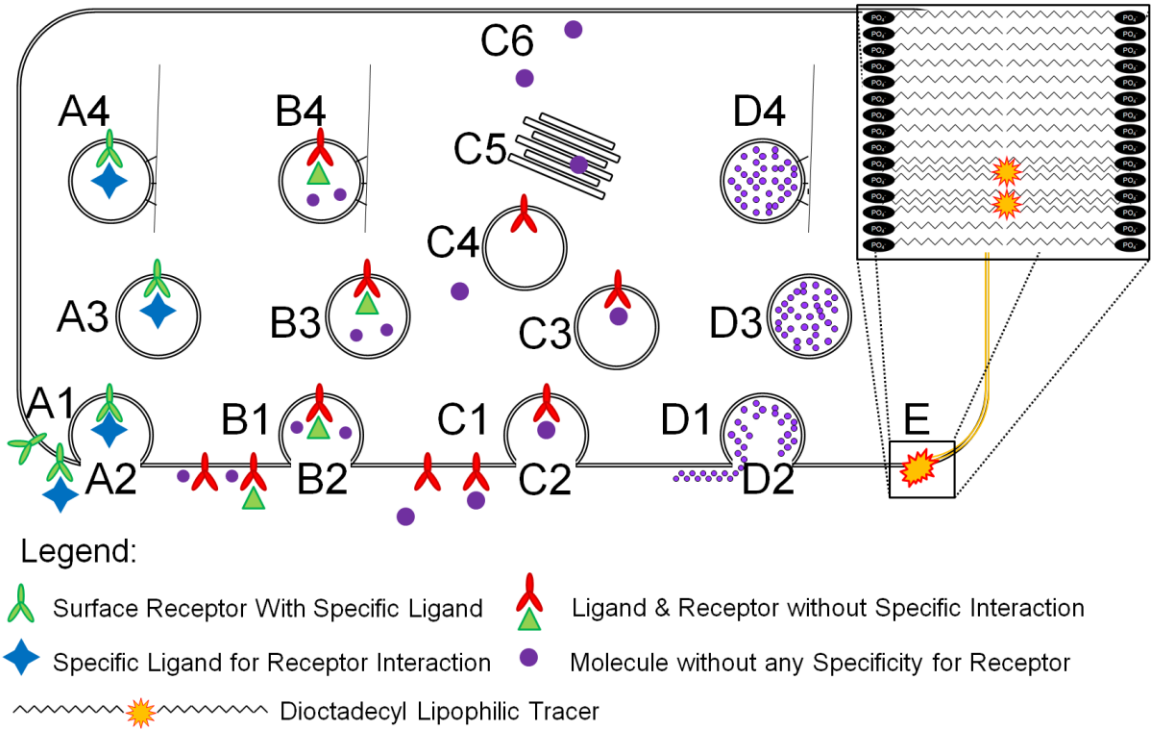


**Figure 1-4: Five mechanisms of cellular uptake of axon tracers.**
**A) Receptor mediated, where a specific cell receptor binds to its ligand (A1), and triggers endocytosis (A2) and endosome formation (A3), and binds to transport machinery on the cytoskeleton (A4). Non-specific endocytosis is triggered where ligands which are not specific to receptors can bind (B1), trigger uptake (B2), endosome formation (B3), and transport (B4). Other non-specific cell uptake occurs through ligand binding (C1), uptake (C2), endosome formation (C3), endosome release (C4), cellular processing in Golgi (C5), and passive diffusion throughout the cell (C6). The final mechanism is bulk endocytosis, where ligands in the extracellular matrix associate with the cell membrane (D1), are engulfed by endocytosis (D2 & D3), and are transported (D4).**

Receptor mediated endocytosis is frequently modulated through clatherin driven signalling [59]. This type of endocytosis accounts for the internalization of smaller volumes and small molecules. Larger volumes can be internalized through bulk endocytosis, modulated not through a receptor driven processes, but rather through the fusion of the

plasma membrane and the formation of endosomes, where they are concentrated and fused with lysosomal structures for degradation by the cell. These endosomes are frequently found within dendrites and axons, where their contents can be transported to the cell body for degradation through retrograde transport for concentrating endosomes and lysosomal fusion. Like the cellular recognition of tracer molecules, the mechanism of uptake largely dictates the type of transport which is to occur.

Transport of tracer molecules, can be accomplished through various processes including: fast axonal transport, slow transport, cytosolic diffusion, and membrane diffusion [1]. Fast axon transport is an active transport process whereby membrane organelles are fused with ATP-driven transport proteins which physically crawl down the length of actin fibres within the axon. These proteins are kinesin in the case of anterograde transport and dynein in the case of retrograde transport. This is a fast process, which can reach transport speeds of 400 mm/ day [1]. Axon tracers utilizing this type of transport are sequestered into membrane bound structures such as endosomes which are transported along the axon at high speeds. A schematic representation of this transport is shown in Figure 1-5. The other active transport mechanism which takes place within axons is slow transport which accounts for the transport of trans-membrane peptides [77].The peptides are linked to ATP-driven transport proteins which are able to physically move the plasma membrane lodged proteins. This active transport process only occurs in the anterograde direction, and has found little applicability for axon tracing in live subjects. Passive diffusion is another important mechanism in axon tracing and accounts for many of the tracers available. The tracers are able to enter into the cytosol

where, over a period of weeks, the tracers diffuse along the whole cell and into the processes, and axons. This process takes no energy input for the diffusion of the tracer; however, active uptake can be responsible for their internalization. Dextran amines act with this mechanism with active uptake and passive diffusion. Furthermore, membrane diffusion has strong applicability as axon tracers because the process is entirely passive, and this is a benefit because the tracer can be applied for post-mortem analysis of tissue. Like cytosolic diffusion, the tracer extends throughout the cell and labels the membranes. Because diffusion is passive and the entire cell will uniformly contain the tracer, the cell will be uniform in appearance when examined histologically. This has distinct advantages over tracers which are transported in membrane bound organelles because the tracers will be concentrated within the clusters of endosomes and lysosomes in the soma, and therefore not uniform in their labelling. However, a major disadvantage of a membrane diffusion tracer like DiI is that it can leak out of fixed tissue and mislabel other neurons or axons through any breaks in the plasma membrane [74 78].

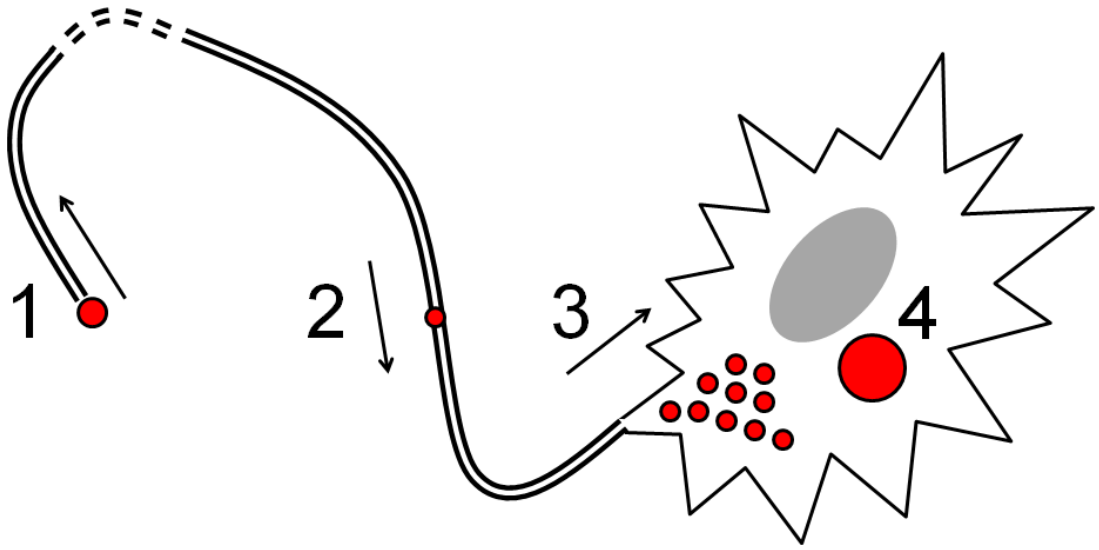


**Figure 1-5: Mechanism of retrograde axonal transport of endosomes.**
**A tracer is taken up into an endosome through a mechanism described above (1), the endosome is transported through active transport along the cytoskeleton (2), and endosomes are concentrated in the soma (3) where the endosomes fuse with lysosomes for cell processing and destruction (4). If the tracer resists degradation, it will stay in place forever.**

The clear advantage of the actively transported molecules is their speed, in contrast to the process of diffusion. The process of retrograde transport is shown schematically in Figure 1-5. This is contrasted to lipophilic tracers which are not transported at all and diffuse in the membrane, as shown schematically in Figure 1-6.

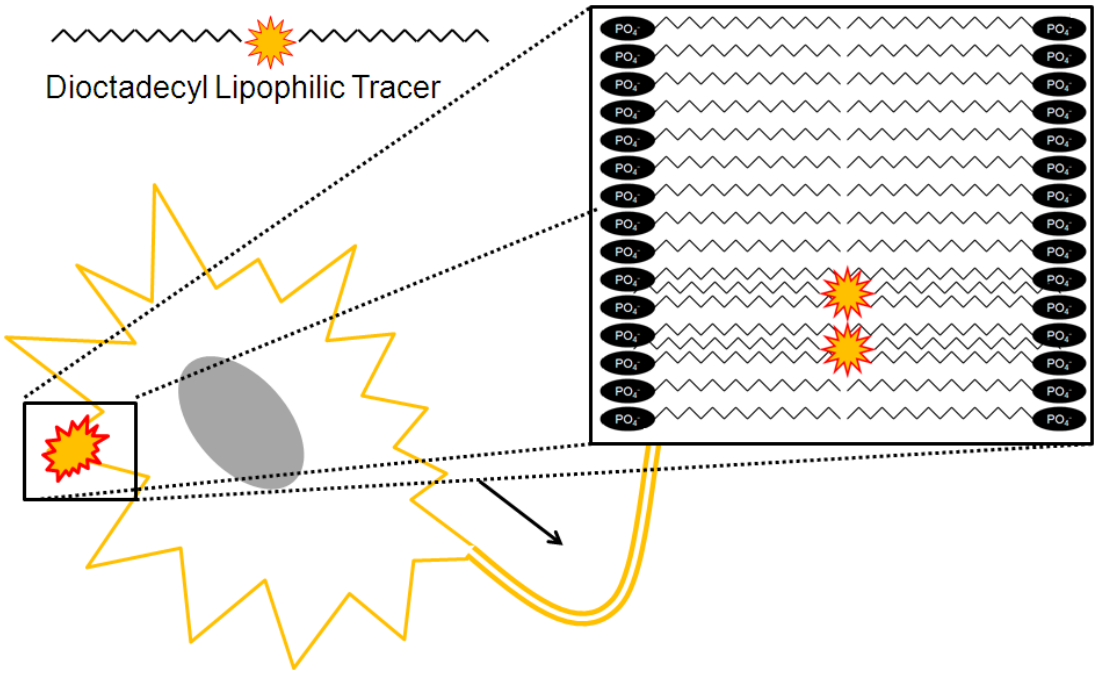


**Figure 1-6: Mechanism of dioctadecyl tracers such as DiI.**
**The lipophilic dye crystal contacts the cell membrane where it enters the hydrophobic core of the plasma membrane and diffuses passively throughout the cell membrane. Shown on the molecular level is how the lipophilic dye resides in the hydrophobic membrane core.**

The final step of axon transport and tracing is the externalization of the tracer. Some molecules, when reaching the axon terminals will be exported in vesicles into the synapse [1]. Other molecules will rest within the lysosomes until they are destroyed, or if the tracer is stable in the low pH and oxidizing environment of the lysosome, the tracer can stay for the life of the cell [60]. It is possible that when the tracer is externalized between pre and post-synaptic neurons, the tracing process can begin *de novo* in the post-synaptic neuron.

Based on the different mechanisms of uptake and axon transport of molecules, there has been the development of a wide range of molecules specifically for optical imaging of neuronal networks. These molecules were first selected based on their

properties in uptake and transport as described above, and for their optical functionality where a dye or fluorophore can be added and visualized. There exist 4 broad classes of tracers, as described in Table 1-1. Dextrans are polysaccharides which are taken up by neurons as nutrients and dissolve passively throughout the cytoplasm after first being processed by the Golgi apparatus, as they cannot be degraded by the cell[78, 79]. The mechanism is diffusion, and labelling takes a long time due to the passive process, but is uniform throughout the cell. Tracing is either retrograde or anterograde depending on where in the cell the injection is made. Lipophilic molecules containing dioctadecyl functional groups are hydrophobic in nature and diffuse into the hydrophobic core of the plasma membrane, and diffuse throughout the cell membrane[75, 76, 80, 81]. The tracing is passive and can be either retrograde or anterograde depending on the site of the lipophilic molecule application. Peptides interact specifically with cell receptors, are internalized into membrane bound structures such as endosomes, are transported actively, and the transport can be in either an anterograde or retrograde direction[1, 20, 82]. A broad last class of molecules is comprised of other tracers which diffuse or are transported into the cell by bulk endocytosis. These molecules are mostly transported in a retrograde direction to the cell body in endosomes for lysosomal fusion and destruction[1, 60].

**Table 1-1: Summary of functional groups in axonal tracers.**

| | Axon Tracer Functionalities | | | |
|---|---|---|---|---|
| **Functional Group** | **Dextran** | **Octadecyl** | **Peptide** | **Other/Charged** |
| **Structure** | 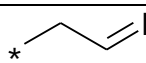 | 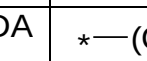 | 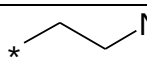 | *-OH |
| **Tracer (Example)** | Dextran Amine | DiI | CtB | Fluoro-Gold |
| **Charge** | Anionic | Neutral | Cationic | Neutral/Cationic |
| **Uptake** | Receptor Mediated | Membrane Diffusion | Passive Diffusion/ Receptor | Passive |
| **Transport** | Cytosolic Diffusion | Membrane Diffusion | Active Transport | Active Transport Diffusion |
| **Organelle** | Cytoplasm | Membrane | Endosome | Lysosome |
| **Direction** | Both | Both | Both | Both |

### 1.5.2 Magnetic Resonance Imaging for Axon Tracing

Magnetic resonance imaging (MRI) has been widely used in the field of neuroscience, with particularly widespread use in the clinical setting. The main advantages of MRI are that it does not use ionizing radiation, it can be applied serially over time, detailed tissue architecture can be visualized, and it is particularly well suited to imaging soft tissues. MRI is based on the interactions of the spin moments in the nucleus of an atom in a magnetic field, specifically the proton in hydrogen in this study [25]. The imaging applications of MRI in the brain and spinal cord have been increased with techniques such as diffusion tensor imaging (DTI) and with contrast agents. DTI measures the diffusion of water and, together with mathematical algorithms, can be used to reconstruct axon fiber tracts in three dimensions [14-16]. It has been used in the study of pathology in the brain and spinal cord. Although fiber tracts can be visualized, specific labelling of axon tracts as visualized by MRI cannot be directly confirmed with histology.

Chemical contrast agents for MRI include inorganic complexes of highly paramagnetic metals whose magnetic properties have effects on the speed of decay of the resonance signal. There are agents which have effects on both the decay times. The T1 and T2 times are the two time parameters which are critical in providing contrast in MRI, and characterize the varying differing magnetic resonance of protons in their specific chemical environment. T1 characterizes the spin-lattice relaxation of protons, and T2 characterizes spin-spin relaxation of the protons which differ depending on the molecular structure and intermolecular forces that a proton experiences[83]. Generally, complexes which are considered negative agents will affect T2 and appear hypointense compared to its surroundings. Positive contrast agents have an effect on creating a hyperintense region on T1 weighted images[25]. Examples of a negative agent would be iron (III) or dysprosium (III), and examples of positive agents would be gadolinium (III) or manganese (II). Magnetic nanoparticles have been used recently for their strong signal contrast enhancement potential, and furthermore offer the potential to be conjugated to other molecules to create multifunctionality. Superparamagnetic iron oxide (SPIO) nanoparticles have been used widely as contrast agents for MRI [84].

Other nanoparticle contrast agents are gadolinium oxide[85], manganese oxide [86, 87], and dysprosium oxide [88], and both gadolinium and manganese are positive contrast agents. These agents are beneficial since they are not present in high quantities in the body naturally, and can be potentially quantified in tissue with analytical chemical techniques. This is different than SPIO contrast agents, which when iron is quantified can be mistakenly identified as iron in the blood. All of these agents have been used chelated

in their ionic state in clinical applications [89]. Chelation reduces the toxicity of the injected agent. Conjugated ionic gadolinium incorporated directly into a silica nanoparticle superstructure has been suggested as a possible nanoparticle MRI contrast agent [67].

### 1.5.3 Nanoparticles in Axon Tracing

Few studies have examined axon tracing with MRI. Functionalized iron oxide nanoparticles have been injected into the rat sciatic nerve to image transport, and tracing of more than 1 cm was observable with MRI [36, 37]. These results were confirmed with histology. Another approach to axon tracing in rats was to examine the rat corticospinal tract with manganese enhanced MRI [16]. In this study, an aqueous solution of manganese (II) was injected into the rat sensorimotor cortex, and along with electrical stimulation, the corticospinal tract could be observed *in vivo*. Unfortunately, the labelling of the tract for MRI does not result in labelling of the tract for histological evaluation. Thus, this technique would not allow the simultaneous evaluations of the MRI labelled tract together with additional histological investigations and would limit evaluation of the fiber tract. For example, visualization of the interaction of astrocytes with the MRI labelled tract would be limited because although one could use immunohistochemistry to visualize astroctyes, the MRI labelled tract does not generate a histologically visualized label that would allow microscopic visualization of both the axon and the astrocyte.

The use of clinical MR systems with lower field strengths in the imaging of spinal cord injury (SCI) have been successfully accomplished in rats; however, tissue resolution is limited [10]. Resolution is improved at higher magnetic field strengths such as 3T, and quantification of nanoparticle concentrations in the rat brain can be accomplished through

an investigation of the T2 time as demonstrated by the examination of labelled progenitor cells [23]. Higher field strength magnets can provide greater resolution; however, SPIOs can be visualized in small quantities on clinical strength magnets, and due to the wide availability of clinical MRI, the tracers used in this thesis are tailored to clinical strength MRIs.

The prototype trifunctional nanoparticles were prepared as axonal tracers functionalized with each of the above class of axon tracers in Table 1-1 with the exclusion of specific peptide or neurotrophin molecules. Because the proposed mechanism of the particles is based on the incorporation of the nanoparticles into membrane bound structures for axonal transport, they were developed as retrograde tracers based on the fast transport and strong staining observed with Fluoro-gold [90]. The proposed mechanism for the uptake and transport of these axonal tracers on the cellular level is shown schematically in Figure 1-7. The octadecyl functionalized lipophilic membrane diffusion nanoparticles were also prepared for a study as a bidirectional tracer, but were examined *in vivo* with the same experimental setup as the tracers intended for retrograde transport to contrast differences. A schematic representation of the proposed mechanism of interaction of the lipophilic nanoparticles with the plasma membrane of neurons is shown Figure 1-8. The nanoparticles synthesized for application as anterograde tracers were functionalized with the tracer molecule biotinylated dextran amine (BDA).

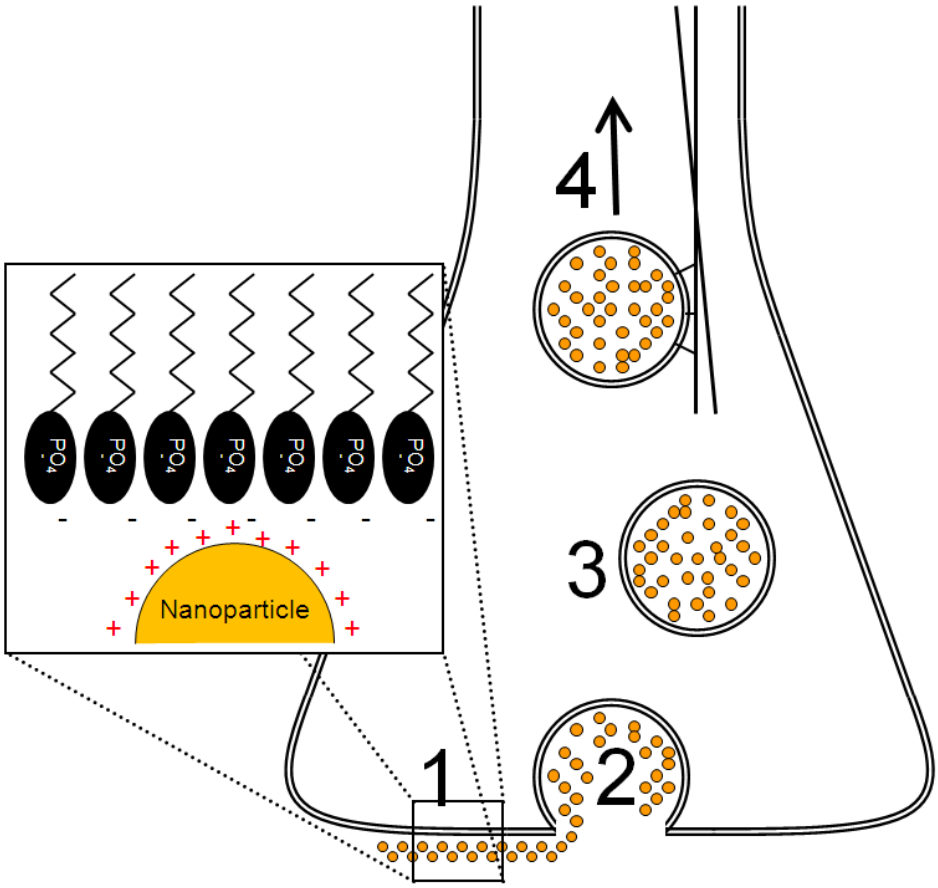


**Figure 1-7: Schematic diagram of proposed mechanism of action of dye coated, amine functionalized nanoparticles (SPIO+SiO2+RuBpy+NH2) as retrograde axon tracers at the terminal of an axon.**

**The amine functionalized nanoparticle binds to the negatively charged membrane (1), where the electrochemical interactions are shown in the exploded view. Invagination of the membrane occurs (2) and the nanoparticles bound to the membrane are engulfed to in the endosome (3). The endosome is actively transported by the cell with transport proteins along the cytoskeleton (4).**

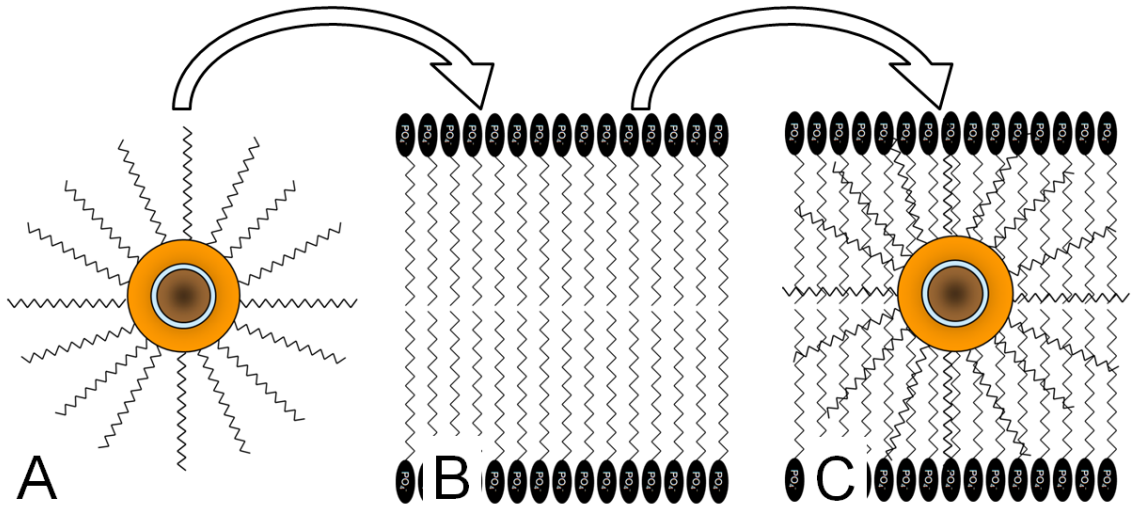


**Figure 1-8: Proposed mechanism of action of lipophilic (C18) functionalized nanoparticles as axonal tracers.**

**The lipophilic surface coating of the particle (A) interacts with the hydrophobic core of the plasma membrane (B) to be incorporated directly into the hydrophobic core of the membrane (C).**

## 1.6 *Ex vivo* Assessment of Nanoparticles

Lipophilic tracers can be used for the labelling of tissue ex-vivo, and post-mortem[75, 76]. Protocols have been developed for axon tracing in fixed spinal cord tissue with lipophilic dyes such as DiI and DiO [80]. This tracing is possible because the dioctadecyl functionalization of the axonal tracer diffuses within the plasma membrane and diffuses along the length of an intact membrane, which includes extension into axons. This mechanism is shown in Figure 1-4 and Figure 1-6. This mechanism is experimented with *in vivo*; however, lipohilic diffusion of the octadecyl functionalized nanoparticles should be expected to take place *ex vivo* in fixed tissue. Quantification of

diffusion of octadecyl functionalized nanoparticles with respect to conventional lipohilic dyes such as DiI can determine the extent of nanoparticle diffusion.

# Chapter 2: Methods

## 2.1 Nanoparticle Preparation

### 2.1.1 SiO2 Coating of SPIO nanoparticles

The silica functionalized SPIO nanoparticles (SPIO+$SiO_2$) was done with the polymerization of the silica precursor tetraethoxysilane (TEOS)[62]. This was done by first suspending Prepared SPIO nanoparticles (0.11 g) (Sigma-Aldrich) (FW=231.54 g/mol) in 3.22 mL de-ionized water. The particles were sonicated until a uniformly brown colloidal solution was seen, which took approximately 5 minutes. The suspended particles were then mixed into a solution containing 14.4 mL water, 13.7 mL ethanol, and 0.6 mL of tetraethoxysilane (Sigma) (TEOS). 1.5 mL of concentrated ammonium hydroxide was added to the solution to initiate the polymerization of silica. The particles were stirred for 4 hours at room temperature, and were washed with deionized water three times and ethanol three times. For the washing procedure, the particles were precipitated with a magnet, and the supernatant was drained off, and the particles were sonicated in the washing solution to re-suspend the particles and remove any physically adsorbed contaminants. The washed particles were suspended in 10 mL of ethanol, at an approximate concentration of 1 % iron oxide weight by volume. The particles were stored at room temperature and sonicated before use.

### 2.1.2 Dye coating of SPIO nanoparticles

The tris-2,2'-bipyridine ruthenium bipyridine (RuBpy) coated silica functionalized SPIO nanoparticles, abbreviated SPIO+SiO2+RuBpy henceforth were prepared as follows[46]. Using the SPIO+SiO2 nanoparticles which were prepared at 1% in ethanol, the dye functionalization was accomplished. Two millilitres of the prepared SPIO+SiO2 particles, 0.5 mL of 50 mg/mL aqueous ruthenium bipyridine (Sigma), and 0.75 mL TEOS were added to 10 mL of Ethanol with rapid mechanical stirring. Once mixed, 0.75 mL concentrated ammonium hydroxide was added to initiate the polymerization of silica. The particles were stirred for 3 hours before washing them three times with ethanol with magnetic separation. The fluorescence of the particles was verified by examining both the dye coated, and non-dye coated SPIO+SiO2 nanoparticles by drying one drop on a glass microscope slide and examining the slide with UV fluorescence excitation. The particles were disbursed in 2 mL of ethanol, at a concentration of 1% iron oxide by weight.

### 2.1.3 Amine functionalized SPIO nanoparticles

The amine functionalization of the silica nanoparticles was accomplished using the amine-silane precursor $N^1$-(3-Trimethoxysilylpropyl)diethylenetriamine (DETA) [49]. This precursor was used to functionalize both dye-functionalized and non-dye-functionalized nanoparticles using SPIO+$SiO_2$+RuBpy and SPIO+$SiO_2$ nanoparticles, respectively. The dye coated, amine functionalized nanoparticles are abbreviated SPIO+$SiO_2$+RuBpy+$NH_2$. One mL of the SPIO+$SiO_2$+RuBpy particles was added to 5 mL ethanol, along with 25 μL of TEOS and 0.1 mL DETA. The reaction was started with

0.1 mL ammonium hydroxide, and the particles stirred for 3 hours at which point they were washed 3 times with ethanol using magnetic separation. The particles were disbursed in 1 mL of ethanol at a concentration of approximately 1% with respect to weight percent of iron oxide in a volume.

### 2.1.4 Octadecyl Functionalized Nanoparticle Synthesis

Octadecyl amine surface functionalized SPIO nanoparticles with a fluorescent shell ($SPIO+SiO_2+RuBpy+C_{18}$) were prepared through a similar route of functionalization as the other nanoparticle functionalizations, and were based on other methods for the preparation of silica nanoparticles[52]. One mL of 1% $SPIO+SiO_2$ nanoparticles was added to 5 mL ethanol along with 375 μL of TEOS, 250 μL of 50 mg/mL RuBpy, and 200 μL of Trimethoxy(octadecyl)silane (C18). Ammonium hydroxide (375 μL) was used to initiate the reaction. The particles were stirred on a magnetic stir plate for 3 hours, at which point they were washed three times in ethanol, separating the particles with magnetic separation between washes. The particles were disbursed in 1 mL ethanol, and stored at room temperature until use. To fabricate $SPIO+SiO_2+C_{18}$ particles, the above procedure was without adding the RuBpy dye.

### 2.1.5 Biotin Dextran Amine Functionalization of SPIO Nanoparticles

The nanoparticles prepared with an amine group were further functionalized with biotin dextran amine (BDA) through a covalent imine bond [49], to produce SPIO+SiO2+RuBpy+BDA nanoparticles. Half a millilitre of the 1% SPIO+SiO2+RuBpy+NH2 particles were first centrifuged for 10 minutes at 10,000 rpm

and washed with deionized water three times with centrifugation. A solution of 1 ml 5% aqueous glutaraldehyde was added to the particle pellet, and the particles were re-suspended in solution with sonication. The particles were next incubated in the glutaraldehyde solution for 2 hours at 37°C, then centrifuged 10 minutes at 10,000 rpm and washed with water three times with centrifugation. 100 μL of the original 500 μL of the particles were then pelleted and suspended in 1% BDA (Invitrogen) solution in PBS and incubated for 2 hours at 37°C in. The particles were then incubated for 30 minutes at 37°C in 1 mL of sterile aqueous 30 mM glycine to saturate the remaining aldehyde sites. Washing was performed with centrifugation 3 times with sterile PBS, and the particles were stored at 4°C until use in 0.1 mL PBS.

## 2.2 Nanoparticle Characterization

Particles were characterized with magnetic resonance imaging, UV-visible spectroscopy, scanning electron microscopy, infrared spectroscopy, and fluorescence spectroscopy.

### 2.2.1 Magnetic Resonance Imaging

Particles were characterized with MRI for their contrast enhancement properties. One millilitre of particles were dispersed in water at decreasing logarithmic concentrations from$1x10^{-7}$ M to $1x10^{-1}$ M SPIO in deionized water, and compared to water controls. Particles were imaged with both TI and T2 weighted sequences to determine the contrast enhancing potential of the particles.

### 2.2.2 Infrared Spectroscopy

Particles which were washed in ethanol were pelleted, and the ethanol supernatant was drained off. The remaining supernatant was removed by drying in a vacuum desiccator overnight. The nanoparticle powders were weighed and 5-10 mg of the nanoparticle powder was compacted into an approximately 0.1 g potassium bromide pellet under high pressure. The potassium bromide pellets were mounted in an ABB Boemen MB Series scanning IR spectrophotometer, and the IR spectrum was collected between 600 $cm^{-1}$ and 4000 $cm^{-1}$.

Liquid suspensions of nanoparticles were deposited on NaCl salt disks and the IR spectrum was collected with an ABB Boeman MB Series scanning IR spectrometer in the range of 600 $cm^{-1}$ to 4000 $cm^{-1}$.

### 2.2.3 UV-Visible Spectroscopy

Determination of chemical properties was done by diluting the nanoparticle solutions with various functional groups in deionized water and imaging was done with a Cary 3 UV-visible spectrophotometer scanning in the 200 nm to 900 nm range.

Concentration determinations were made with a Perkin Elmer UV visible spectrophotometer. Concentration determinations were made using a standard dilution method with application of the Beer-Lambert law. A range of standard SPIO nanoparticle concentrations between 0.1 mM to 100 mM was prepared and diluted $1/10^{th}$. A further $1/10^{th}$ dilution was made in a 1 cm cuvette, and particles were measured with a water standard at 400 nm (with 4 nm slit width), and the concentrations of the different nanoparticles with different functional groups were calculated.

Determination of iron concentration in the SPIO nanoparticles was done using Prussian Blue staining as a method for determination of aqueous ferrous and ferric iron [23]. Fifty μL of nanoparticle solutions in water were added to 450 μL of 5% potassium ferrocyanide for a period of 5 minutes. To that, a 5% HCl solution was added for at least 20 minutes, and the solution was further diluted into a 3 ml in a 1 cm cuvette. The absorbance was measured with a Perkin Elmer UV-visible spectrophotometer at 410 nm with a 4 nm slit width, and the absorbances were plotted as a function of particle concentration between 0.1 mM and 20 mM with respect to iron.

### 2.2.4 Fluorescence Spectroscopy

The fluorescence spectrum was collected using a Cary Eclipse Fluorescence Spectrometer with excitation at 460 nm with a 10 mm quartz cuvette. The particles were separated with a magnet placed inside the spectrometer to observe the differences in fluorescence intensity due to precipitation of the nanoparticles in the presence of an applied magnetic field.

### 2.2.5 Scanning Electron Microscopy

Nanoparticles were air dried overnight, and the powder form of the nanoparticles was mounted onto double sided tape on an aluminum mounting bracket for SEM. The particles were sputter coated with a less than 20 nm coating of gold/platinum under vacuum. The particles were imaged with a Tescan Vega-II XMU scanning electron microscope at Carleton University.

## 2.3 *In Vitro* Nanoparticle Assessment

### 2.3.1 Neural Progenitor Cell Culture

Animal protocols were approved by the Ottawa Hospital Research Institute Institutional Animal Care Committee in accordance with guidelines by the Canadian Council on Animal Care. Cell culture was done of adult rat neural progenitor cells (NPC) based on the protocol developed by Kulbatski et al [91]. Cells were harvested from female Sprague Dawley rats weighing between 100 and 150 g. Rats were deeply anesthetized with isofluorane, and decapitated with a rodent guillotine. The spinal columns were then dissected out using scissors, dipped in 70% ethanol and stored until use in dissection media. Dissection media was composed of 87% α-minimal essential media (α-MEM) (Gibco–Invitrogen; Burlington, ON, Canada, 12492-013), 10% Fetal Bovine Serum (Gibco–Invitrogen, 12483-020), 1% L-Glutamine (Gibco–Invitrogen, 25030-081), and 2% Penicillin and Streptomycin (Gibco–Invitrogen, 15140-122).

Using sterile instruments the spinal cord was isolated. The spinal cord was removed from the vertebrae after bilateral laminectomy was performed along the length of the spinal column from the cervical to lumbar spine and cutting the nerve roots with microscissors. The spinal cord was transacted with a razor blade 1 mm rostral to the conus medullaris, and the entire length of the spinal cord was further dissected for cell harvesting.

Harvesting of the spinal neural progenitor cells from the ependymal zone was done by exposing the grey matter and central canal along the ventral fissure and folding the cord open in half. Tissue from the grey matter was isolated from the white matter

with fine tipped forceps, and the cells were isolated in a sterile tube containing the dissection media.

The cells were separated using protocols previously described by Kulbatski and others [91]. Cells were suspended in 15 mL sterile centrifuge tubes, in dissection media, and were triturated 20 times with a polished fine tip Pasteur pipette. The solution was centrifuged at 200 rpm for 2 min and the supernatant was drawn by aspiration and reserved in another sterile tube. Two mL of dissection media was added to the pellet where it was triturated 20 times, spun at 200 rpm for 2 min and supernatant was added to the previously reserved supernatant. This process was repeated two additional times, and the tube containing the collected supernatant was centrifuged at 1500 rpm and the pellet was dispersed in culture media containing 98% Dulbecco's modified eagle media F12 (DMEM/F12) (Gibco–Invitrogen, 10565-042), 1% L-Glutamine (Gibco–Invitrogen, 25030-081), 1% $N_2$ Supplement (containing: 10000mg/L human transferrin, 500mg/L insulin recombinant full chain, 0.63mg/L progesterone, 1611mg/L putrescine and 0.52 mg/L selenite) (Gibco–Invitrogen, 17502-048) in 0.1% BSA (Fisher Sci, PI-77110) PBS and fibroblast growth factor-basic (FGF) 20ng/ml (Peprotech, 100-18B) and epidermal growth factor (EGF) 20ng/ml (Peprotech, Rocky Hill, New Jersey, 100-44). Cells were plated into six well plates with each well containing 5 mL of media. The cells were grown for 7 days in these conditions, at which point they were passaged. Briefly, cells were drawn into 15 mL tubes, centrifuged for 5 min at 100 rpm, and pelletted withdrawing all but 1 mL of supernatant. The mixture was triturated 40 times with a 1 mL sterile pipette. The cells were equally distributed into 90 wells of a 96 well plate, and

supplemented with growth media to a volume of 150 μL and were left to grow at 37C for 7 days. Cells were then differentiated for 7 days before incorporating the nanoparticles. This was done by replacing the used media with culture media without EGF and FGF supplementation. In each experiment, PBS was added for the duration of the experiment as a control, and 0.3 % hydrogen peroxide was added 24 hours before the experimental endpoint as a positive control for TUNEL and Trypan blue.

### 2.3.2 Nanoparticle Cellular Uptake *in vitro*

The uptake of nanoparticles was assessed through two means. Firstly, the particles were stained histologically with Prussian blue to determine the uptake of iron into the cells, and determine roughly where the iron is located, and secondly through the study of the fluorescence of the nanoparticles within the cells, sectioned optically with confocal microscopy. All experiments were done with the incubation of nanoparticles for 7 days with the spinal neural progenitor cells, and the experimental parameters are shown in Table 2-1.

Prussian blue staining of the cells in the 96 well plates was accomplished by fixing the cells for 30 minutes with 4% paraformaldehyde. Aspirating between steps, the fixative was washed 3 times with PBS and 150 μL of 5 % potassium ferrocyanide was added for a period of 5 minutes, and 150 μL 5 % hydrochloric acid was added to the potassium ferrocyanide in the well for 20 minutes. The stain was removed, and the wells were washed 3 times with PBS. Cells were counterstained for 5 minutes with a 0.1 % nuclear fast red solution in 5 % aluminum sulphate, and washed 3 times before imaging.

The plate was imaged at 20 times magnification with an inverted optical microscope, and quantification of the Prussian blue labelled cells was done manually.

**Table 2-1: Parameters investigated for *in vitro* assessment of nanoparticles.**
**Number of independent repetitions indicated for each concentration for particular in vitro technique. Each repetition contains cells harvested from two rats * Indicates that TUNEL cannot be done for nanoparticles containing dye due to fluorescence overlap of nanoparticle with TUNEL stain. ** indicates that fluorescence microscopy was only done for the particle variation which contained fluorescence dye.**

| | | | *In vitro* Nanoparticles Assessment | | | |
|---|---|---|---|---|---|---|
| | | | Cellular Toxicity | | Cellular Uptake | |
| Nanoparticle Type | Dye Present | Concentration (mM) | TUNEL | Trypan Blue | Prussian Blue | Fluorescence Microscopy |
| SPIO | - | 0.1, 1, 10 | (n=3) | (n=3) | (n=3) | (n=3) |
| SPIO+$SiO_2$ | - | 0.1, 1, 10 | (n=3) | (n=3) | (n=3) | (n=3) |
| SPIO+$SiO_2$+RuBpy | √ | 0.1, 1, 10 | * | (n=3) | (n=3) | (n=3) |
| SPIO+$SiO_2$+RuBpy+C18 | √ | 0.1, 1, 10 | * | (n=3) | (n=3) | (n=3) |
| SPIO+$SiO_2$+RuBpy+$NH_2$ | √ | 0.1, 1, 10 | * | (n=3) | (n=3) | (n=3) |
| SPIO+$SiO_2$+RuBpy+BDA | √ | 0.1, 1, 10 | * | (n=3) | (n=3) | (n=3) |
| SPIO+$SiO_2$ | - | 0.1, 1, 10 | (n=3) | (n=3) | - | ** |
| SPIO+$SiO_2$+C18 | - | 0.1, 1, 10 | (n=3) | (n=3) | - | ** |
| SPIO+$SiO_2$+$NH_2$ | - | 0.1, 1, 10 | (n=3) | (n=3) | - | ** |
| SPIO+$SiO_2$+BDA | - | 0.1, 1, 10 | (n=3) | (n=3) | - | ** |
| Control (PBS alone) | - | 0 | (n=3) | (n=3) | (n=3) | (n=3) |
| Control ($H_2O_2$ 24 h) | - | 0 | (n=3) | (n=3) | (n=3) | (n=3) |

Confocal microscopy and optical sectioning of the cells incubated with the nanoparticles was done with a Nikon C1 inverted optical microscope. A purpose built microscope stage capable of accepting 96 well plates was routed from a 1/4” clear Lexan plastic sheet. The nanoparticle fluorescence was excited with an Argon ion laser (Melles Griot) at 488 nm and emission at 514 nm, and the topography of the cell was determined through the transmitted light image at 488 nm. Optical Z-stacking was done, and a three

dimensional reconstruction of the cell was made. Determination of fluorescence within the boundaries of the cell membrane versus outside the cell membrane were done by examining the fluorescence in orthogonal projection of the three dimensional image of the neural progenitor cells.

Fluorescence microscopic measurements of the cells with the nanoparticles was done with Hoechst labelling. Hoechst was added to wells at a 1:1000 dilution from the stock solution (Invitrogen) for a period of 30 minutes. The wells were washed 3 times with PBS. Imaging was done with a long-pass UV filter pass filter, and photographed with a color camera capable of distinguishing the green emission from Hoechst (green) and the nanoparticles (orange). The filter used for this purpose was a 360 nm excitation bandpass filter with a 400 nm long pass emission filter (Chroma Technology Corp.). This filter was capable of distinguishing Hoechst from the fluorescence of nanoparticles, as the fluorescence appeared green and red respectively.

## 2.4 *In vitro* Assessment of Toxicity

Due to the overlap of the nanoparticle dye with the quantification of secondary antibodies used in the TUNEL stain, the nanoparticles were prepared without the inclusion of the RuBpy dye. However, because the nanoparticles relevant for *in vivo* studies were those with the RuBpy dye, it was necessary to investigate any additional toxic effects the dye would incur to the nanoparticles. To accomplish this without the use of a fluorescent marker, the bright field microscopic membrane permeabilization marker Trypan Blue was incorporated directly into the wells to assess toxicity. The

measurements of Trypan blue and TUNEL were compared for both the groups containing the dye, and the groups prepared without the dye inclusion.

For trypan blue staining, staining was done directly in the culture plate, and wells were examined without fixation based on Marchenko *et al*[92]. The culture media was aspirated, and 5 µL of fresh culture media was added. To this 5 µL of freshly filtered 0.4% trypan blue (Invitrogen) was added. Wells were examined with light microscopy and three separate fields of view from each well were photographed. The fraction of cells labelled with trypan blue compared to total cell counts was quantified manually with Image J. Results were displayed graphically with standard error representations.

TUNEL staining for neural progenitor cells was performed as described by Melanson-Drapeau *et al* [93]. TUNEL was performed using the *in vitro* cell death detection kit (Roche) following the manufacturer's instructions. Each well was imaged for three independent fields of view, and quantification was done manually with Image J to determine the ratio of TUNEL positive cells. Quantification and statistical analysis with ANOVA was done with Microsoft EXCEL 2007 with data analysis package.

## 2.5 *In vivo* Assessment of Nanoparticles

Studies of axonal tracers *in vivo* with imaging focused on the application of anterograde axonal tracers injected into the sensory-motor cortex of adult rat brains and retrograde tracers implanted into the spinal cord of adult Sprague Dawley rats. Quantification of axon tracing was done with magnetic resonance imaging (MRI) and histology.

Animal protocols were approved by the Ottawa Hospital Research Institute institutional animal care committee following guidelines established by the Canadian Council on Animal Care (CCAC).

### 2.5.1 Anterograde Tracer Injections

The injection of the nanoparticles axon tracers was done surgically with the aid of a stereotaxic frame. Adult female Sprague Dawley rats (230-430 g) were anesthetized with 2-4 % isofluorane in oxygen at 1.5 L/m. The rats were mounted with ear bars in the stereotaxic frame and were prepared for surgery with shaving their heads, injections with 3 mL sub-cutaneous bolus of normal saline, and cleaning of the surgical site with Betadine. All surgical procedures were done with the assistance of a Zeiss operating microscope. A 1.5 cm long midline incision was made along the sagittal suture and the connective tissue on the skull was dissected with a scalpel blade locating the bregma as a landmark. A craniectomy was preformed with a surgical drill, and a 5 mm x 10 mm right craniotomy was performed. The medial border of the craniotomy was 1 mm lateral to the bregma and the anterior border was 1 mm anterior to the bregma. Bleeding was controlled with packing of sterile gauze. Any observations of damage to the brain or bleeding were noted when inspecting the craniectomy site; however, there were no differences observed between groups. The manipulator arm was mounted to the stereotaxic frame, in preparation for the injections.

For the tracer injections, a 200 μm tipped glass needle with a 10 μL Hamilton syringe was attached to the head of the manipulator arm on the stereotaxic frame, and the needle was localized to the bregma. The operating microscope was oriented for

visualization of the brain, injection sites and bregma. The glass needle was loaded with the 1% BDA solution (n=4), 10 mM SPIO+SiO2+RuBpy+BDA (n=4), and 10 mM SPIO+SiO2+NH2 (n=5), using new glass needles with tips of very similar sizes. 5 injections of 1 μL at 5 different sites were made in each rat brain to a total of 5μL solution per rat, and each injection was timed for 3 minutes with the needle remaining in place. The first injection site was 2 mm lateral and 0.5 mm anterior to bregma; the second site was 1 mm posterior to the first; the third site was 1 mm posterior to the second; the fourth was 0.5 mm anterior and 1 mm lateral to the third; and the fifth site was 1 mm anterior to the fourth. The injection site location is shown schematically in Figure 2-1 where the anatomical landmarks, craniectomy site, and coordinates of the injection sites are shown as viewed during surgery looking down onto the rat skull. At each site, the needle was inserted 1 mm below the surface of the brain for injection.

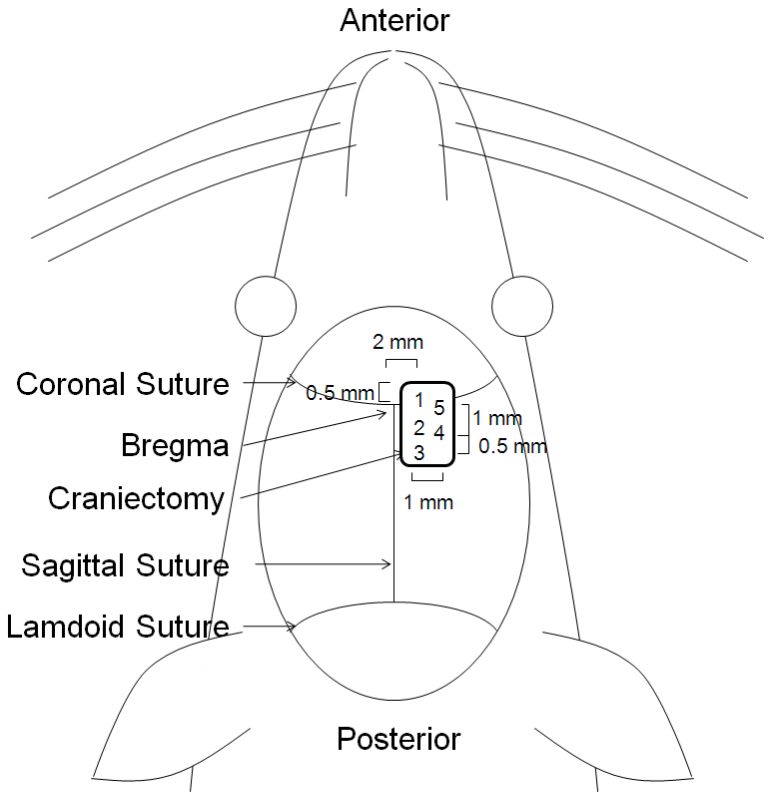


**Figure 2-1: Schematic diagram of rat skull viewed during surgery looking down on the rat head.**
**The anatomical references and site of the craniectomy window are labeled along with the coordinates and separation of the injection sites numbered 1-5.**

Once the injections were completed, the manipulator arm was removed, and the rat scalp was closed with 3-0 prolene sutures. Rats were given a bolus of buprenorphine at 0.1 mg/kg post-operatively. Rats were monitored and weighed daily for one week, and then weighed weekly for the duration of the experiments. MR imaging was done one day after injection, and three weeks after injection. These time points were chosen so that a baseline could be established on the first day, and three weeks is a time point typically used for BDA staining. After three weeks, a potential decrease in axon tracing staining

can be observed[90]. MRI scanning could only be done on at one week intervals due to access to the facilities. Animals were sacrificed immediately following the MRI to compare histology results to MRI; imaging was done at night, and the animals were sacrificed the following morning.

Three animals were excluded from the study in the SPIO+SiO2+NH2 group because of premature death. Two rats died during surgery (n=2), and n=1 rat died while anesthetised with ketamine/xylazine for MRI. A summary of the numbers in the animal experiments is shown in Table 2-2.

**Table 2-2: Summary of anterograde nanoparticle tracer analysis *in vivo*.**

| | Anterograde Nanoparticle Tracer Type *In vivo* | | |
|---|---|---|---|
| | BDA (Control) | SPIO+$SiO_2$+RuBpy+BDA | SPIO+$SiO_2$+RuBpy+$NH_2$ |
| Total Number | 4 | 4 | 5 |
| Died before experimental endpoints* | 0 | 0 | 3 (2 surgical anesthetic complications and 1 during anesthesia for MRI) |
| Excluded from analysis | 0 | 0 | 0 |
| Total Number Included | 4 | 4 | 2 |

### 2.5.2 Retrograde Tracer implantations

Retrograde tracers were surgically inserted into a transected spinal cord. Adult female Sprague Dawley rats (230-430 g) were anesthetized with 2-4 % isofluorane in oxygen stream at 1.5 L/m. The rats were mounted with ear bars in the stereotaxic frame and were prepared for surgery with shaving the thoracic region, injections with 3 mL sub-cutaneous bolus of normal saline, and preparing the surgical site with Betadine. All surgical procedures were done with the assistance of a Zeiss operating microscope. A five

cm long midline incision was made along the back centered at the eighth thoracic level. The muscles along the spinal column were dissected with a scalpel blade, and a laminectomy from the seventh to ninth thoracic level was done with 9 mm serrated malleus nippers (Storz); all bleeding was controlled with packing of gauze or Surgifoam. The spinal cord was lifted with a glass hook, and completely transected with microscissors. A pledget of sterile Surgifoam approximately 3 $mm^3$ was soaked in a 40 μL solution of tracer. The tracers incorporated in this fashion were PBS control (n=3), SPIO+SiO2+RuBpy (n=5), SPIO+SiO2+RuBpy+NH2 (n=5), and SPIO+SiO2+RuBpy+c18 (n=4). The muscle layers were closed with 3-0 vicryl braided sutures, and the skin was closed with 3-0 prolene monofilament sutures. The rats were given a bolus of 0.1 mg/kg buprenorphine, and their bladders were manually expressed 3 times daily. Urinary tract infections were detected by the presence of blood in the urine, and infected rats were treated with 5 days of sub-cutaneous boluses of ampicillin twice a day. Tracers were implanted in the animals for a total of three weeks. Weekly MR imaging was done with the first MRI performed one week after implantation

The summary of rats included in each group, and any removal of animals from the analysis is tabulated in

Table 2-3. In the SPIO+SiO2+RuBpy group, n=1 animal died during the surgery, and was excluded from analysis. In the control group and SPIO+SiO2+RuBpy+NH2 group, n=1 animal was perfused from each group 4-7 days before the experimental endpoints due to weight loss exceeding 25%. Because these animals were imaged with MRI at the final timepoint along with the other animals in the group, they were not excluded from

histological analysis and were treated with the same tissue processing. From the SPIO+SiO2+RuBpy+NH2 group, n=1 animal did not have access to the MRI due to availability, and was excluded from analysis.

**Table 2-3: Summary of animal groups in retrograde nanoparticle tracer analysis *in vivo***

| | Retrograde Nanoparticle Tracer Type *In vivo* | | | |
|---|---|---|---|---|
| | PBS (Control) | SPIO+$SiO_2$+ RuBpy | SPIO+$SiO_2$+ RuBpy+$NH_2$ | SPIO+$SiO_2$+ RuBpy+C18 |
| Total Number | 3 | 5 | 5 | 4 |
| Died before experimental endpoints* | 0 | 1 (Died during surgery) | 0 | 0 |
| Perfused to due high weight loss >25% | 1 (After Final MRI – not excluded) | 0 | 1 (After Final MRI – not excluded) | 0 |
| Examined at Multiple endpoints with MRI and used for further analysis | 3 | 4 | 3 (1 animal could not be imaged - no MRI access) | 4 |
| Excluded from MRI analysis | 0 | 0 | 0 | 1 (scoliosis) |
| Total Number (n=) | 3 | 4 | 3 | 3 |

### 2.5.3 Magnetic Resonance Imaging *in vivo*

Magnetic resonance imaging was done with a 3 T Siemens Magnetom TRIO clinical imager at the Civic Campus of the Ottawa Hospital. Rats were anesthetized with a ketamine/xylazine cocktail at 60 mg/kg ketamine, and 7.5 mg/kg xylazine for rats with spinal cord injections and 100 mg/kg ketamine, and 10 mg/kg xylazine for rats with spinal cord injections, and transported in filtered rat cages to the MRI suite. The difference in anaesthetic concentrations was due to differences in the protocols at the time of the experiments. The coil reference marks were centered on the spinal cord or

brain depending on the injection site. The rats were fixed in position in a wrist coil, and centered on the table.

The imaging sequence for the rats with the anterograde tracers was a localizer sequence followed by sagittal and axial gradient echo sequences. In the case of rats with retrograde tracer injections in the spinal cord, only a sagittal gradient echo imaging sequence followed the localizer sequence.

### 2.5.4 Anterograde Tracer Imaging

The analysis of the anterograde tracers, BDA (n=4), SPIO+SiO2+RuBpy+BDA (n=4), SPIO+SiO2+NH2 (n=3), was done through image analysis with ImageJ. Gradient Echo MR Images acquired on the 3 T Siemens TRIO were exported to a format analysable with Image J using the Siemens Syngo Fast-View software and calibrated with mm markings. Both the depth of injection and area of the injection site visualized was manually highlighted as a region of interest, and were measured 3 times for each rat and the measurements for area were averaged. Measurements were made of both the axial and parasagittal MR images. The measurements for each of the groups were tabulated and statistically analysed with in EXCEL with ANOVA, and the Tukey-Kramer post-hoc analysis for statistical significance. The mean areas for each group were also expressed graphically, with errors represented as the standard error.

### 2.5.5 Retrograde Tracer Imaging Analysis

The analysis of the retrograde tracers, SPIO+SiO2+RuBpy+NH2 (n=3), SPIO+SiO2+C18 (n=4), SPIO+SiO2+RuBpy (n=4), and PBS control (n=3) was done

through image analysis with ImageJ at periods of 1 week, 2 weeks, and 3 weeks post-implantation. Not all groups were imaged at 3 weeks due to the availability of the MRI. Gradient Echo MR Images acquired on the 3 T Siemens TRIO were exported to a format analyzable with Image J using the Siemens Syngo Fast-View software and calibrated with mm markings. The spinal cord was identified in the MR images along with the site of the transection injury with tracer implantation. The identifiable hypointense region due to the iron contrast agent was measured as the distance of the hypointense region along the spinal cord between the rostral and caudal ends. Each distance was measured three times and averaged. The results of the distances were tabulated and statistically analysed with in EXCEL with ANOVA, and the Tukey post-hoc analysis for statistical significance, and the results were displayed graphically with error bars of the standard error. To determine if there were any changes in distance or movement of the band of contrast, the distances measured at the second and third week time points were subtracted from the distance at the first timepoint, and these results were expressed graphically with errors propagated from the standard error measurements from the distance measurements. ANOVA was done with EXCEL, analyzing differences within groups with time with $\alpha$=0.05.

To investigate the travel of the nanoparticle tracer with histology to corroborate the measures to that of the MRI, the histology was done in three ways for all groups. In the near range to the Surgifoam implantation site (within 5 mm rostrally), a 1 cm long section approximately 5 mm rostral to the Surgifoam was sectioned parasagittaly at 40 μm, and stained. The levels of the sections are shown in a diagram in Figure 2-2. To

investigate the long distance travel of the particles, axial sections 40 μm thick were cut at the upper cervical (C1-C2) level, and were imaged both for nanoparticle fluorescence and Prussian blue staining for iron. Furthermore, because it is possible that the particles were not seen in the axons in the cervical spinal cord, axial sections of the brain were cut at 40 μm thickness. Prussian Blue staining was done to test for the presence of iron nanoparticles, and fluorescence was also examined microscopically. Data was tabulated and statistically analyzed in EXCEL.

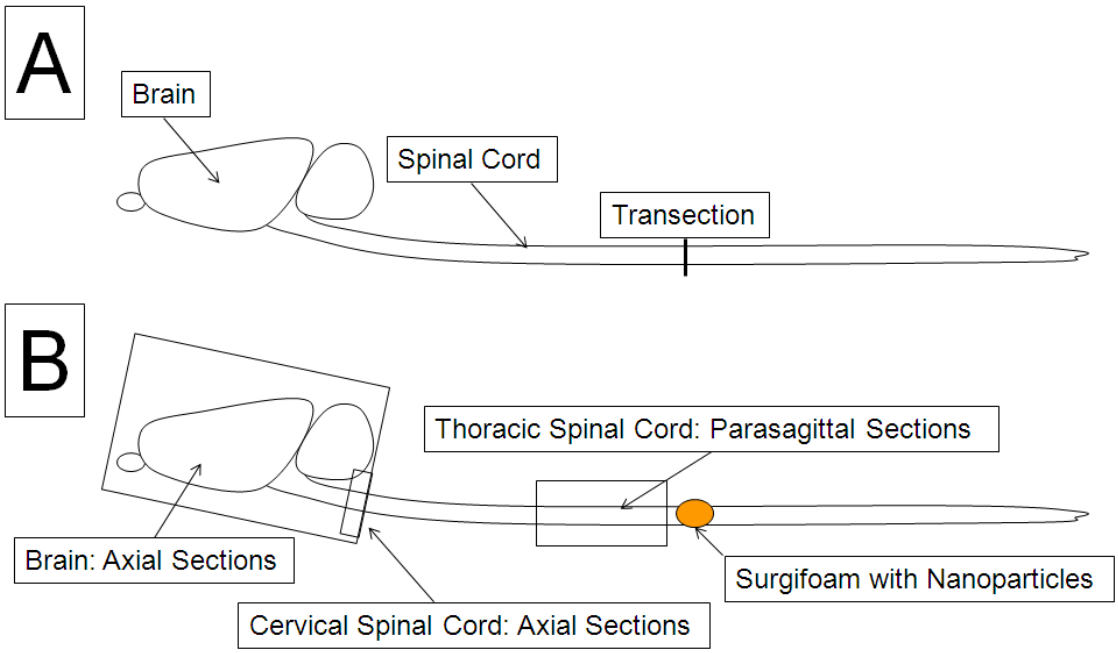


**Figure 2-2: Diagram of rat brain and spinal cords used in the retrograde axonal tracer experiments of tissue after perfusion and dissection.**
**A) shows the rat brain and spinal and the level of the transection of the in the spinal cord, and B) shows the implantation of the surgifoam pledget with nanoparticles and the level of the thoracic parasagittal sections, along with where the cervical axial and brain sections were made for histochemical analysis.**

### 2.5.6 Tissue Handling and Sectioning

At the experimental endpoints of animals, the rats were deeply anaesthetized with isofluorane, and with a thoracotomy were perfused with an intracardiac injection directly into the left ventricle of 500 mL of cold saline followed by 500 mL of 4% paraformaldehyde in phosphate buffered saline (PBS). The brain and spinal cord were harvested with the assistance of 9 mm serrated malleus nippers (Storz). The tissue was post-fixed at 4°C for 24 hours followed by 30% sucrose in PBS, and the tissue was only further processed once it had sunk to the bottom.

The tissue stored in the 30% sucrose solution was all processed for frozen sections. Tissues were mounted with Tissue-Tek Optimal Cutting Temperature (OCT) in plastic moulds, and were frozen in isopentane chilled to -40°C. The moulds were mounted in a cryostat (Leika), and the frozen tissue was serially sectioned directly onto SuperFrost (Fisher) glass microscope slides at a slice thickness of 40 μm. The slides were dried overnight on a slide warmer at 50°C, and stained immediately or stored at -80°C.

### 2.5.7 Prussian Blue Staining

Tissue sections were stained for iron using Prussian blue. Briefly, the frozen tissue sections were warmed to room temperature and were dipped in distilled water for 10 minutes for rehydration. The slides were then dipped for 5 minutes in a 5% potassium ferrocyanide solution in deionized water, followed by a 1:1 mixture of 5% potassium ferrocyanide: 5% hydrochloric acid for a period of 20-40 minutes. The slides were rinsed for 5 minutes in distilled water. Because of the fluorescence associated with nuclear fast

red counterstaining, when Prussian blue was combined with fluorescence, no further counterstaining was done, and the sections would proceed directly to the dehydration step. Otherwise, for counterstaining, nuclear fast red was used. The slides were dipped for a period of 5 minutes in a 0.1% nuclear fast red solution in 5% aluminum sulphate, and were rinsed with running tap water for 1 minute (until the solution cleared). Sections were dehydrated with 2 changes each for 5 minutes in 95% ethanol, 100% ethanol, and xylene (or Histoclear), and mounted with Permount (Fisher) and coverslipped.

### 2.5.8 Biotinylated Dextan Amine Histochemistry

Staining for BDA was done with 3,3'-Diaminobenzidine (DAB) using methods previously established by Veenman *et al*[48]. Tissue was stained with the biotinylated dextran amine kit (Invitrogen) in accordance with manufacturer's instructions.

### 2.5.9 Microscopic Imaging and Quantification

All bright field, fluorescence, and confocal microscopic imaging was done with a Nikon C1Eclipse inverted optical microscope.

## 2.6 *Ex vivo* Nanoparticle Studies

Spinal cords were isolated from the healthy spinal cord tissue extracted from three adult female Sprague Dawley rats 6 weeks in age. This procedure was developed for axon tracing in fixed tissue with other lipophilic dyes[80].The rats were fixed with 4% paraformaldehyde(PFA) through an intercardiac perfusion after first being perfused with 500 ml phosphate buffered saline. The brains and spinal cords were harvested and kept in 4% PFA overnight. The spinal cords were cut into sections of approximately 1 cm in

length and the rostral faces of the spinal cords were coated with the dried nanoparticle dyes. SPIO+$SiO_2$+RuBpy+C18 nanoparticles were investigated (n=3) with bare fluorescent SPIO+$SiO_2$+RuBpy as negative control (n=3) as well as the lipophilic tracer DiI as positive control (n=3). The rostral faces of the spinal cords were then coated with paraffin wax to prevent leakage of the dyes into the solution and the cords were incubated in 4% PFA at 37°C for 3 weeks. This type of study has been attempted previously with the use of agarose,[80] but wax was used as a substitute due to the availability of the materials.

Histological examination was done by serial cryo-sectioning the spinal cords 40 μm thick along the parasagittal axis. The sections were imaged directly for fluorescence with a Nikon fluorescence microscope, differentiating between autofluorescence and the dye fluorescence with the use of a long-pass UV filter, and red and green band pass filters. The images were taken in an automated process with a 4 x objective and stitched together. The distance from the spinal cord face where the particles were applied to the furthest continuous streak of the dye was measured in microns with the Nikon NS software. The results from the groups were tabulated in EXCEL, and statistical analysis was done in EXCEL with ANOVA, and the Tukey-Kramer post-hoc analysis for statistical significance.

# Chapter 3: Results

## 3.1 Nanoparticle characterization

The synthesized silica nanoparticles were characterized with infrared spectroscopy. The iron oxide core nanoparticles were purchased as prepared with the specifications that the particles did not have surfactant. The various functionalizations of the nanoparticles are shown schematically in Figure 3-1. The SPIO nanoparticles showed evidence of a band in the region of 3500 $cm^{-1}$, characteristic of hydroxyl stretching. With the addition of the silica functionalization on the surface of the particles, there was a peak and shoulder at 1050 $cm^{-1}$, indicative of Si-O stretching. A doublet of peaks at the 2800 $cm^{-1}$ range in the C18 functionalization of the nanoparticles is characteristic of a long carbon chain. In the case of the NH2 functionalization, there was an appearance of peaks in the range of 2800 $cm^{-1}$, and 1700 $cm^{-1,}$ characteristic of further functionalization on the surface of the silica nanoparticle. In the case of the BDA functionalization, there was a peak broadening of the 3500 $cm^{-1}$ peak, and the appearance of a peak at 2800 $cm^{-1}$. These indicated functionalization in addition to the bare SPIO+SiO2 nanoparticle.

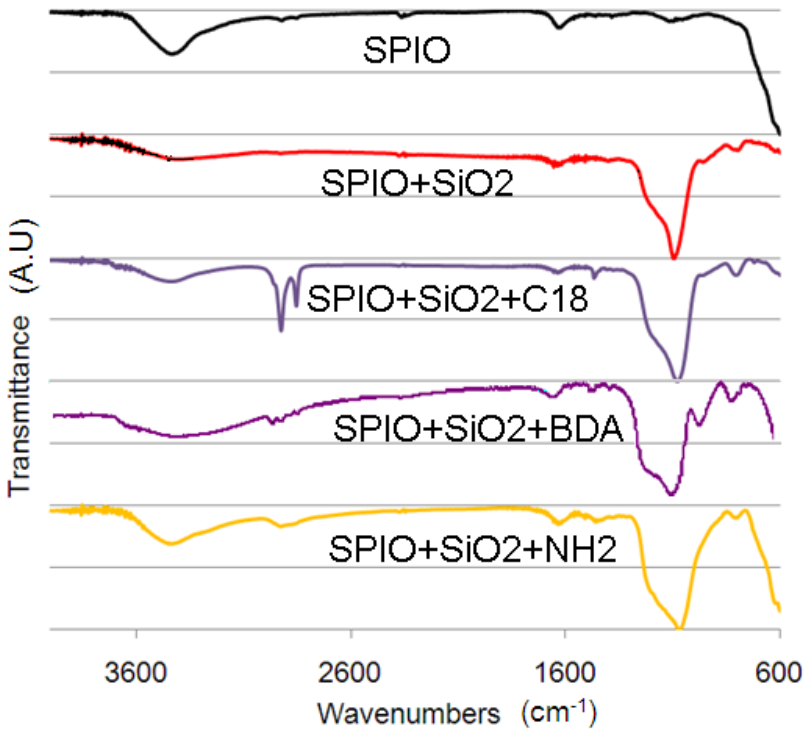


**Figure 3-1: Infrared spectroscopic characterization of the functionalized nanoparticles.**

The fluorescence spectroscopic characterization of the nanoparticles functionalized with the RuBpyRuBpy shell at a 460 nm excitation wavelength indicated a strong fluorescence emission peak at 610 nm. With the application of an external magnetic field, the fluorescence emission intensity of the SPIO+SiO2+RuBpy nanoparticles decreased. This was due to the precipitation of the nanoparticles in the magnetic field, and therefore the reduction in fluorescence intensity, indicating that the fluorescence functionality and magnetic functionality were unified on the same nanoparticle.

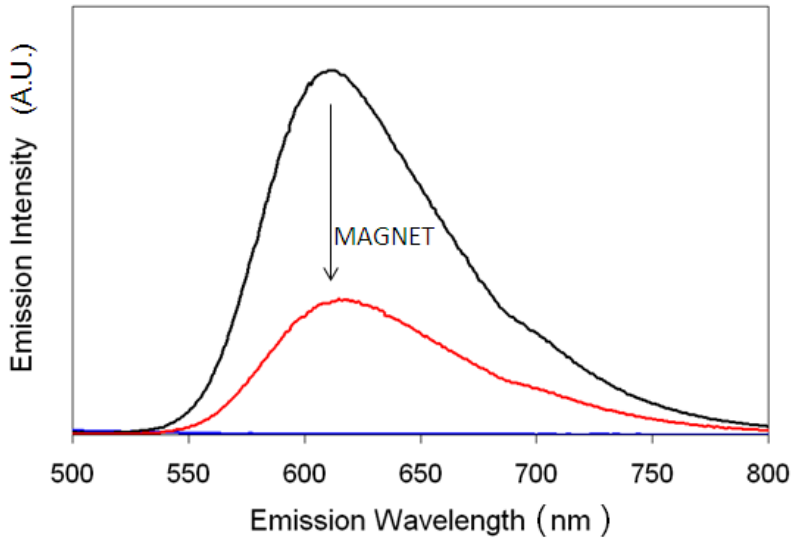


**Figure 3-2: Fluorescence spectroscopic characterization of SPIO+SiO2+RuBpy nanoparticles (black) compared to SPIO+SiO2 (blue) nanoparticles alone. With the application of an external magnetic field, there is a reduction of fluorescence intensity (red). Excitation at 460 nm.**

SEM characterization of SPIO nanoparticles with functionalization is shown in Figure 3-3. Nanoparticles with SPIO, SPIO+SiO2, SPIO+SiO2+RuBpy, SPIO+SiO2+RuBpy, and SPIO+SiO2+RuBpy+C18 are shown. Particles are smaller than 500 nm. Increased functionalization of the nanoparticles corresponded with increased particle size.

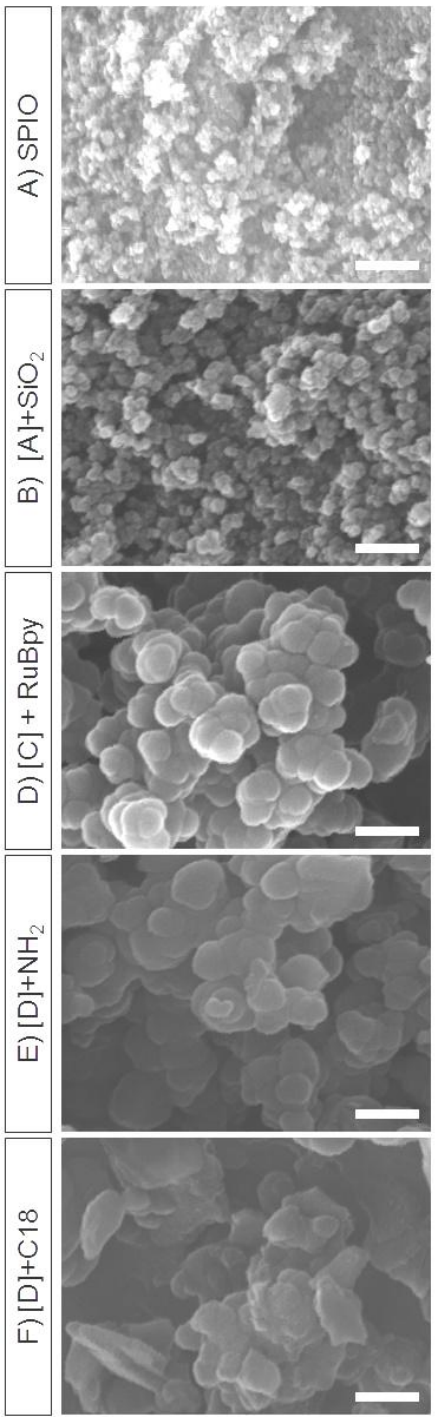


**Figure 3-3: Scanning electron microscopy images of SPIO nanoparticles. A) SPIO, B)SPIO+SiO2, C) SPIO+SiO2+RuBpy, D) SPIO+SiO2+RuBpy, E) SPIO+SiO2+RuBpy+C18. Scale bar 500 nm.**

Characterization of the nanoparticles was also done with magnetic resonance imaging to indentify the MRI contrast properties of the magnetic nanoparticles. On T2 weighted magnetic resonance imaging, increasing nanoparticle concentrations have decreased signal intensity compared to the water control. Images of the MRI characterization of the SPIO nanoparticles are shown in Figure 3-4.

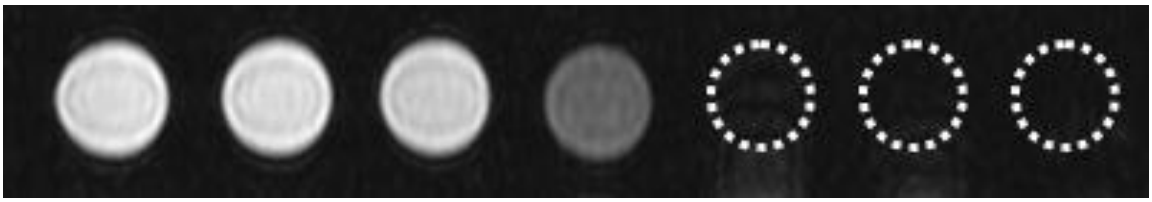

**Figure 3-4: T2 weighted MR image of varying concentration of SPIO nanoparticles. On the far left is water and from left to right are increasing concentrations of nanoparticles from $1x10^{-7}$ M, $1x10^{-6}$ M, $1x10^{-5}$ M, $1x10^{-4}$ M, $1x10^{-3}$ M, $1x10^{-2}$ M to $1x10^{-1}$ M SPIO. Because the contrast is so strong at higher concentrations, they cannot be distinguished on the image, and are highlighted in white.**

Further MRI characterizations were done to examine the contrast enhancement differences between ferric and ferrous iron at the same concentration. It was clear that at 1 mM of each of these aqueous solutions that the ferric iron was more hypointense. This is shown in Figure 3-5. This shows the relative strength of the oxidation state of iron on the contrast enhancement with MRI.

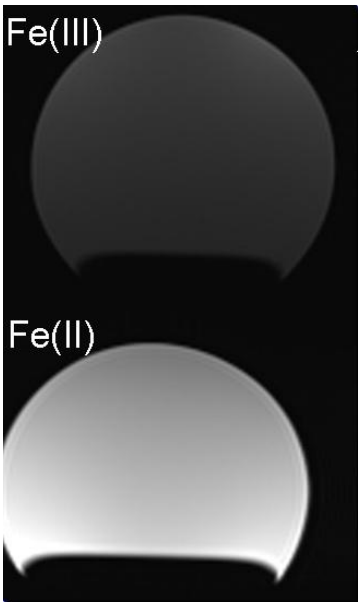


**Figure 3-5: T2 weighted MR image of 1 mM Ferric iron ($Fe^{3+}$) and 1mM Ferrous iron ($Fe^{2+}$) in solution.**
**Note that the ferric iron is much darker at the same concentration, and is a stronger paramagnetic contrast agent.**

## 3.2 *In vitro* Nanoparticle Studies

*In vitro* studies of NPC cultured for 7 days with nanoparticles were done. Fluorescence microscopy of the cells with Hoechst labelling and the nanoparticle RuBpy fluorescence with a UV-long pass filter (360 nm excitation and 400 nm long pass emission) are shown in Figure 3-6 for nanoparticles at 1 mM. The Hoechst labelling of the cells could be visualized by fluorescence microscopy in all groups. In the PBS, SPIO, SPIO+SiO2 groups, there was no fluorescence of the nanoparticles visualized with UV excitation. In the other groups, SPIO+SiO2+RuBpy, SPIO+SiO2+RuBpy+NH2, SPIO+SiO2+RuBpy+BDA, and SPIO+SiO2+RuBpy+C18 there was an orange fluorescence signal visualized with UV excitation of the nanoparticles associated with the

cell structures. To determine if the nanoparticles were inside the cell, or coated on the surface of the cell membrane, confocal microscopy was used.

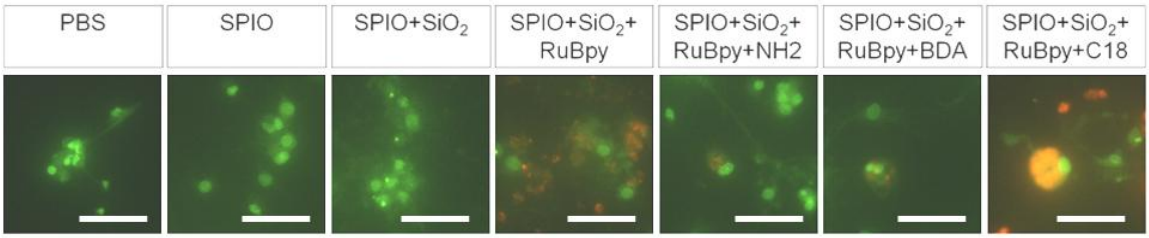


**Figure 3-6: Microscopic images 20x of Hoechst (green) and nanoparticles (orange) with NPC incubated with nanoparticles.**
**Orange-red fluorescence can be seen in the cells with nanoparticles made of SPIO+SiO2+RuBpy, SPIO+SiO2+RuBpy+NH2, SPIO+SiO2+RuBpy+BDA, and SPIO+SiO2+RuBpy+C18 at 1 mM nanoparticles. Scale bar of 50 µm. Hoechst is green due to the fluorescence seen with the long pass filter.**

Confocal microscopy was used to determine both the uptake and location of the nanoparticles cultured for 7 days with NPC. Optical sections were made at 10 μm slice thicknesses, and the images along with orthogonal projections are shown in Figure 3-7. These are representative images at 1mM for SPIO (n=3), SPIO+SiO2 (n=3), SPIO+SiO2+RuBpy (n=3), SPIO+SiO2+RuBpy+NH2 (n=3), SPIO+SiO2+RuBpy+BDA (n=3), SPIO+SiO2+RuBpy+C18 (n=3), and PBS alone (n=3). In the PBS, SPIO, and SPIO+SiO2 groups, no fluorescence signal was visualized. This is consistent with the lack of dye incorporation in the nanoparticles in these groups, indicating that any dye labeling was from the nanoparticles themselves. In the orthogonal projection of the nanoparticles with all functionalizations, the fluorescence from the nanoparticles was seen within the cells. At the 10 mM particle concentration, there was fluorescence from nanoparticles coating the plate that was not associated with cells, and there were also some particles which are seen on the outside of cells. This indicated that not 100% of the nanoparticles were taken up into the cells, and that there were excess particles which were not incorporated into cells. Fluorescence was excited with a 488 nm laser and detected at 615 nm. Cells were counted as positive for the uptake of nanoparticles if there was fluorescence from the nanoparticles detected within the cells as determined through examination of the three dimensional orthogonal representation. The cell boundaries were identified with the transmitted light image in three dimensions, and fluorescence was detected within the cellular borders. This was done to ensure that particles were in fact within the cells and not on exterior or on the surface of the cellular membrane. High nanoparticle concentrations did not have 100% uptake of nanoparticles.

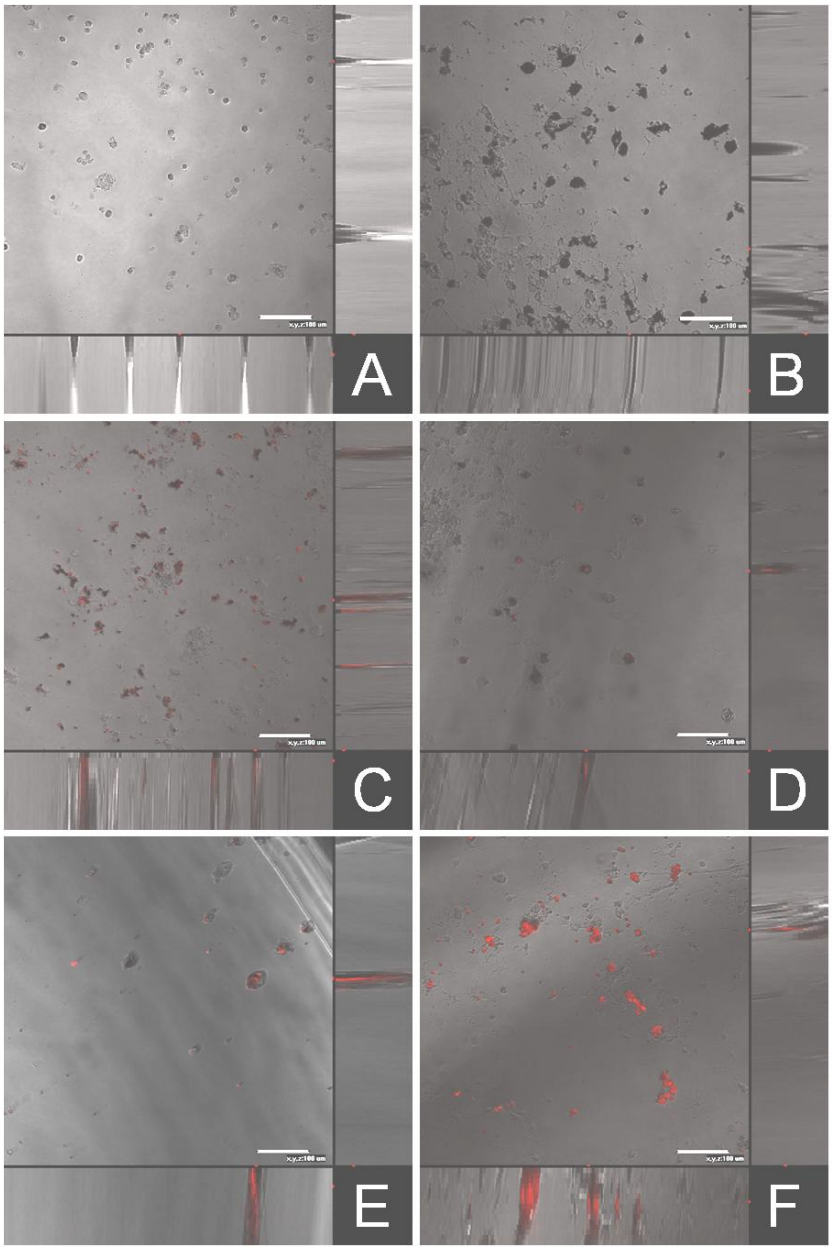


**Figure 3-7: Confocal microscopic images of NPC with nanoparticles.**
**Red signal indicates a fluorescent signal from the nanoparticles, and the transmitted light phase image was taken to identify the morphology of the cells. Scale bar of 100 µm. A) PBS, B) SPIO+SiO2, C) SPIO+SiO2+RuBpy, D) SPIO+SiO2+RuBpy+NH2, E) SPIO+SiO2+RuBpy+BDA, F) SPIO+SiO2+RuBpy+C18 at 1 mM with respect to iron. The orthogonal projection of the cells indicated that the particles were associated within the cell boundaries.**

Quantification of nanoparticle fluorescence in the cells was assessed with confocal microscopy at nanoparticle concentrations of 0.1 mM, 1 mM, and 10 mM. A a PBS control without nanoparticles was used as a control for cell viability and a control with 0.3% hydrogen peroxide was used as a control for cell death. These resuls are shown in Figure 3-8. None of the cells were positive for fluorescence in the SPIO, SPIO+SiO2, PBS, and $H_2O_2$ groups. This was due to the lack of nanoparticle labelling in these groups. There were statistically significant differences in the levels of cell labelling with nanoparticles at 1 mM with SPIO+SiO2+RuBpy and SPIO+SiO2+RuBpy+C18 nanoparticles ($p<0.05$, ANOVA, Tukey-Kramer Post-hoc). At 10 mM, all of the dye functionalized nanoparticles showed statistically significant differences in the level of cell uptake between control groups and those without dye ($p<0.05$, ANOVA, Tukey-Kramer Post-hoc).

In all groups of fluorescent nanoparticles, approximately 80-90% of cells were co-labelled with nanoparticles. Increasing nanoparticle concentrations have an effect on increasing the number of cells which were labelled with nanoparticles in all groups. The difference between the number of cells labelled with fluorescent nanoparticles at 0.1 mM and 1 mM, however, was not statistically significant. The fluorescence signal, both intensity and spatial labelling size, varied between individual cells.

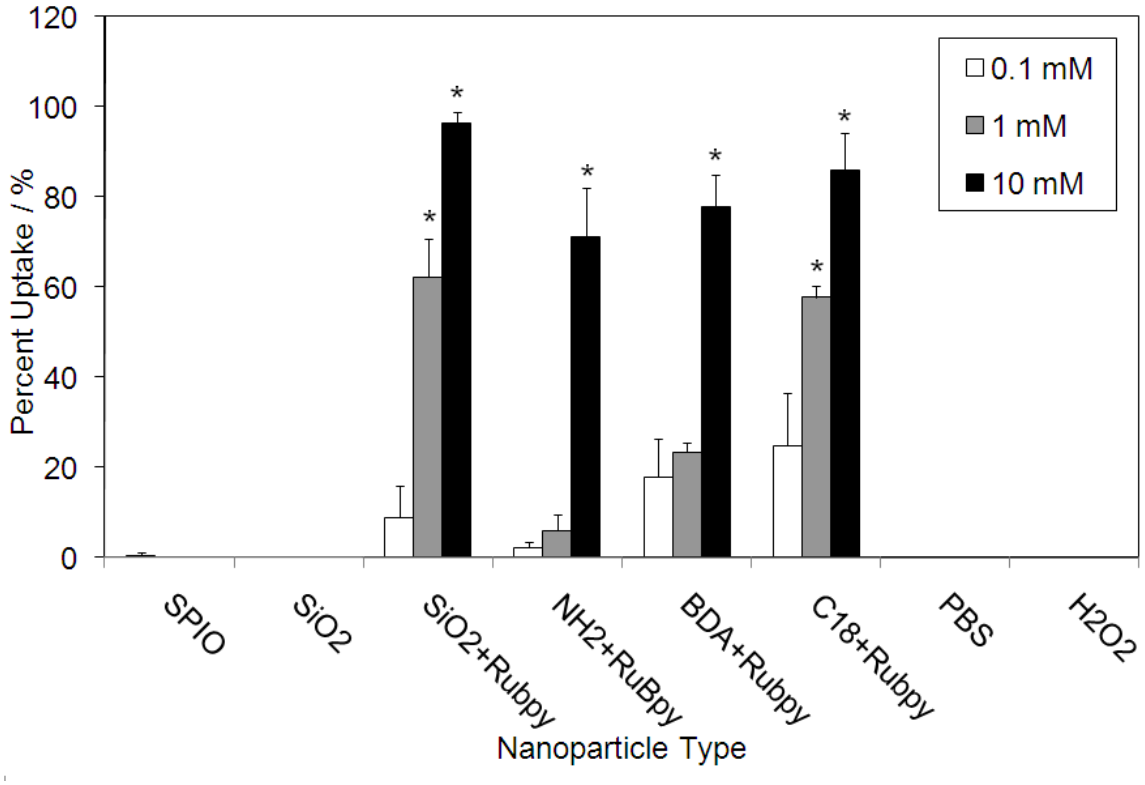


**Figure 3-8: Quantification of the cellular uptake of functionalized nanoparticles through confocal microscopy.**

**The percent of cells with the nanoparticle fluorescence signal present is shown as a function of different functional groups at 0.1 mM, 1 mM, and 10 mM iron. Fluorescence was found in cells incubated with SPIO+SiO2+RuBpy, SPIO+SiO2+RuBpy+NH2, SPIO+SiO2+RuBpy+BDA, and SPIO+SiO2+RuBpy+C18. (*) indicates statistically significant differences in the percent of labeled cells compared to the PBS control with ANOVA p>0.05 with Tukey post-hoc analysis.**

Shown in Figure 3-9 are representative images of the Prussian blue cellular labelling of NPC incubated with nanoparticles with various functional groups at 1 mM for 7 days. In the PBS control, there was no labelling for Prussian blue. With the various ranges of surface functionalizations of the SPIO particles, there were varying effects on

the cell labelling, and the number of cells containing Prussian blue staining were quantified.

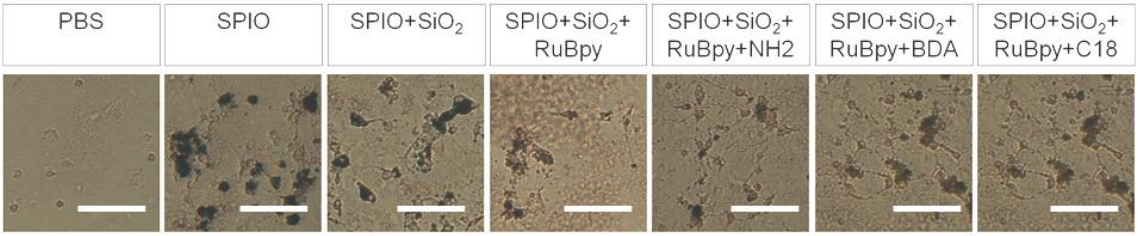


**Figure 3-9: Microscopic images of Prussian Blue stained NPC cells with nuclear fast red counterstain.**

**Prussian blue from the iron in the nanoparticles is shown blue. Prussian blue is detected in SPIO, SPIO+SiO2, SPIO+SiO2+RuBpy, SPIO+SiO2+RuBpy+NH2, SPIO+SiO2+RuBpy+BDA, and SPIO+SiO2+RuBpy+C18 at 1 mM nanoparticles. Scale bar = 100 µm.**

The quantification of Prussian blue labelling assessed the number of cells taking up the nanoparticles at 0.1 mM, 1 mM and 10 mM, SPIO (n=3), SPIO+SiO2 (n=3), SPIO+SiO2+RuBpy (n=3), SPIO+SiO2+RuBpy+NH2 (n=3), SPIO+SiO2+RuBpy+BDA (n=3), SPIO+SiO2+RuBpy+C18 (n=3), along with PBS (n=3) and $H_2O_2$ alone (n=3) as controls. Unlike with the confocal microscopic analysis, all the nanoparticle groups, including SPIO and SPIO+SiO2 were labelled. This was due to the fact that Prussian blue detects iron, rather than the nanoparticle fluorescence signal. The concentration of iron in each cell was not quantified. In quantifying cell numbers in contrast to both the PBS and $H_2O_2$ controls, as shown in Figure 3-10, there was uptake of nanoparticles and cell labelling at all concentrations. Compared to the control, there was a statistically significant labelling of cells with Prussian blue for all functional groups at 10 mM, and approximately 90% of cells were labelled. At 1 mM nanoparticles, approximately 60% of

cells were labelled, and this difference was statistically significant to the control in the case of all groups with the exception of the SPIO+SiO2+RuBpy+C18 group. At 0.1 mM, only SPIO and SPIO+SiO2 cell counts were statistically significant, at levels in the range of 50%. Differences within the same nanoparticle functionalizations at different concentrations existed between 0.1 mM and 10 mM groups and also between the 1mM and 10mM groups and were statistically significant, and none were significant between 0.1 mM and 1 mM ($p>0.05$, ANOVA, Tukey-Kramer Post-hoc).

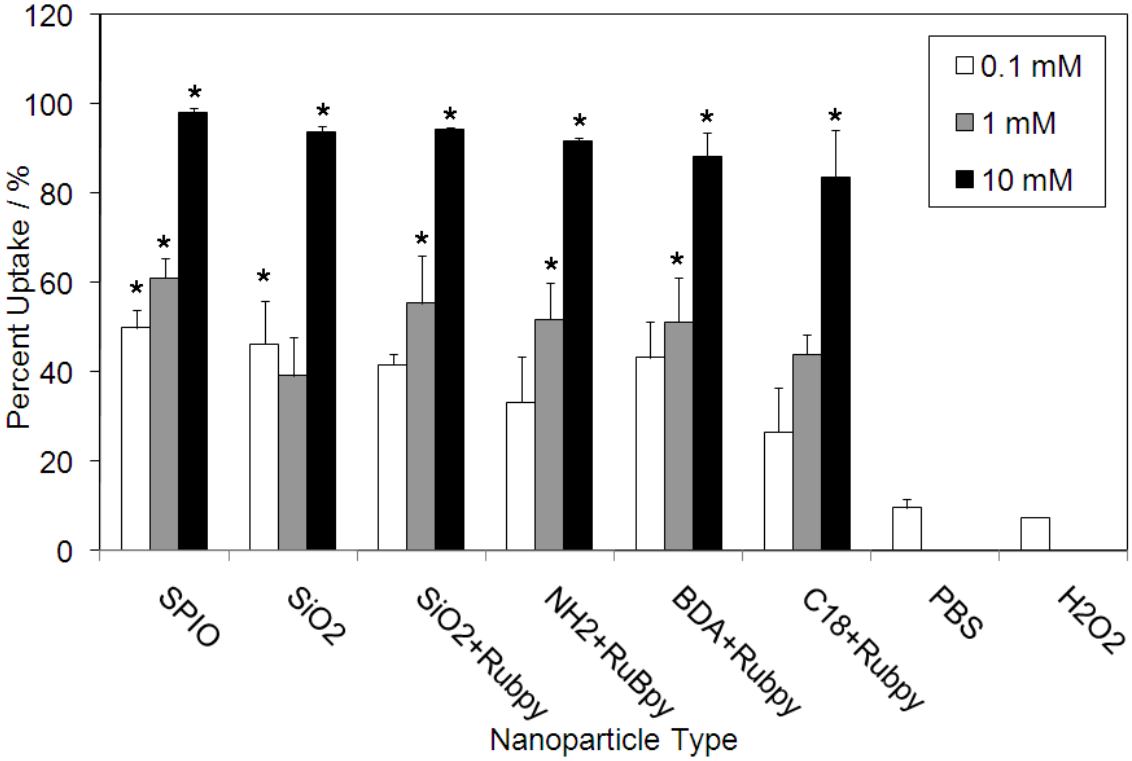


**Figure 3-10: Quantification of the cellular uptake of functionalized nanoparticles through Prussian blue staining and microscopy.**

**The percent of cells with Prussian blue from nanoparticles is shown as a function of different functional groups at 0.1 mM, 1 mM, and 10 mM iron. Prussian blue was found in cells incubated with SPIO, SPIO+ SiO2, SPIO+SiO2+RuBpy, SPIO+SiO2+RuBpy+NH2, SPIO+SiO2+RuBpy+BDA, and SPIO+SiO2+RuBpy+C18. (*) indicates statistically significant differences in the percent of labeled cells compared to the PBS control with ANOVA $p<0.05$ with Tukey post-hoc analysis.**

Assessment of cellular toxicity was done using a Trypan blue cellular exclusion assay for concentrations of nanoparticles of 0.1 mM, 1 mM, and 10 mM for SPIO (n=3), SPIO+SiO2 (n=3), SPIO+SiO2+RuBpy (n=3), SPIO+SiO2+RuBpy+NH2 (n=3), SPIO+SiO2+RuBpy+BDA (n=3), SPIO+SiO2+RuBpy+C18 (n=3), and PBS alone (n=3)

incubated for 7 days. Also included were SPIO+SiO2+No_RuBpy (n=3), SPIO+SiO2+No_RuBpy+NH2 (n=3), SPIO+SiO2+No_RuBpy+BDA (n=3), SPIO+SiO2+No_RuBpy+C18 (n=3), where "No_RuBpy" indicated the exclusion of the RuBpy dye from the multifunctional nanoparticle to assess the effects of dye on cellular toxicity. There was a statistically significant difference between PBS and $H_2O_2$ levels of trypan blue exclusion. This indicates $H_2O_2$ was an effective positive control for cellular toxicity. These results are displayed graphically in Figure 3-11. The levels of trypan blue labelling between the PBS control and the $H_2O_2$ positive control for toxicity revealed a statistically significant difference, indicating that the levels of trypan blue labelling for $H_2O_2$ was a good measure for toxicity. There was a non-statistically significant trend of increasing toxicity with increasing nanoparticle concentration within groups, with one exception where the difference was statistically significant for SPIO+SiO2+No_RuBpy+NH2. At all nanoparticle concentrations, there was no statistically significant difference between the trypan blue labelling of the various nanoparticle concentrations and the PBS controls, indicating no difference with PBS. The only exception was SPIO+SiO2+No_RuBpy+NH2 at 10 mM, where there was a statistically significant difference between PBS and its value at 10 mM, while there was no statistically significant difference at this concentration to $H_2O_2$.

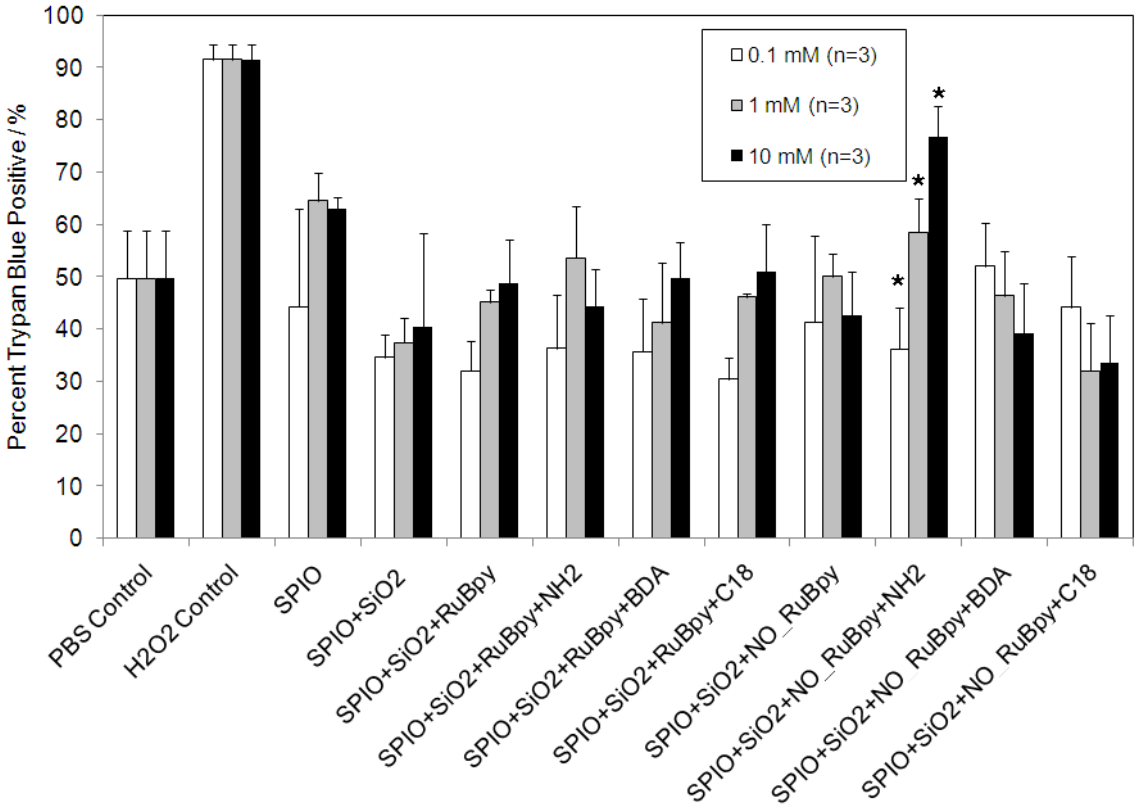


**Figure 3-11: Quantification of Trypan blue cellular exclusion assay for toxicity of NPC incubated with nanoparticles for 7 days.**

**Shown are the ratio of the number of cells labeled with Trypan blue compared to total cell counts as a function of nanoparticle functionalization at 0.1 mM, 1 mM, and 10 mM. No statistically significant differences exist between nanoparticles and PBS control, ANOVA $p<0.05$. (*) indicates statistically significant differences in cell death between concentrations of the same nanoparticle functionalization.**

TUNEL staining was done as another measure of toxicity of the nanoparticles at 0.1, 1 and 10 mM compared to PBS and $H_2O_2$ controls. In contrast with the trypan blue measurements, the groups used were nanoparticles with the exclusion of the RuBpy dye due to the fluorescence overlap of the dye with the TUNEL staining. SPIO (n=3), SPIO+SiO2 (n=3), SPIO+SiO2+NO_RuBpy (n=3), SPIO+SiO2+No_RuBpy+NH2 (n=3), SPIO+SiO2+No_RuBpy+BDA (n=3), SPIO+SiO2+No_RuBpy+C18 (n=3), where "No_RuBpy" indicated the exclusion of the dye. In this case, there did not exist a statistically significant difference in TUNEL staining between the PBS and $H_2O_2$ controls due to high PBS TUNEL levels; however, the TUNEL staining of $H_2O_2$ was at an average of 95%. ANOVA testing indicated that there was a statistically significant difference between TUNEL levels of $H_2O_2$ control and all nanoparticle groups at 0.1 mM and 1 mM with the exception of one group of SPIO+SiO2+No_RuBpy+BDA at 0.1 mM. At 10 mM, there was no statistically significant difference between the nanoparticle groups and the $H_2O_2$ control. *In vivo* testing of the nanoparticles was done at the levels of 10 mM to have a sufficient amount for contrast enhancement and also be able to test axonal transport. At this level, cell uptake was maximal from the previous results.

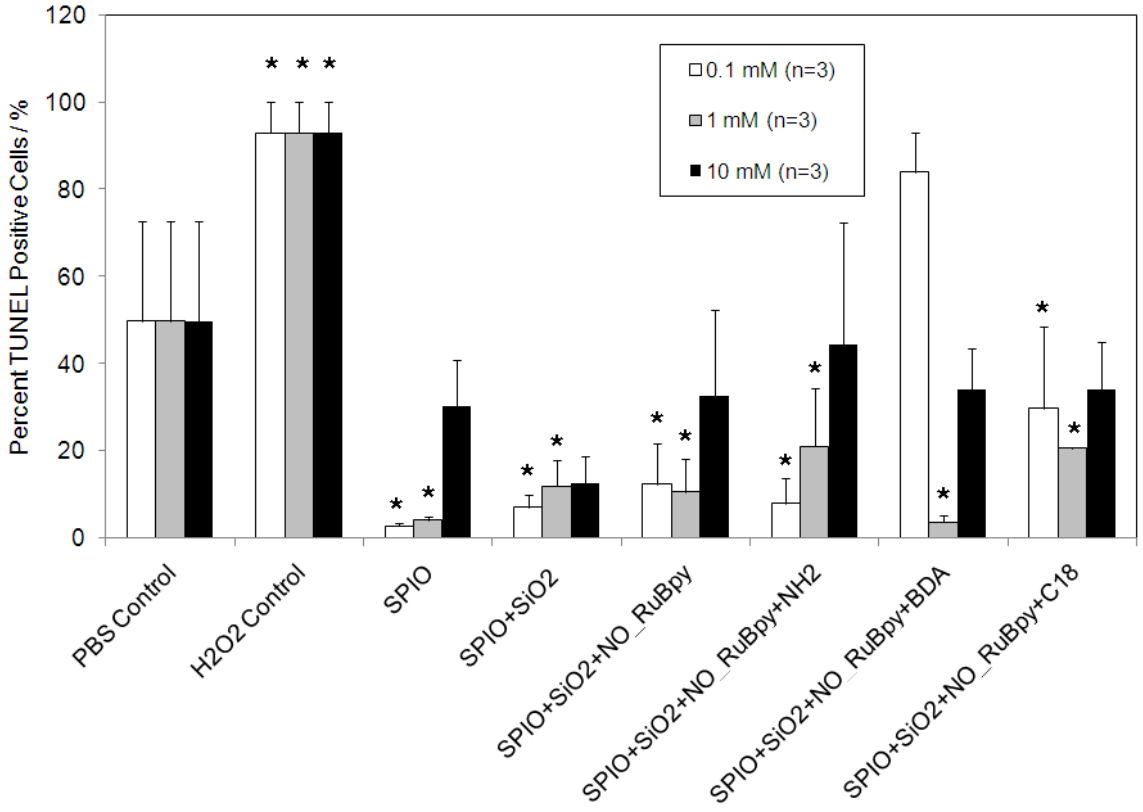


**Figure 3-12: Quantification of TUNEL assay for toxicity of NPC incubated with nanoparticles for 7 days.**

**Shown are the ratio of the number of cells labeled with TUNEL compared to total cell counts as a function of nanoparticle functionalization at 0.1 mM, 1 mM, and 10 mM. Statistically significant differences were not present between nanoparticles and PBS control, ANOVA $p<0.05$. (*) indicates statistically significant differences in TUNEL compared to the $H_2O_2$ toxicity control.**

## 3.3 *In vivo* Nanoparticle Studies

### 3.3.1 Anterograde Axonal Nanoparticle Tracers

Gradient echo MR images from animals receiving nanoparticle injections were obtained for rats receiving sensorimotor cortex injections of 1 % BDA (n=4) and 10 mM SPIO+SiO2+RuBpy+BDA (n=4), and representative axial and parasagittal images are

shown in Figure 3-13 at 1 day and 22 days post-injection. Serial images were acquired both in the parasagittal and axial planes for the rat brain, and the images with the signal hypointensity due to iron were identified. It was clear that on both parasagittal and axial sections of the rat brain that the contrast achieved with the nanoparticles was identifiable and larger in size than was the case in the rats receiving BDA injection alone.

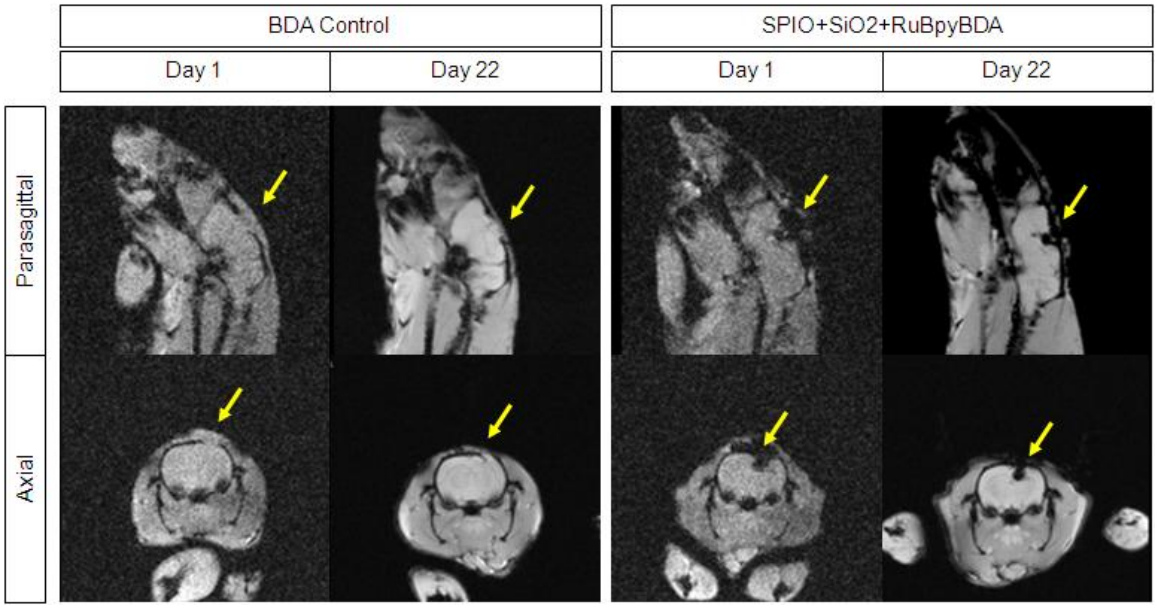


**Figure 3-13: Representative parasagittal and Axial gradient echo images of rat brains injected with 1% BDA and 10 mM SPIO+SiO2+RuBpy+BDA nanoparticles at 1 day post-injection and 22 days post injection.**

**The injection site can be visualized with MRI and is indicated with a yellow arrow. Note the large area of the hypointense contrast region from the SPIO particles in the +SiO2+RuBpy+BDA groups.**

Quantification of the area of the injection site for axial and parasagittal images was tabulated and expressed graphically in Figure 3-14. Contrasting the area of the injection at both day 1 and 22 post injection, there was a statistically significant difference between the injection of BDA (n=4) and SPIO+SiO2+RuBpy+BDA (n=4)

(ANOVA $p<0.05$, Tukey post-hoc analysis). In both cases of the SPIO+SiO2+RuBpy+BDA and BDA control, there was no statistically significant difference in the areas measured between the first and 22nd days which would be hypothesized to occur should the SPIO+SiO2+RuBpy+BDA function as an axon tracer.

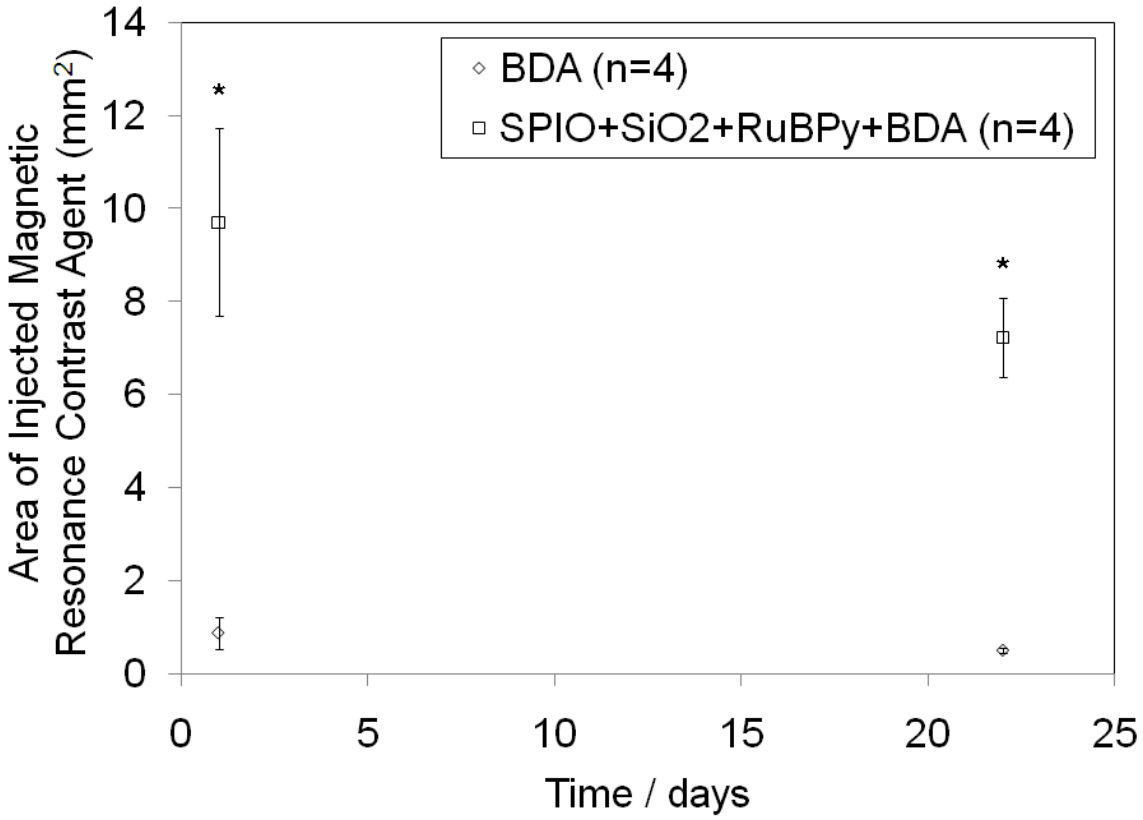


**Figure 3-14: Quantification of areas of decreased signal intensity in 1% BDA (n=4) and SPIO+SiO2+RuBpy+BDA (n=4) at day 1 and 22 post brain injection.**
**There is a non-statistically significant difference between the first and 22nd day in both the BDA and BDA+SiO2+RuBpy+BDA (ANOVA p=0.4) groups. The difference between BDA and BDA+SiO2+RuBpy+BDA measurements at both timepoints is statistically significant (ANOVA p>0.05, Tukey Post-hoc analysis)**

Histological analysis was done on the brains of the animals injected with the anterograde tracers for Prussian blue. A low power, representative merged image of the

entire rat brain at the level of the injection site identified is shown in Figure 3-15 for a SPIO+SiO2+RuBpy+BDA rat. The injection site is visible in the right hand side of the brain and extends down approximately 1 mm. Anatomical references are indicated to demonstrate the location of the injection site in the sensory-motor cortex of the rat brain. Further histological analysis was done examining the animals of different groups at the level of the injection site, and the window of where this is in relation to major anatomical structures in the brain is shown in Figure 3-15. Focal brain edema at the site on injection and craniotomy was visible at the sight of injection.

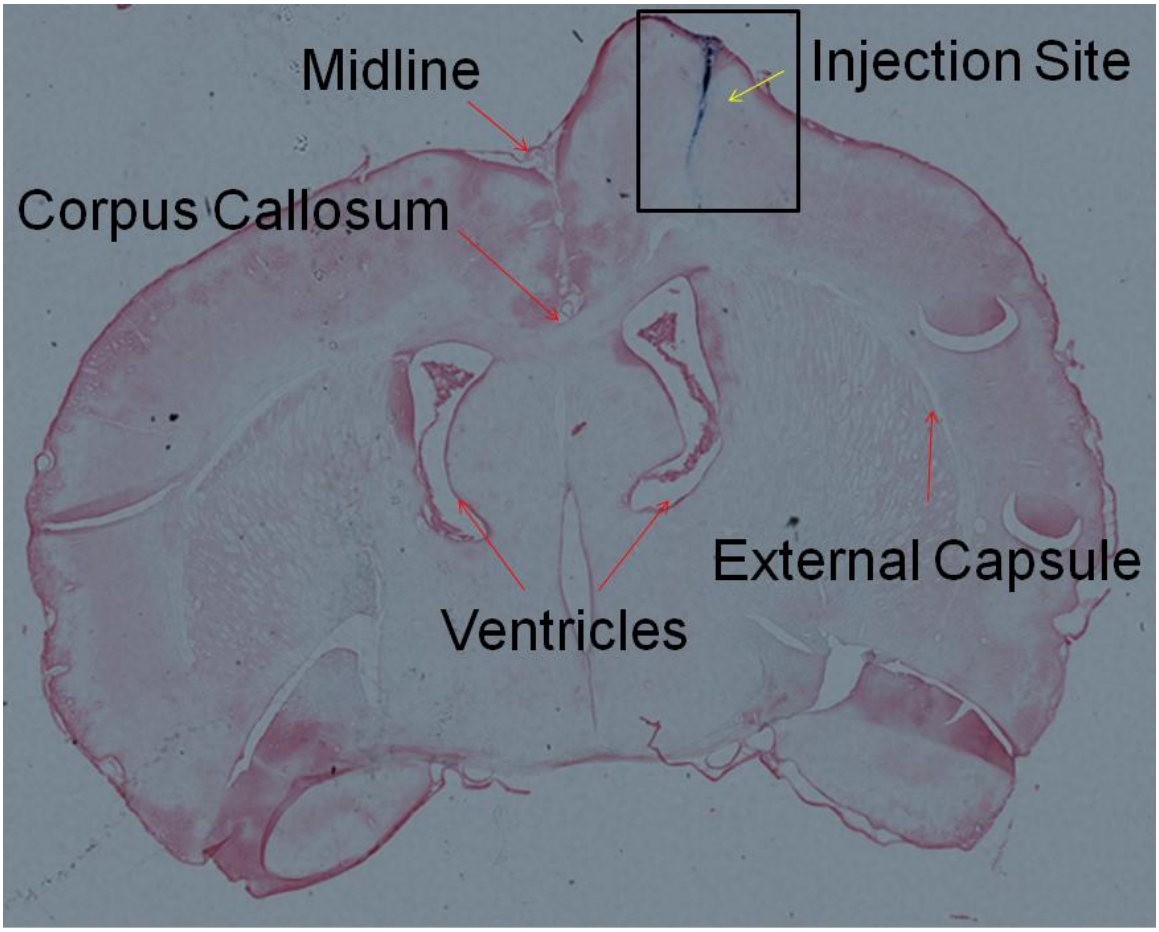


**Figure 3-15: Representative histological section of an entire axial section of rat brain sectioned at 40 µm injected with 10 mM SPIO+SiO2+RuBpy+BDA nanoparticles at 23 days post injection.**
**Images with a 4x objective were stitched together. The injection site labeled with Prussian blue is indicated with a yellow arrow. The box indicates the region of interest photographed for comparison between groups.**

Prussian blue staining was done for the anterograde tracer injection groups at the level of the site of the injection in the brain. Representative images for both groups are shown in Figure 3-16. Quantification of the depth of injection, area of the Prussian blue labeling and the optical absorbance of the injection are shown graphically in Figure 3-17, Figure 3-18, and Figure 3-19 respectively. In all cases, there was no statistically

significant difference in the injection depth, area, or optical absorbance with ANOVA $p>0.05$. Prussian blue staining was done in the hindbrain examining the pyramidal tracts and in the high cervical level of the spinal cord to assess for staining in the corticospinal tract in both the BDA (n=4) and SPIO+SiO2+RuBpy+BDA (n=4) groups. No Prussian blue staining was observed at either of these locations in the brain tissue in both groups indicating that the cortical spinal tract was not labeled in the hind brain pyramidal tracts and in the high cervical level of the spinal cord.

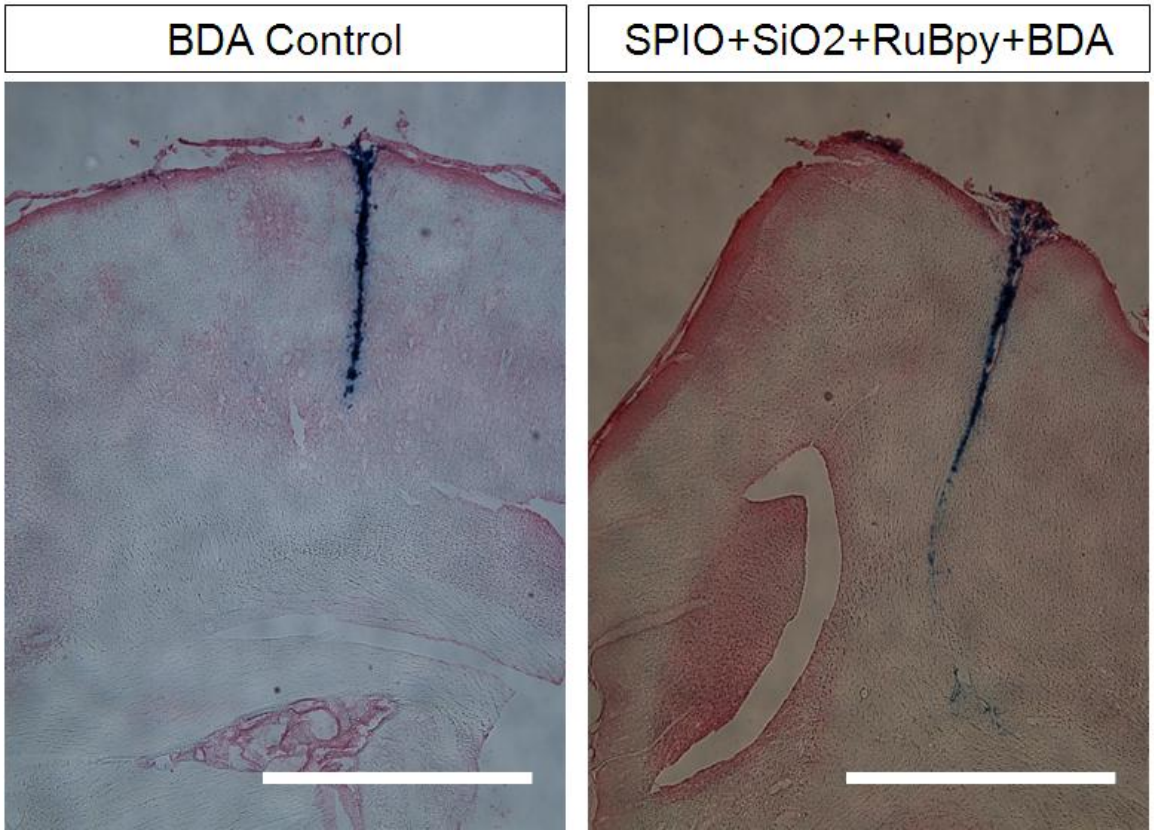


**Figure 3-16: Representative histological images of axial sections of rat brain sectioned at 40 µm injected with 1% BDA and 10 mM SPIO+SiO2+RuBpy+BDA nanoparticles at 23 days post injection.**

**The injection site labeled with Prussian blue is visualized in the top right corner in both cases. Scale bar of 1 mm.**

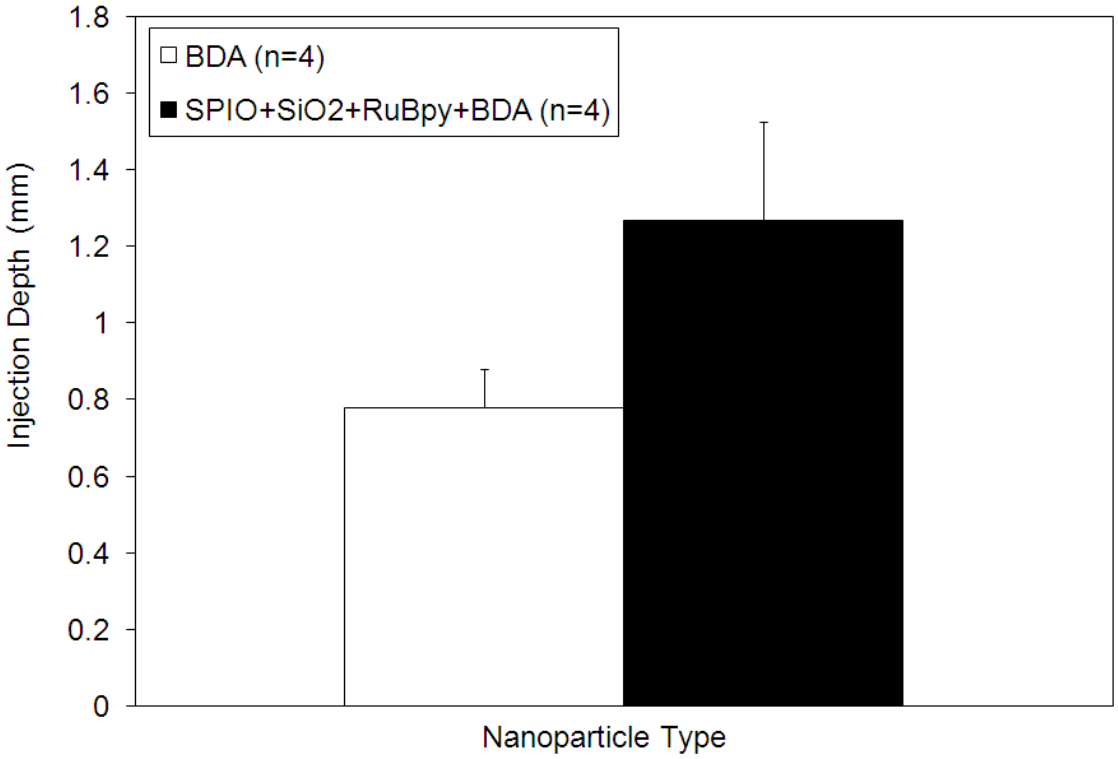


**Figure 3-17: Quantification of injection depth in histological sections of rat brains injected with 1% BDA (n=4) and 10 mM SPIO+SiO2+RuBpy+BDA (n=4) sacrificed 23 days post-injection.**

**There is no statistically significant difference in injection depth. ANOVA $p>0.05$.**

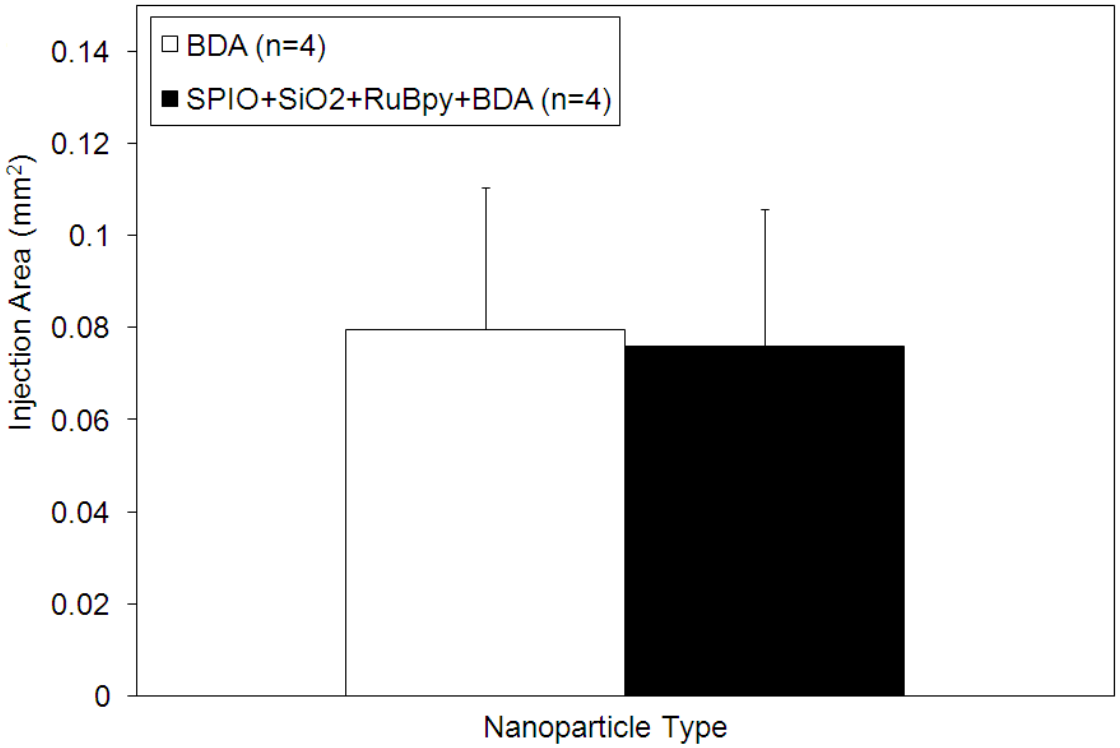


**Figure 3-18: Quantification of injection area in histological sections of rat brains injected with 1% BDA (n=4) and 10 mM SPIO+SiO2+RuBpy+BDA (n=4) sacrificed 23 days post-injection measured with Prussian blue.**

**There is no statistically significant difference in injection area. ANOVA $p>0.05$.**

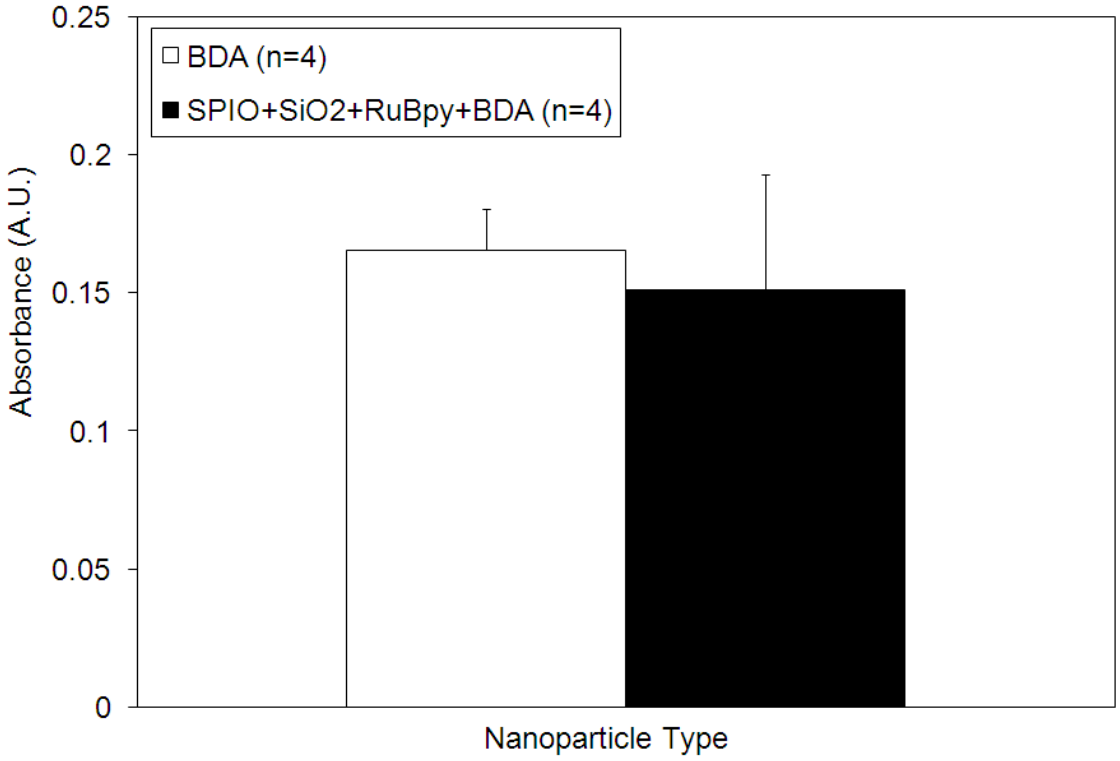


**Figure 3-19: Quantification of injection optical absorbance in the injection area in histological sections of rat brains injected with 1% BDA (n=4) and 10 mM SPIO+SiO2+RuBpy+BDA (n=4) sacrificed 23 days post-injection measured with Prussian blue.**
**There is no statistically significant difference in optical absorbance in the injection area. ANOVA p>0.05.**

BDA staining was done with Avidin-HRP and DAB to examine for neuronal labeling for the anterograde tracer experiments with BDA 1% (n=4) and SPIO+SiO2+RuBpy+BDA (n=4). Representative images of the BDA staining are shown in Figure 3-20. In the BDA 1% group, the labeling of cells with processes, characteristic of neurons can be seen; however, the form of the labeling with the SPIO+SiO2+RuBpy+BDA does not show the same characteristic staining. There were no distinct cells with the same appearance as the BDA alone. Staining was in the same form

of the Prussian blue staining in the above figure. BDA staining was done at the level of the hindbrain examining for the pyramidal tracts and in the upper cervical spinal cord examining for staining in the corticospinal tract; however, no staining was observed.

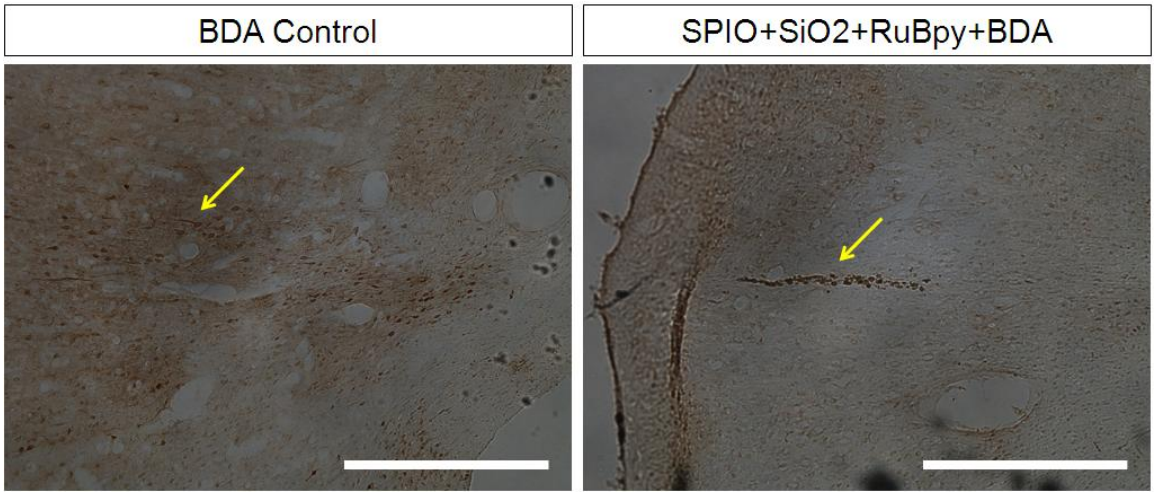


**Figure 3-20: BDA-Avidin HRP-DAB staining of rat brains receiving anterograde axonal tracer injections in the sensory-motor cortex.**
**Cells with processes are labeled with the BDA alone group (n=4), but are not in the SPIO+SiO2+RuBpy+BDA group (n=4).Yellow arrows indicate cell staining for DAB. Scale bar=1 mm.**

### 3.3.2 Retrograde Axonal Nanoparticle Tracing

Representative gradient echo magnetic resonance images of the spinal cords are shown at multiple weekly timepoints after the incorporation of the retrograde axonal tracer in the spinal cord for the groups PBS control (n=3), SPIO+SiO2+RuBpy (n=4), SPIO+SiO2+RuBpy+NH2 (n=3), and SPIO+SiO2+RuBpy+C18 (n=3) and are shown in Figure 3-21.

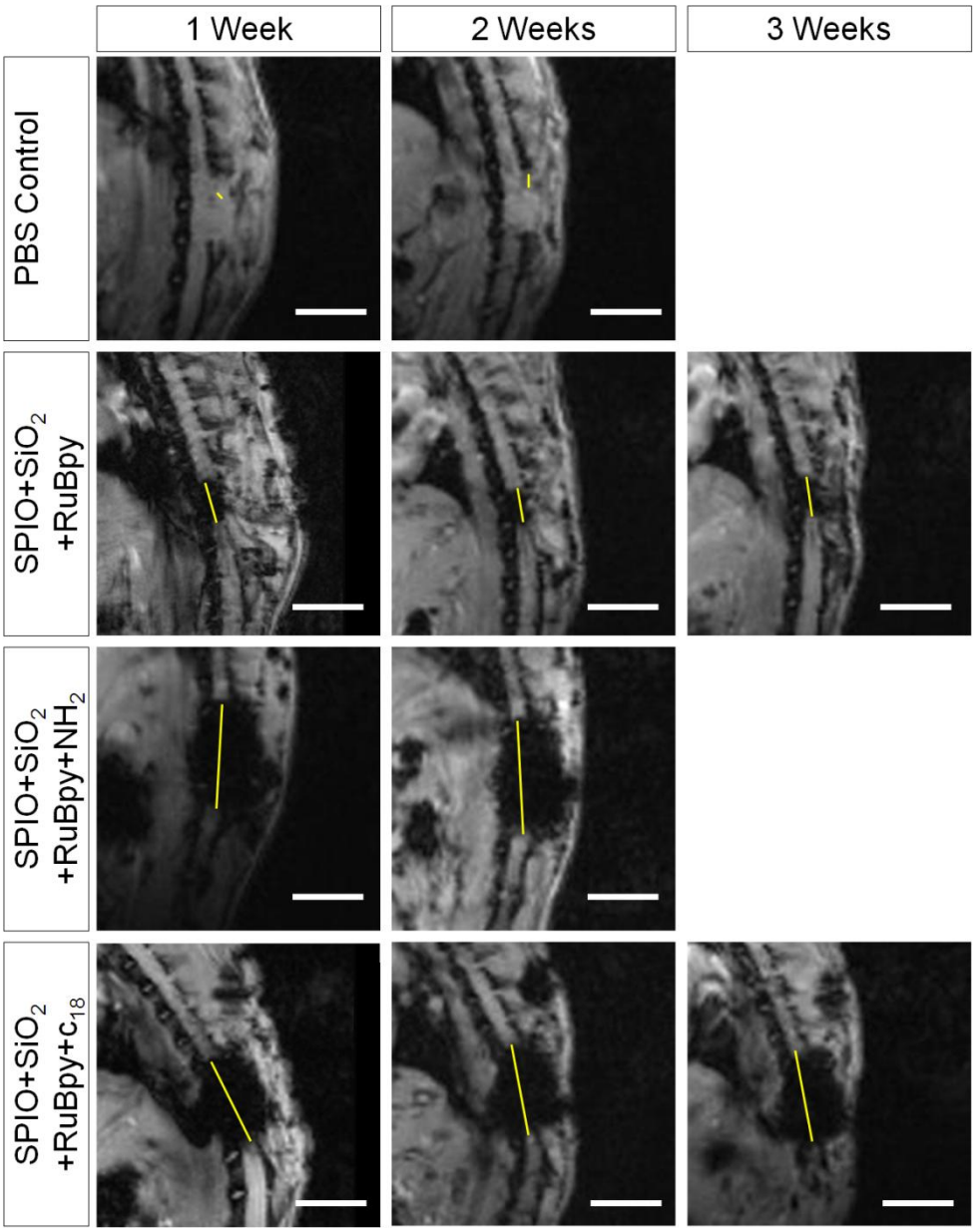


**Figure 3-21: Representative T1 weighted MR images of transected Sprague Dawley rat spinal cords.**

**Cord contained implants of Surgifoam pledgets loaded with 40 µL of PBS control, SPIO+RuBpy+$SiO_2$ nanoparticles, SPIO+$SiO_2$+RuBpy+$NH_2$ nanoparticles, and SPIO+SiO2+RuBpy+$C_{18}$ nanoparticles. at 1 week, 2 weeks, and 3 weeks post-implantation for SPIO+$SiO_2$+RuBpy and SPIO+$SiO_2$+RuBpy+$NH_2$ nanoparticles. Yellow lines indicate the distances of MRI contrast area measured. Scale bar=1 cm.**

Quantification of the change in distance of the decreased signal intensity within the region of the transacted spinal cord in the MR images was done over the time points for each of the groups. The graphical representation of the distance changes compared to the first week of MRI is shown in Figure 3-22. In the control group, there was no contrast which completely transected the cord at either the first or second weeks'. The large standard errors reflect the large variability in the measurements of length; however, no trend was observed in individual subjects. In the nanoparticle groups, there are no statistically significant differences with respect to the changes in the length of the decreased signal intensity along the spinal cord. In the SPIO+SiO2+RuBpy+C18 (n=3) group, there was an initial, non significant decrease in length followed by a non-significant increase in length. There was a non-significant decrease in length in the SPIO+SiO2+RuBpy (n=3) group measured with MRI. Quantification of the difference between the length values of all the nanoparticle groups compared to the PBS control indicated a statistically significant difference in length tested with ANOVA with Tukey-Kramer Post-hoc analysis $p<0.05$.

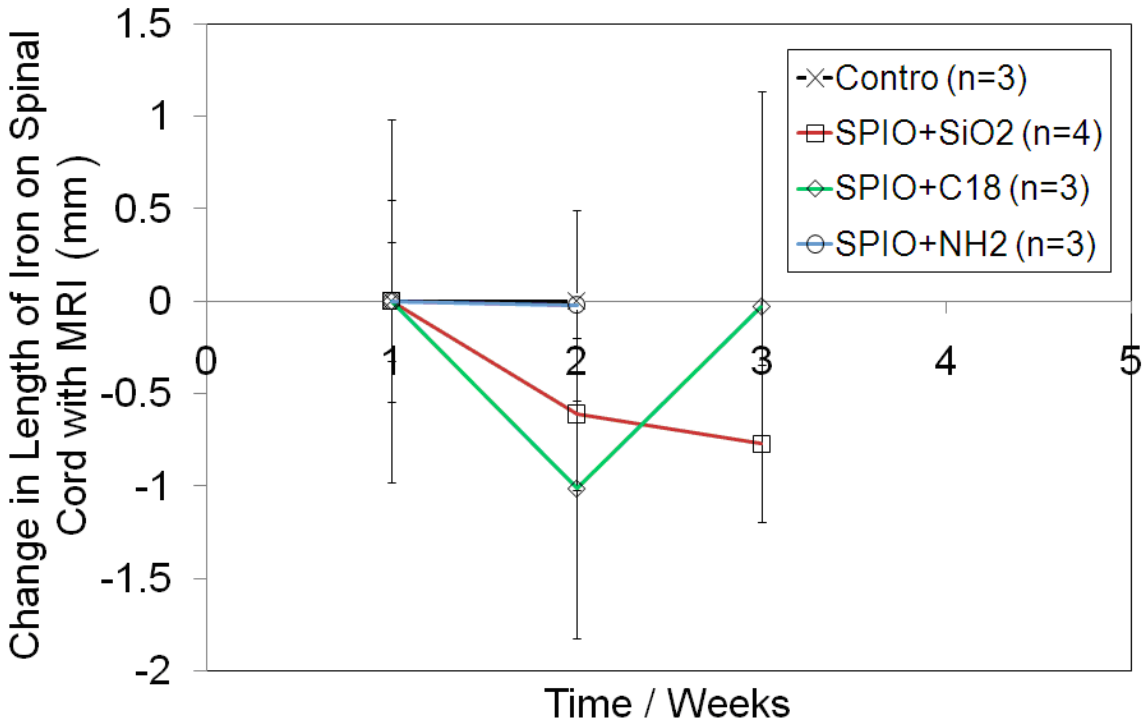


**Figure 3-22: Quantification of the change in the decreased signal intensity representing the nanoparticles in the spinal cord from the first week of T1 MRI measurements. Transected Sprague Dawley rat spinal cords implanted with Surgifoam pledgets loaded with 40 µL of PBS control (n=3), SPIO+$SiO_2$(RuBpy) nanoparticles (n=4), SPIO+$SiO_2$+$NH_2$(RuBpy) nanoparticles (n=3), and SPIO+SiO2+$C_{18}$(RuBpy) nanoparticles (n=3) were measured at weekly intervals. Quantification is of distance of the decreased signal intensity between the rostral and caudal ends of spinal cord. There is no statistically significant change in distance between any groups (p=0.51 ANOVA) or within groups at the different timepoints. Standard error is shown.**

Results of the histological examination of the fluorescence from the nanoparticles in the brain, cervical spinal cord and thoracic spinal cord are shown schematically in Figure 2-2. The cervical spinal cord sections at 40 µm indicated no nanoparticle fluorescence in the UV-bandpass filter. Low power microscopic sections of the

fluorescence images of the cervical spinal cord are shown in Figure 3-23. Any fluorescence from the nanoparticle RuBpy dye would appear orange on the images.

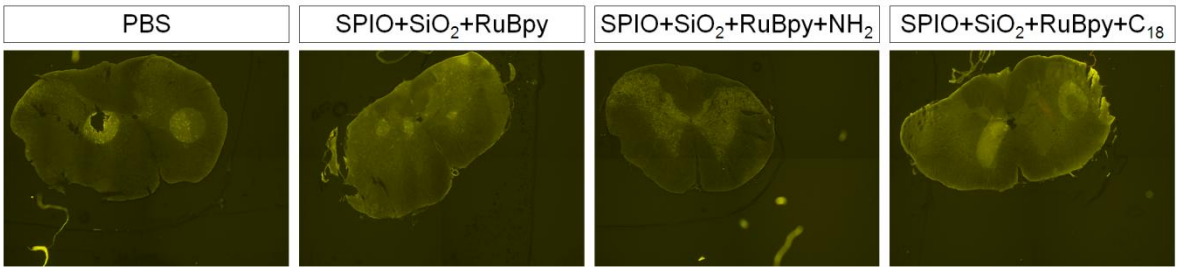


**Figure 3-23: Representative histological sections of axial cervical sections of rat spinal cord sectioned at 40 µm.**
**Fluorescence images were taken with the Fluoro-gold long pass filter, and fluorescence of the nanoparticles would be seen as orange. No nanoparticle fluorescence was found in the cervical axial sections.**

Fluorescence was examined in the brains of the rats receiving the retrograde nanoparticle tracers. There was no Prussian blue labeling of the nanoparticles in the brain, and sample sections at the level of the sensory-motor cortex are shown in Figure 3-24. Prussian blue staining was also done at the level of the hindbrain to assess for staining of the pyramidal tracts; however, no staining was observed. This suggests that retrograde transport of the nanoparticles to the pyramidal tract region of the hindbrain did not occur. It was concluded that retrograde transport of the nanoparticles from the spinal cord to the brain did not occur.

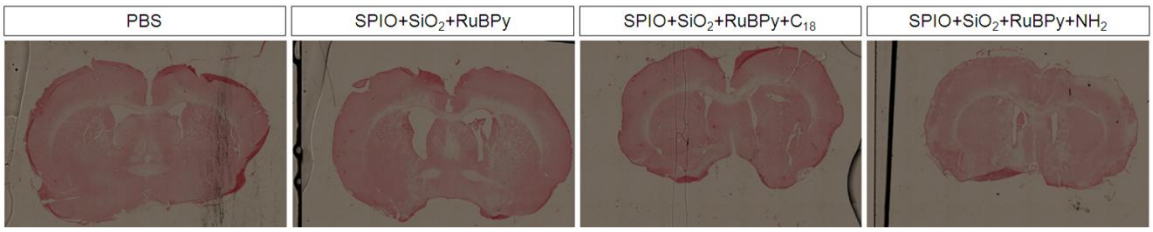


**Figure 3-24: Representative Prussian Blue/Nuclear fast red stained brain sections at the level of the sensory-motor cortex of rats receiving spinal cord implantation of the functionalized nanoparticles.**
**Note there is no Prussian blue staining in the brain, specifically in the motor cortex in any of the groups.**

## 3.4 *Ex vivo* Nanoparticle Studies

Examination of the diffusion of the lipophilic nanoparticle tracers indicated that in the DiI control (n=3), there was a diffusion of 6000µm compared to less than 100µm in either of the nanoparticle groups, both SPIO+SiO2+RuBpy (n=3) and SPIO+SiO2+RuBpy+C18 (n=3). Representative images are shown in Figure 3-25. Quantification of the distance of diffusion levels of the fluorescence signal revealed a statistically significant difference between the DiI control and both of the nanoparticle groups with respect to distance. This quantification is shown graphically in Figure 3-26.

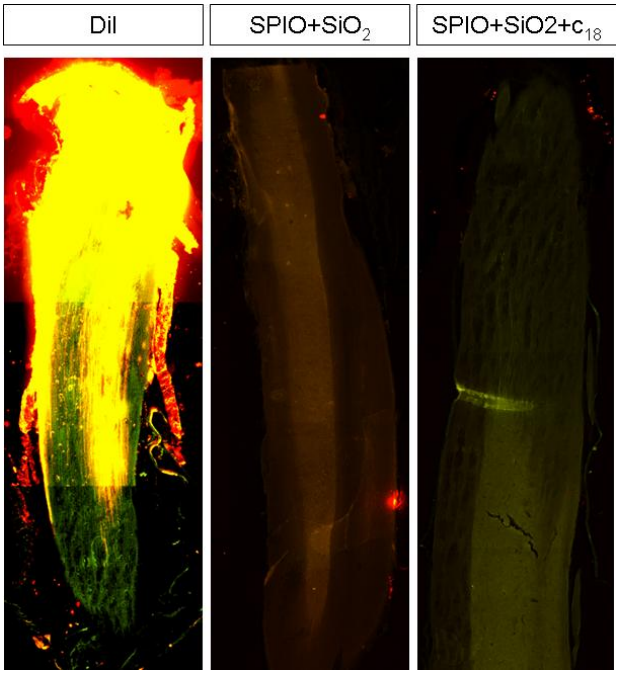


**Figure 3-25: Representative fluorescence images of *ex vivo* studies of diffusion from the rostral face of the spinal cord sections (rostral is oriented up) for DiI (n=3), SPIO+SiO2+RuBpy (n=3), and SPIO+SiO2+RuBpy+C18 (n=3). Clear diffusion of DiI extended from the rostral face, while there was no diffusion seen in either of the nanoparticle groups.**

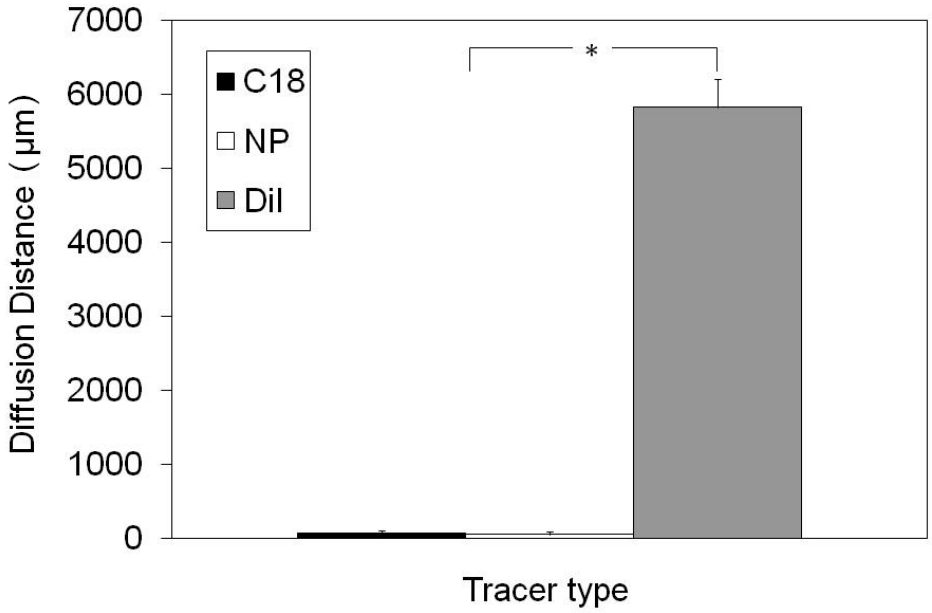


**Figure 3-26: Quantification of diffusion of lipophilic tracers in fixed spinal cord sections for DiI (n=3), SPIO+SiO2+RuBpy (n=3) and SPIO+SiO2+C18 (n=3). (*) indicates statistical significance between DiI and both nanoparticle groups with ANOVA $p<0.05$ Tukey post-hock analysis**

# Chapter 4: Discussion

## 4.1 Nanoparticle Synthesis and Characterization

Infrared (IR) characterization of nanoparticles has been used previously as a means of identifying the functional groups and silica functionalization of metal oxide nanoparticles[41] which was evidenced both in previous research and in Figure 3-1 by the evolution of peaks in the spectrum at 1050 $cm^{-1}$. IR was also used for the monitoring of the attachment of amine functional groups on silica functionalized nanoparticles with bands in the region of 2800 $cm^{-1}$[54]. Other studies of amine functionalized nanoparticles have been successful [49, 94], and they have used other characterization methods such as AES, which suggest this as a viable means for the amine functionalization[53]. Previous studies of the functionalization of silica particles with an octadecyl group used elemental analysis with electron microscopy. The long unsaturated carbon chain has a characteristic IR spectroscopic pattern in the region of 2800 $cm^{-1}$ as evidenced in Figure 3-1, and this was a means of identifying the presence of a long carbon chain on the magnetic nanoparticle. Although different synthetic routes have been applied for dextran attachment to nanoparticles [50], imine bond formation has been successfully used in the functionalization of nanoparticles with other biomolecules [49]. IR was used in Figure 3-1 to demonstrate further functionalization of the nanoparticle. Further characterization of

the nanoparticles for charge, such as zeta potential measurements or gel electrophoresis of the nanoparticles, could have been advantageous.

Scanning electron microscopic imaging of the particles revealed their size to be on the order of 200 nm in diameter, as shown in Figure 3-3. Bare SPIO nanoparticles are smallest (>50 nm); however, with the addition of the silica shell, the particle sizes increase. This size increase is due to the polymerization of silica on the surface of the particle, and the size is further increased with additional functionalization. The incorporation of the dye in the second shell provided an additional fluorescence component to the nanoparticle, as indicated in Figure 3-2 but also increased the size of the nanoparticle. The fluorescence spectrum indicated a multifunctionality of the nanoparticle when the fluorescence intensity decreased with magnetic separation. This method of fluorescence and magnetism with nanoparticles has been used previously as a method to characterize the dual functionality of the nanoparticle[41]. The increase in size with the dye incorporation was due to the further polymerization of silica. The dye was not incorporated in the layer directly adjacent to the metal oxide nanoparticle due to the possibility of distance-dependent fluorescent quenching of the dye [42]. One limitation and trade off of this method of dye encapsulation was that a larger shell can contain more dye and thus a higher fluorescence yield; however, this directly impacted the size of the nanoparticle and led to larger particles with thicker shells. The incorporation of a dye with a higher fluorescence quantum yield would be an asset to allow for smaller particle sizes while not compromising the particle size. Furthermore, this particular dye is

incorporated in the silica shell through relatively weak intermolecular forces, and without a covalent linkage of the dye to the nanoparticle, fluorescent leaching is possible.

The magnetic resonance contrast enhancement ability of the magnetic nanoparticles was strong. With the MR sequences used (see Figure 3-4) the contrast effects of the nanoparticles were clearly evident with concentrations as low as $1x10^{-5}$ M. Increasing particle concentrations had drastically increasing effects on MR contrast, and this concentration was lower than that of the nanoparticle injections made in the brain. It is clear in Figure 3-5 that the oxidation state of iron plays a major role in the contrast enhancement abilities of the magnetic nanoparticles. Further discussion on the possible oxidation of the nanoparticles is below, but the oxidation state is highly determinative in the contrast provided by the nanoparticles. Cellular interactions with nanoparticles may greatly impact this contrast.

## 4.2 *In Vitro* nanoparticle assessment

The NPC harvested from the spinal cord were used as a model of the cells in the spinal cord, and have the ability to assess the effects of the nanoparticles on the toxicity, and uptake of the nanoparticles. The cells have the ability to differentiate into neurons, astrocytes, and oligodendrocytes, and were therefore chosen to model the cellular environment of the spinal cord.

Imaging of the fluorescence of the nanoparticles incubated with the cells revealed that with increasing nanoparticle concentrations, increasing numbers of cells would contain the nanoparticles. This is shown in Figure 3-8. Only the nanoparticles with the dye multifunctionality could be visualized with fluorescence microscopy. This therefore

highlights an advantage of the dye functionalized nanoparticles. It was hypothesized that the nanoparticles with the amine as the positive charge would have the highest number of labelled cells. However, there was no evidence to suggest that. Because of the additional functionalization of the shell of the nanoparticle with the amine group, the size of the particle increased, as determined with SEM. It is however, well known that nanoparticle uptake efficiency is a function of the particle size[55]. In an experiment examining the efficiency of uptake of nanoparticles with amine functionalization, it was determined that higher levels were taken up into progenitor cells with the silica functionalization alone as opposed to the amine[53]. This might be a size dependent effect and is in contrast with research done examining the uptake efficiency of nanoparticles of the same size [38, 55], and also contrasts with studies using a highly charged poly-L-lysine bound functional group where it was found that such a highly positive functional group had strong effects on the uptake of the nanoparticle [36]. Decreasing the size could have an impact on uptake. In the case of the hydophobically coated C18 nanoparticles, suspension of the particles in water was difficult due to their hydrophobicity; a true representation of their function *in vivo* might not be shown through *in vitro* studies alone. It was also hypothesized that the nanoparticles would be associated with the cell membrane. In the confocal microscopic analysis, the particles appeared to be aggregated within the cells rather than uniformly coating the membrane. It is possible, that they were also present in the membranes of internalized endosomes. Higher resolution techniques such as electron microscopy would be required to confirm this. Dye leaching may have also influenced the counting of cells

because the dye leaching out of the nanoparticle would reduce the fluorescence yield and therefore reduce the number of counted cells.

Cell counts of nanoparticle incorporation with Prussian blue labelling could also be influenced by the effect of the silica functionalization slowing the Prussian blue colorimetric reaction forming the blue pigment compared to bare SPIO particles alone. It is possible that with thicker silica coating, Prussian blue staining would therefore be slightly reduced compared to SPIO particles alone .This would have the effect of higher relative quantification of nanoparticle labelling in the SPIO compared to those with the different functional groups.

The study of the interaction of nanoparticles with neural progenitor cells enables the investigation of cell death and uptake on a cellular level, allowing for more detailed studies and optimization of parameters before working with an in vivo model. When the particles were incorporated in the culture media, the particles were dispersed evenly, and could fall to the bottom of the culture dish. Therefore, in order for the cells to take up the nanoparticles, the cells must be mobile. Neural progenitor cells in culture conditions forming neurospheres have been demonstrated to migrate and move within the culture and within the neurosphere indicating the sphere is dynamic [95]. This mobility could explain the high level of particle uptake in culture conditions, and why the cells were able to potentially create higher intracellular concentrations of the nanoparticles than the original concentration in the media.

Toxicity studies of the nanoparticles on the NPCs indicated that the particles had a generally increasing trend in both TUNEL and Trypan blue staining according to the

concentration of the nanoparticles. Cell death was examined with Trypan blue staining and apoptosis was assessed with TUNEL staining. There was no statistically significant difference with respect to nanoparticles with and without the dye coating, suggesting that the dye did not increase toxicity. There was also no statistically significant data suggesting that the silica functionalization of the SPIO changed the toxicity of the SPIO, thus suggesting that the silica did not decrease toxicity. This correlates with a previous research hypothesis that by adding a biocompatible group to the nanoparticle, toxicity can be reduced[59]. With TUNEL staining, nanoparticles at concentrations of 10 mM did not show a statistically significant difference to the positive toxicity control, $H_2O_2$. It is difficult to assess if this implies direct toxicity at these concentrations. However, it can be concluded that higher nanoparticle concentrations have more effects on the TUNEL staining of cells. There also were no major differences in the trends found between the two techniques of TUNEL and trypan blue. There was one exceptional group in the general trend of toxicity. This was the SPIO+SiO2+No_RuBpy+BDA where, at 0.1 mM concentration, there were higher than expected TUNEL and Trypan blue levels. It is not likely that this one nanoparticle type uniquely exhibited toxicity at low quantifications compared to the other nanoparticle concentrations, and it is possible that some contamination existed in the dilution of the nanoparticles to 0.1 mM.

Trypan blue staining indicated a high percentage of cells which were dead with the culture conditions. This is likely due to the culture conditions where cells were harvested and incubated in vitro for a period totaling more than 2 weeks. With the removal of the growth factors, there is also a reduction in the proliferation of the

progenitor cells, and furthermore, cell death can be a consequence. Trypan blue is also not the most specific indicator of cell death, and therefore TUNEL staining was used for more accurate measurements. TUNEL staining is also lower because it targets only cells undergoing apoptosis; whereas, Trypan blue selects all cells with ruptured membranes. It is possible that membranes can be ruptured in cells undergoing necrosis, which would result in lower TUNEL levels comparatively. Trypan blue was used as a marker of cell death because TUNEL could not be used for the analysis of the nanoparticles with the dye due to the overlap in the fluorescence spectrum. It was also noted that there was a non-statistically significant decrease in apoptosis in the groups with nanoparticles compared to the PBS control indicated with TUNEL staining. This suggests that the mechanisms of cell death associated with the nanoparticles is more likely due to a necrotic rather than apoptotic mechanism. Further experimentation to assess if nanoparticles nanoparticles have a protective effect would be necessary to make conclusions.

It has been hypothesized that the toxicity of nanoparticles is due to the formation of reactive oxide species (ROS) [59]. It was furthermore found that in a Fenton reaction process, that SPIO nanoparticles could be oxidized, catalyzing ROS generation [66]. Optical spectroscopic results here indicated that there was an oxidation of ferrous iron to ferric iron, and this was likely taking place in the cells. There is an important link therefore between toxicity and MRI contrast enhancement of the nanoparticles. As shown in Figure 3-5, there was higher MRI contrast with the ferric iron state. It is therefore possible that in the Fenton catalyzation generating ROS, nanoparticles are oxidized, and signal

contrast increases. This could be especially problematic when using SPIO nanoparticles as a stable quantification platform. This problem exists because the concentration of nanoparticles in MRI quantification is calculated based on an equation which assumes that the contrast is directly related to particle concentration. This does not account for contrast changes, and drastically elevated measurements could lead one to conclude that nanoparticle concentrations have increased, or there was a higher than real movement of nanoparticles. This could be overcome by using nanoparticles which are fully oxidized to the $Fe_2O_3$ state before injection, or by using a more stable positive contrast agent.

## 4.3 *In vivo* Nanoparticle Assessment

In both applications of the nanoparticles as retrograde and anterograde tracers in the spinal cord and brain respectively, the contrast provided by the concentrations of nanoparticles was sufficient for their visualization in a low field strength clinical MRI scanner. A higher concentration could have provided higher signal contrast; however, *in vitro* data suggested that both with nanoparticle uptake and toxicity, higher concentrations might have detrimental effects. For this reason, a concentration of 10 mM iron oxide was deemed acceptable. The resolution achieved with clinical MRI systems of rat spinal cords in previous experiments is comparable to that done in these experiments in terms of the resolution, structural details, and anatomical structures which can be extracted from the images [10]. Detailed anatomical structures cannot be resolved, but the contrast provided with the nanoparticles is clear in both applications. There was a statistically significant difference between the contrast obtained from the sham controls using both BDA and PBS solutions, which clearly indicates that the contrast derived from

the nanoparticles demonstrably overpowers any effects from any iron in blood cells that may ensue from any surgical trauma received during the injection process. In both cases, the injection of the contrast agents were stable over time, as demonstrated by the measurements of anatomical structures and measurement of areas of decreased signal intensity of the injection site with serial imaging at multiple timepoints. Because both the host tissue and region of interest with the injected contrast agent are visible with MRI, this technique allows great advantages to supplement other visualization techniques such as microscopy. These results indicate that the MRI contrast agents and low field strength are indeed suitable for the purposes of the present study.

### 4.3.1 Anterograde Nanoparticle Tracer Assessment

The MRI experiments investigating the anterograde tracing of SPIO+SiO2+RuBpy+BDA compared to 1% BDA alone indicated that over time, the area of the zone of decreased signal of the contrast agent did not change from 1 day to 22 days after the injection. The MRI slices with the maximum area of decreased signal zones were chosen, and the area of decreased signal present in the other slices remained the same over the time points assessed. This means of measuring the area in both the axial and sagittal planes accounted for changes which would occur either from non-specific diffusion in the extacellular matrix or within axons. In a similar study examining the rat sciatic nerve with ultra-small iron oxide nanoparticles, there was a clear change in this parameter from the first to the tenth day [36]. Examining the other axial and sagittal MR sections did not reveal the appearance of any contrast at the level of the cervical spinal

cord, the brain stem, or inferior to the cerebellum in regions where the pyramidal tracts would be expected to descend.

In the histological quantification of Prussian blue staining in the anterograde injections, there were no statistically significant differences in any measurements between the control and experimental groups. This higher than expected level of Prussian blue staining in the control group was likely due to numerous causes such as byproducts of hemorrhage (e.g. hemosiderin) associated with the tracer injection, as all of these measures were the same. This could also have been associated with the inflammatory response to the nanoparticles with a phagocytic cell; for instance, a macrophage. The specific cells involved in the uptake of nanoparticles could be identidied with immunohistochemistry. Because the MRI contrast was so strong in the nanoparticle group, it was expected that there would be a greater optical absorbance of Prussian blue; however, this was not evident. The low Prussian blue staining is likely a combination of two major factors. The total concentration of each injection site totalled 1 µL, and with each injection containing 10 mM of iron, the total number of moles would have been 1 nM. It is likely that a concentration of this small magnitude could not be easily differentiated with histology. However, this does indicate the strong signal contrast enhancement potential of such small concentrations of nanoparticles. Secondly, due to the thick silica shell around the nanoparticle, the Prussian blue staining reaction rate was drastically slowed for the examination of the nanoparticles. This phenomenon was described earlier, but when the staining time is too long, high background staining occurs.

Further examination of the differences between the groups revealed characteristic cellular staining along with the staining of cellular projections with BDA staining in the BDA group. This is shown in Figure 3-20. This was not the case in the SPIO+SiO2+RuBpy+BDA group where the staining is present in amorphous groupings without the same characteristic cellular appearance. This would indicate major differences in the uptake and transport of the nanoparticle and non-conjugated BDA biomolecule. There was no staining present for BDA at the level of the pyramidal tracts in the brainstem or in the ventral dorsal columns of the cervical spinal cord which could be easily identified. It is possible that the BDA stain degraded with time, or that anatomical variations in the landmarks in the rats lead to slight differences in the sites of injection in the cortex. These same coordinates with respect to the bregma as an anatomical landmark have been used previously with success, and staining in the corticospinal tract was strong [33].

### 4.3.2 Retrograde Nanoparticle Tracer Assessment

The lack of change of the measured length of signal contrast in the spinal cord in the retrograde tracer experiments indicates limited diffusion of the particles within the spinal cord. Previous research where this measurement was employed in the rat sciatic nerve indicated distance changes of as much as 10 mm in a period of 10 days [36], a study where particles with a size totalling less than 50 nm were used. It is likely that due to the relatively larger size of the nanoparticles used in the present study, their uptake and subsequent transport was limited.

To corroborate the retrograde tracer results with the MRI data, the histological examination of the tissue revealed no fluorescence from the nanoparticles in the cervical spinal cord. Furthermore, there was no fluorescence from the nanoparticles in the brains of the animals. Prussian blue stained sections were examined in the region of the sensory-motor cortex and no staining was evident. Thus there was no evidence that nanoparticles were transported to these regions of the brain, and tracing to these areas in the brain was deemed critical for the study of spinal cord injury[90]. Therefore, this tracer was limited in the application of spinal cord injury studies. With the current experimental setup, there was no detection that nanoparticles had been transported to the brain. It is possible that the use of smaller sized nanoparticles containing a fluorescent dye with a higher fluorescent quantum yield could yield evidence that nanoparticles can be transported and detected with higher efficiency.

## 4.4 *Ex vivo* Assessment of Nanoparticles

From the fluorescence quantification of fixed tissue where dye had been permitted to diffuse *ex vivo*, there was no indication of diffusion in comparison to the lipophilic dye DiI. Both nanoparticles with and without lipophilic functionalization were allowed to diffuse for a 3 week period, and the measured fluorescence distance from the rostral face of the spinal cord was 100 μm in both cases, with no statistically significant difference between them. This contrasts with the 6000 μm distance exhibited by the conventional lipophillic tracer DiI. The difference between the nanoparticles and the dye was statistically significant. It is again possible that nanoparticle size rendered them incapable of incorporation into the plasma membrane and diffusion within the fixed spinal cord.

Using nanoparticles with a lipophilic functional group which is smaller than the thickness of the bilayer could potentially enable diffusion to occur.

It is possible that the use of another capping agent as opposed to wax would have further facilitated the diffusion of the nanoparticle tracer, as was used by Chen and others.[80]

## 4.5 Future Directions

The application of the nanoparticles synthesized in this project was limited for the study of axon tracing; however, their stability over time with MRI would be an asset as a stereotaxic label for MRI. This would be highly advantageous for the study of electrophysiology probes implanted in the brain. It would also be useful for the probing of structures or labelling studies done in the brain. It has the potential to be used as a label for serial imaging over time of a specific anatomical region and be correlated with histology directly.

Nanoparticles still have major potential in as axon tracers. It is likely that smaller nanoparticles will be much more efficient with respect to uptake and transport, allowing the limitations experienced in the present study to be overcome. The use of a dye with a higher fluorescent quantum yield would further facilitate the histological examination of tissue and be un-ambiguous for histological examination.

Nanoparticles with a different magnetic contrast agent such as gadolinium oxide would be advantageous both because it is a positive contrast agent which is un-ambiguous in MRI measurements, and also because the staining for gadolinium cannot be

confused with elements at high concentrations in the body. This was problematic with iron oxide because of the high levels of iron present in the blood in a normal subject.

# Chapter 5: Conclusions

The characterization of the nanoparticles indicated that fluorescence and magnetic functionalization of an iron oxide core nanoparticle through a silica shell was possible. It was furthermore indicated that subsequent functionalizations could be added to the nanoparticle. *In vitro* experiments indicated that nanoparticles had no statistically significant evidence of toxicity to cultured neural progenitor cells at concentrations below 10 mM as measured with both Trypan blue and TUNEL. At 10 mM, all functionalizations of nanoparticles were efficient for cell labeling as indicated by confocal microscope and Prussian blue staining.

*In vivo* injections of multifunctional nanoparticles injected into the rat brain indicated that, at levels as low as 5 nM, clear MRI signal contrast could be achieved, stably expressed over a period of at least 3 weeks, and with a difference of the contrast agent compared to the control that was statistically significant in the area of hypointensity. There was no statistically significant change in the size of the zone of hypointensity created by the injection of the iron during this time period. There was no change in contrast area shape or area indicated with MRI, and there was furthermore no evidence with histology to indicate anterograde travel of the nanoparticles with the techniques used.

Retrograde nanoparticle experiments did not indicate any statistically significant changes in the area of the region of hypointensity diffusing along the spinal cord. There were no statistically significant differences with the staining for Prussian blue in the spinal cord between controls and experimental groups, and accordingly, there was no evidence that nanoparticles had travelled to the brain.

It is likely that due to the size of the nanoparticles, there were limitations in axon transport either because of a lack of uptake of the nanoparticles, or difficulty in transport. With the application of smaller particles with higher fluorescence intensity, it might be possible to overcome these limitations.

# Chapter 6: References

1. von Bartheld CS. Axonal transport and neuronal transcytosis of trophic factors, tracers, and pathogens. J Neurobiol 2004;58:295-314.
2. Nauta WJ. Some early travails of tracing axonal pathways in the brain. J Neurosci 1993;13:1337-45.
3. Bodian D. A new method for staining nerve fibers and nerve endings in mounted paraffin sections. Anat Rec 1936;65:89-97.
4. McEwen BS, Grafstein B. Fast and slow components in axonal transport of protein. J Cell Biol 1968;38:494-508.
5. Cowan WM, Gottlieb DI, Hendrickson AE, Price JL, Woolsey TA. The autoradiographic demonstration of axonal connections in the central nervous system. Brain Res 1972;37:21-51.
6. Zaborszky L, and Heimer, L. Combination of tracer techniques, especially HRP and PHA-L, with transmitter identification for correlated light and electron microscopic studies
Neuroanatomical Tract-Tracing Methods II, Recent
Progress 1989:173–99.
7. von Bartheld CS, Cunningham DE, Rubel EW. Neuronal tracing with DiI: decalcification, cryosectioning, and photoconversion for light and electron microscopic analysis. J Histochem Cytochem 1990;38:725-33.
8. Papadopoulos GC, Dori I. DiI labeling combined with conventional immunocytochemical techniques for correlated light and electron microscopic studies. J Neurosci Methods 1993;46:251-8.
9. Manganas LN, Zhang X, Li Y, et al. Magnetic resonance spectroscopy identifies neural progenitor cells in the live human brain. Science 2007;318:980-5.
10. Iannotti C, Li H, Stemmler M, Perman WH, Xu XM. Identification of regenerative tissue cables using in vivo MRI after spinal cord hemisection and schwann cell bridging transplantation. J Neurotrauma 2002;19:1543-54.
11. Bilgen M, Al-Hafez B, Berman NE, Festoff BW. Magnetic resonance imaging of mouse spinal cord. Magn Reson Med 2005;54:1226-31.
12. Beuf O, Jaillon F, Saint-Jalmes H. Small-animal MRI: signal-to-noise ratio comparison at 7 and 1.5 T with multiple-animal acquisition strategies. Magma 2006;19:202-8.

13. Holodny AI, Watts R, Korneinko VN, et al. Diffusion tensor tractography of the motor white matter tracts in man: Current controversies and future directions. Ann N Y Acad Sci 2005;1064:88-97.
14. Elshafiey I, Bilgen M, He R, Narayana PA. In vivo diffusion tensor imaging of rat spinal cord at 7 T. Magn Reson Imaging 2002;20:243-7.
15. Vargas MI, Delavelle J, Jlassi H, et al. Clinical applications of diffusion tensor tractography of the spinal cord. Neuroradiology 2008;50:25-9.
16. Bilgen M, Dancause N, Al-Hafez B, He YY, Malone TM. Manganese-enhanced MRI of rat spinal cord injury. Magn Reson Imaging 2005;23:829-32.
17. Helmchen F, Denk W. Deep tissue two-photon microscopy. Nat Methods 2005;2:932-40.
18. Bridot J-L, Faure A-C, Laurent S, et al. Hybrid Gadolinium Oxide Nanoparticles:  Multimodal Contrast Agents for in Vivo Imaging. Journal of the American Chemical Society 2007;129:5076-84.
19. Inoue Y, Izawa K, Yoshikawa K, Yamada H, Tojo A, Ohtomo K. In vivo fluorescence imaging of the reticuloendothelial system using quantum dots in combination with bioluminescent tumour monitoring. Eur J Nucl Med Mol Imaging 2007;34:2048-56.
20. Cui B, Wu C, Chen L, et al. One at a time, live tracking of NGF axonal transport using quantum dots. Proc Natl Acad Sci U S A 2007;104:13666-71.
21. Filler AG. Axonal transport and MR imaging: prospects for contrast agent development. J Magn Reson Imaging 1994;4:259-67.
22. Schroeder T. Imaging Stem-Cell-Driven Regeneration in Mammals. Nature 2008;453:345-251.
23. Rad AM, Arbab AS, Iskander AS, Jiang Q, Soltanian-Zadeh H. Quantification of superparamagnetic iron oxide (SPIO)-labeled cells using MRI. J Magn Reson Imaging 2007;26:366-74.
24. Wu SH, Lin YS, Hung Y, et al. Multifunctional mesoporous silica nanoparticles for intracellular labeling and animal magnetic resonance imaging studies. Chembiochem 2008;9:53-7.
25. Reichert DE, Lewis JS, Anderson CJ. Metal complexes as diagnostic tools. Coordination Chemistry Reviews 1999;184:3-66.
26. Strijkers GJ, Mulder WJ, van Tilborg GA, Nicolay K. MRI contrast agents: current status and future perspectives. Anticancer Agents Med Chem 2007;7:291-305.
27. Suh WH, Suslick KS, Stucky GD, Suh YH. Nanotechnology, nanotoxicology, and neuroscience. Prog Neurobiol 2009;87:133-70.
28. Gao X, Dave SR. Quantum dots for cancer molecular imaging. Adv Exp Med Biol 2007;620:57-73.
29. Xing Y, So MK, Koh AL, Sinclair R, Rao J. Improved QD-BRET conjugates for detection and imaging. Biochem Biophys Res Commun 2008;372:388-94.
30. Cho K, Wang X, Nie S, Chen ZG, Shin DM. Therapeutic nanoparticles for drug delivery in cancer. Clin Cancer Res 2008;14:1310-6.

31. Liu Y, Miyoshi H, Nakamura M. Nanomedicine for drug delivery and imaging: a promising avenue for cancer therapy and diagnosis using targeted functional nanoparticles. Int J Cancer 2007;120:2527-37.
32. Li X, Fan Y, Watari F. Current investigations into carbon nanotubes for biomedical application. Biomed Mater;5:22001.
33. Yang X, Westwick H, Cao X, Tsai EC. MAGNETIC RESONANCE TRACKING OF NOVEL BIODEGRADABLE, BIOCOMPATIBLE PLGA CHANNELS FOR SPINAL CORD REPAIR. J Neurotrauma 2008 25:894.
34. Cho Y, Borgens RB. The effect of an electrically conductive carbon nanotube/collagen composite on neurite outgrowth of PC12 cells. J Biomed Mater Res A.
35. Das M, Patil S, Bhargava N, et al. Auto-catalytic ceria nanoparticles offer neuroprotection to adult rat spinal cord neurons. Biomaterials 2007;28:1918-25.
36. Enochs WS, Schaffer B, Bhide PG, et al. MR imaging of slow axonal transport in vivo. Exp Neurol 1993;123:235-42.
37. van Everdingen KJ, Enochs WS, Bhide PG, et al. Determinants of in vivo MR imaging of slow axonal transport. Radiology 1994;193:485-91.
38. Song M, Moon WK, Kim Y, Lim D, Song IC, Yoon BW. Labeling efficacy of superparamagnetic iron oxide nanoparticles to human neural stem cells: comparison of ferumoxides, monocrystalline iron oxide, cross-linked iron oxide (CLIO)-NH2 and tat-CLIO. Korean J Radiol 2007;8:365-71.
39. Sykova E, Jendelova P. Magnetic resonance tracking of transplanted stem cells in rat brain and spinal cord. Neurodegener Dis 2006;3:62-7.
40. Wu X, Hu J, Zhou L, et al. In vivo tracking of superparamagnetic iron oxide nanoparticle-labeled mesenchymal stem cell tropism to malignant gliomas using magnetic resonance imaging. Laboratory investigation. J Neurosurg 2008;108:320-9.
41. Yu S-Y, Zhang H-J, Yu J-B, Wang C, Sun L-N, Shi W-D. Bifunctional Magnetic-Optical Nanocomposites: Grafting Lanthanide
Complex onto Core-Shell Magnetic Silica Nanoarchitecture. Langmuir 2007;23:7836-40.
42. Zhang L, Liu B, Dong S. Bifunctional Nanostructure of Magnetic Core Luminescent Shell and Its Application as
Solid-State Electrochemiluminescence Sensor Material. J Phys Chem B 2007;111:10448-52.
43. Enzel P, Adelman NB, Beckman KJ, Campbell DJ, Ellis AB, Lisensky GC. Preparation and Properties of an Aqueous Ferrofluid J Chem Educ 1999;76:943.
44. Stöber W, Fink A, Bohn E. Controlled Growth of Monodisperse Silica Spheres in the Micron Size Range. J Colloid Interface Sci 1968;26:62-9.
45. Lu Y, Yin Y, Mayers BT, Xia Y. Modifying the surface properties of superparamagnetic iron oxide nanoparticles through a Sol-Gel approach. Nano Lett 2002;2:183-6.
46. Santra S, Wang K, Tapec R, Tan W. Development of novel dye-doped silica nanoparticles for biomarker application. Journal of Biomedical Optics 2001;6:160–6.
47. Yu HC, Argyros A, Barton G, et al. Quantum dot and silica nanoparticle doped polymer optical fibers. Opt Express 2007;15:9989-94.

48. Veenman CL, Reiner A, Honig MG. Biotinylated dextran amine as an anterograde tracer for single- and double-labeling studies. Journal of Neuroscience Methods 1992;41:239-54.
49. Zhu N, Cai H, He P, Fang Y. Tris(2,2'-bipyridyl)cobalt(III)-doped silica nanoparticle DNA probe for the electrochemical detection of DNA hybridization. Analytica Chimica Acta 2003;481:181–9.
50. Earhart C, Jana NR, Erathodiyil N, Ying JY. Synthesis of carbohydrate-conjugated nanoparticles and quantum dots. Langmuir 2008;24:6215-9.
51. Zhao Q, Gottschalk I, Carlsson J, et al. Preparation and Purification of an End to End Coupled
mEGF-Dextran Conjugate. Bioconjugate Chem 1997;8:927-34.
52. Venkarathri N, Yoo JW. Synthesis and Characterization of Silica Nanosphere from Octadecyltrimethoxy Silane. Bulletin of the Korean Chemical Society 2008;29:29-30.
53. Zhang C, Wangler B, Morgenstern B, et al. Silica- and alkoxysilane-coated ultrasmall superparamagnetic iron oxide particles: a promising tool to label cells for magnetic resonance imaging. Langmuir 2007;23:1427-34.
54. Giaume D, Poggi M, Casanova D, et al. Organic functionalization of luminescent oxide nanoparticles toward their application as biological probes. Langmuir 2008;24:11018-26.
55. Yacobi NR, Demaio L, Xie J, et al. Polystyrene nanoparticle trafficking across alveolar epithelium. Nanomedicine 2008;4:139-45.
56. Chakraborty SK, Fitzpatrick JA, Phillippi JA, et al. Cholera toxin B conjugated quantum dots for live cell labeling. Nano Lett 2007;7:2618-26.
57. Rajan SS, Liu HY, Vu TQ. Ligand-bound quantum dot probes for studying the molecular scale dynamics of receptor endocytic trafficking in live cells. ACS Nano 2008;2:1153-66.
58. Ianoul A, Westwick H, Nowacka L, Quan B. Interactions of lactoferricin B derivatives with model cell membrane studied by Raman spectroscopy. Journal of Raman Spectroscopy 2007;38:200-4.
59. Unfried K, Albrecht C, Klotz L-O, VonMikecz A, Grether-Beck S, Schins RPF. Cellular responses to nanoparticles: Target structures and mechanisms. Nanotoxicology 2007;1:52-71.
60. Wessendorf MW. Fluoro-Gold: composition, and mechanism of uptake. Brain Res 1991;553:135-48.
61. Praetorius M, Brunner C, Lehnert B, et al. Transsynaptic delivery of nanoparticles to the central auditory nervous system. Acta Otolaryngol 2007;127:486-90.
62. Lu CW, Hung Y, Hsiao JK, et al. Bifunctional magnetic silica nanoparticles for highly efficient human stem cell labeling. Nano Lett 2007;7:149-54.
63. Mok H, Park JW, Park TG. Enhanced intracellular delivery of quantum dot and adenovirus nanoparticles triggered by acidic pH via surface charge reversal. Bioconjug Chem 2008;19:797-801.

64. Kumar V, Abbas AK, Fausto N, Aster JC. Robbins and Cotran Pathologic Basis of Disease. 8 ed. Philadelphia: Elsevier; 2010.
65. Limbach LK, Wick P, Manser P, Grass RN, Bruinink A, Stark WJ. Exposure of engineered nanoparticles to human lung epithelial cells: influence of chemical composition and catalytic activity on oxidative stress. Environ Sci Technol 2007;41:4158-63.
66. Auffan M, Achouak W, Rose J, et al. Relation between the redox state of iron-based nanoparticles and their cytotoxicity toward Escherichia coli. Environ Sci Technol 2008;42:6730-5.
67. Rieter WJ, Kim JS, Taylor KM, An H, Lin W, Tarrant T. Hybrid silica nanoparticles for multimodal imaging. Angew Chem Int Ed Engl 2007;46:3680-2.
68. Ding M, Chen F, Shi X, Yucesoy B, Mossman B, Vallyathan V. Diseases caused by silica: mechanisms of injury and disease development. Int Immunopharmacol 2002;2:173-82.
69. Latham AH, Williams ME. Controlling transport and chemical functionality of magnetic nanoparticles. Acc Chem Res 2008;41:411-20.
70. Gunawardena S, Goldstein LS. Cargo-carrying motor vehicles on the neuronal highway: transport pathways and neurodegenerative disease. J Neurobiol 2004;58:258-71.
71. MacInnis BL, Campenot RB. Retrograde support of neuronal survival without retrograde transport of nerve growth factor. Science 2002;295:1536-9.
72. Zhang K, Fang H, Chen Z, Taylor JS, Wooley KL. Shape effects of nanoparticles conjugated with cell-penetrating peptides (HIV Tat PTD) on CHO cell uptake. Bioconjug Chem 2008;19:1880-7.
73. Kinyanjui MW, Fixman ED. Cell-penetrating peptides and proteins: new inhibitors of allergic airways disease. Can J Physiol Pharmacol 2008;86:1-7.
74. Fritzsch B, Muirhead KA, Feng F, Gray BD, Ohlsson-Wilhelm BM. Diffusion and imaging properties of three new lipophilic tracers, NeuroVue (TM) Maroon, NeuroVue (TM) Red and NeuroVue (TM) Green and their use for double and triple labeling of neuronal profile. Brain Res Bull 2005;66:249-58.
75. Godement P, Vanselow J, Thanos S, Bonhoeffer F. A study in developing visual systems with a new method of staining neurones and their processes in fixed tissue. Development 1987;101:697-713.
76. Lukas JR, Aigner M, Denk M, Heinzl H, Burian M, Mayr R. Carbocyanine postmortem neuronal tracing: Influence of different parameters on tracing distance and combination with immunocytochemistry. J Histochem Cytochem 1998;46:901-10.
77. Nakada C, Ritchie K, Oba Y, et al. Accumulation of anchored proteins forms membrane diffusion barriers during neuronal polarization. Nat Cell Biol 2003;5:626-32.
78. Fritzsch B, Wilm C. DEXTRAN AMINES IN NEURONAL TRACING. Trends Neurosci 1990;13:14-.
79. Brandt HM, Apkarian AV. Biotin-dextran: a sensitive anterograde tracer for neuroanatomic studies in rat and monkey. J Neurosci Methods 1992;45:35-40.

80. Chen BK, Miller SM, Mantilla CB, Gross L, Yaszemski MJ, Windebank A. Optimizing conditions and avoiding pitfalls for prolonged axonal tracing with carbocyanine dyes in fixed rat spinal cords. Journal of Neuroscience Methods 2006;154:256-63.
81. Perrin FE, Stoeckli ET. Use of lipophilic dyes in studies of axonal pathfinding in vivo. Microsc Res Tech 2000;48:25-31.
82. Cosker KE, Courchesne SL, Segal RA. Action in the axon: generation and transport of signaling endosomes. Curr Opin Neurobiol 2008;18:270-5.
83. Lauffer RB. Paramagnetic metal complexes as water proton relaxation agents for NMR imaging: theory and design. Chemical Reviews 1987;87:901-27.
84. Wang Y-XJ, Hussain SM, Krestin GP. Superparamagnetic iron oxide contrast agents: physicochemical characteristics and applications in MR imaging European Radiology 2000;11:1432-084
85. Bridot JL, Faure AC, Laurent S, et al. Hybrid gadolinium oxide nanoparticles: multimodal contrast agents for in vivo imaging. J Am Chem Soc 2007;129:5076-84.
86. Gilad AA, Walczak P, McMahon MT, et al. MR tracking of transplanted cells with "positive contrast" using manganese oxide nanoparticles. Magn Reson Med 2008;60:1-7.
87. Na HB, Lee JH, An K, et al. Development of a T1 contrast agent for magnetic resonance imaging using MnO nanoparticles. Angew Chem Int Ed Engl 2007;46:5397-401.
88. Norek M, Kampert E, Zeitler U, Peters JA. Tuning of the size of Dy2O3 nanoparticles for optimal performance as an MRI contrast agent. J Am Chem Soc 2008;130:5335-40.
89. Harpur ES, Worah D, Hals PA, Holtz E, Furuhama K, Nomura H. Preclinical safety assessment and pharmacokinetics of gadodiamide injection, a new magnetic resonance imaging contrast agent. Invest Radiol 1993;28 Suppl 1:S28-43.
90. Tsai EC, van Bendegem RL, Hwang SW, Tator CH. A novel method for simultaneous anterograde and retrograde labeling of spinal cord motor tracts in the same animal. J Histochem Cytochem 2001;49:1111-22.
91. Kulbatski I, Mothe AJ, Keating A, Hakamata Y, Kobayashi E, Tator CH. Oligodendrocytes and radial glia derived from adult rat spinal cord progenitors: morphological and immunocytochemical characterization. J Histochem Cytochem 2007;55:209-22.
92. Marchenko S, Flanagan L. Counting human neural stem cells. J Vis Exp 2007:262.
93. Melanson-Drapeau L, Beyko S, Dave S, et al. Oligodendrocyte progenitor enrichment in the connexin32 null-mutant mouse. J Neurosci 2003;23:1759-68.
94. Smith JE, Medley CD, Tang Z, Shangguan D, Lofton C, Tan W. Aptamer-conjugated nanoparticles for the collection and detection of multiple cancer cells. Anal Chem 2007;79:3075-82.
95. Wang TY, Sen A, Behie LA, Kallos MS. Dynamic behavior of cells within neurospheres in expanding populations of neural precursors. Brain Res 2006;1107:82-96.